論文 / 著書情報
Article / Book Information

題目(和文)	レーザ分子線エピタキシ法によるZnO量子構造の作製および紫外線発光素子への応用
Title(English)	Quantum structures and ultraviolet light-emitting devices based on ZnO thin films grown by laser molecular-beam epitaxy
著者(和文)	大友 明
Author(English)	Akira Ohtomo
出典(和文)	学位:博士(工学), 学位授与機関:東京工業大学, 報告番号:甲第4398号, 授与年月日:2000年3月26日, 学位の種別:課程博士, 審査員:川崎雅司
Citation(English)	Degree:Doctor (Engineering), Conferring organization: Tokyo Institute of Technology, Report number:甲第4398号, Conferred date:2000/3/26, Degree Type:Course doctor, Examiner:
学位種別(和文)	博士論文
Type(English)	Doctoral Thesis

Quantum Structures and Ultraviolet Light Emitting Devices Based on ZnO Thin Films Grown by Laser Molecular-Beam Epitaxy

Akira Ohtomo

Department Innovative and Engineered Materials
Tokyo Institute of Technology

January 2000

Contents

§7. High Throughput Optimizations of Alloy and Doped Films Based on ZnO and Parallel Synthesis of ZnO/$Mg_xZn_{1-x}O$ Quantum Wells Using Combinatorial Laser MBE

Chapter 1. General Introduction

1.1. Background

In this decade, short wavelength laser diode has been intensively studied to realize ultra-high optical density optical storage and other new optical application. Blue-green laser emission was first demonstrated in ZnSe-based heterostructures[1]. Although this class of lasers was considered to be promising because most of the device design and processing would be taken after those for GaAs based lasers, short lifetime due to the instability of materials is still problem. Recently, GaN and related III-nitride alloys have attracted considerable attention since Nakamura *et al.* demonstrated high emission efficiency blue light emitting diodes[2] and continuous operation of laser diode[3]. Such high-performance devices could be available after several breakthroughs, *i. e.*, the use of low temperature AlN[4] and GaN[5] buffer layers during the metal-organic chemical vapor deposition (MOCVD) growth, development of $In_xGa_{1-x}N$/GaN quantum well structures[6], and epitaxial lateral over growth technique.[7] However, device-quality films have to be grown at very high temperature (~1200° C) and the threshold for laser action is still high.

In modern microelectronics, metal oxides play various important parts of the electronics using the versatile functions such as metallic, semiconducting, insulating, superconducting, dielectric, ferroelectric, magnetic, and various kinds of non-linear optical properties. Besides, metal oxides have recently shown novel properties, such as high temperature superconductivity[8] and colossal magnetoresistance[9], which attract our attention to explore a new field of microelectronics based on the oxide heterostructures.[10] Epitaxial growth technology of metal oxide films has improved drastically during the last decade because the discovery of high-T_c superconductor (HTSC) triggered intensive studies of the film preparation not only for device application but also for basic research of physics. There is number of studies on epitaxial growth technique of metal oxide films, however, most of the cases is still far behind the matured technologies of compound semiconductors standing on a big industry.

Here are several reasons why quality of the oxide heterostructures is so far behind that of the semiconductors. Metal oxides have been regarded for a long time as polycrystalline materials in nature, with lower purity and higher defect density than semiconductors such as silicon and gallium arsenide. One of the reasons is the complexity of the crystallographic structure, resulting in difficulties at controlling both physical and chemical properties. There are many crystallographic structures. For

instance, rutile and corundum, having relatively simple structures, but also perovskite and spinel, some of which include several tens of atoms in a primitive unit cell. Multiple elements and the large unit cell size increase the difficulty of growing high-quality single crystals. Non-stoichiometry should also be considered a serious problem for controlling the properties. For example, vanadium oxide (VO_x) includes a wide range of intermediate phases with $0.8 \leq x \leq 1.3$. Thus, the epitaxial growth is generally much difficult with oxides than with metals or semiconductors. There is also the number of complexity in roles to determine the physical properties. This is regarded as a contrast case to relatively simple descriptions of semiconductor physics. Lack of the crystalline perfection makes further difficult to understand the physical properties, resulting in decreasing positive effort to improve the growth techniques as well as number of possible investigations.

In spite of such difficulties, however, an atomic scale control on the heteroepitaxial growth of HTSC related materials has been developed.[11] This has crucially required an understanding of inorganic chemistry and developing of laser molecular-beam epitaxy (L-MBE) techniques.[12] An atomic-scale growth technology of HTSC and related metal oxide thin films should enable us to fabricate not only high-performance devices such as HTSC tunnel junctions,[13] but also to explore a new field of electronics with the versatile functions.

The epitaxial growth techniques with using L-MBE attract us to investigate not only electric function but also novel optical functions of metal oxides. The present study started to investigate ZnO and to examine its possibility for fabrication of an ultraviolet light emitter.

1.2. A Widegap Semiconductor Metal Oxide: ZnO

ZnO has been used in applications such as surface acoustic wave (SAW) filters, transparent conducting oxides (TCO), barristers, and gas sensors. These applications utilize following properties of ZnO, piezoelectricity, widegap, *unipolarity* of carrier doping, and carrier transport properties dominated by double Schottky barriers at the grain boundaries.

ZnO has wurtzite structure, in which alternating parallel planes composed of Zn and O ions stacks along the *c*-axis direction, as is schematically drown in Fig. 1-1. Single crystal is terminated on one side by an O plane (-*c*) and on another side by a Zn plane (+*c*) to maintain the charge neutrality so that there is polarity along the *c*-axis direction. Thus, the piezoelectricity exists along the *c*-axis direction, thus, internal electric field appears when external stress is applied. A *c*-axis oriented but in-plane randomly oriented films are applied for SAW filter with the use of the sapphire substrates.

The *n*-type semiconducting of ZnO is attributed to Frenkel-type defects due to an interstitial Zn which generates excess oxygen,[14] as given by,

$$Zn_{Zn}^{X} \longrightarrow Zn_i^{\bullet} + e' + (0.05(eV)) \quad (1\text{-}1)$$

$$Zn_i^{\bullet} \longrightarrow Zn_i^{\bullet\bullet} + e' + (0.5 - 1.5x10^{-4}T\ (eV)) \quad (1\text{-}2)$$

$$O_O^X \longrightarrow \frac{1}{2}O_2(g) \quad (1\text{-}3),$$

where Zn_{Zn}^{X} and O_O^X are Zn and O ion located in the wurtzite lattice site respectively, $Zn_i^{\bullet}$ and $Zn_i^{\bullet\bullet}$ are Zn interstice having positive charge (the superscript dots indicate the number of unity), *e*' is electron, O_2(g) is a molecular gas of oxygen, and *T* is the absolute temperature.

At room temperature, the intrinsic electron density and the electron mobility of a bulk single crystal is ~10^{15} cm^{-3} and ~300 cm^2/Vs, respectively, *i.e.*, the resistivity (ρ) of ~10 Ωcm.[15] It is well known that n^+-type ZnO can be readily obtained by doping of group-III[16,17], -IV[18], or -VII ions.[19] High conducting n^+-type (ρ~10^{-4} Ωcm) and transparent ZnO is recently paid much attention for application towards TCO film in modern solar cell for low cost and high reproducibility. In contrast to the simplicity on *n*-type doping, it is difficult to form *p*-type ZnO due to a strong *unipolarity* of carrier doping.

The double Schottky potential barriers located in the grain boundaries play important role in polycrystalline ZnO. When there is a deep trap level at the grain boundaries, electron are trapped at the grain boundaries to induce carrier depletion around the grain boundaries and to built double Schottky barrier.[20] Schottky barrier height and density can be tuned by impurity doping, resulting in achieving a suitable carrier transport property for the ceramic barristers.[21] Since the electronic properties related with the grain boundary structures can be modified by absorption of various kinds of gases on the surface, ZnO thin films have been utilized for gas sensor media.

Among possible applications, we have been interesting in an application as light emitting devices (LEDs). ZnO is considered to be a suitable material for fabricating short-wavelength semiconductor light emitter such as LEDs and laser diodes (LEDs) because of its wide band gap. The conventional short-wavelength LEDs and LDs are traditionally based on group-II selenides and group-III nitrides. In comparison to these materials, ZnO has a comparable band gap (E_g) of 3.37 eV and much larger exciton binding energy (E_b^{ex}) of 60 meV as listed in Table 1-1 together with other physical parameters and typical growth temperatures.

Here, an explanation of an exciton is given. Structure of exciton has very similar structure to that of a hydrogen atom. It is composed of two particles, an electron and a hole, which were generated by optical or electrical excitation. In an ionic crystal, Coulomb interaction of electron-hole pair is screened by the crystal field. The magnitude of screening is proportional to the dielectric constant. As a result, the Bohr radius of an exciton increases and its binding energy decreases, so that exciton binding energy is lower than that of a hydrogen atom. The Bohr radius (r_B) and the binding energy of an exciton are given by,

$$r_B = 0.52n^2 \frac{\varepsilon}{\mu}(\text{Å}) \quad (n=1, 2, 3, \ldots) \qquad (1\text{-}4)$$

$$E_b^{ex} = 13.6 \frac{1}{n^2} \frac{\mu}{\varepsilon^2}(\text{eV}) \quad (n=1, 2, 3, \ldots) \qquad (1\text{-}5),$$

where n is natural integer as the principle quantum number, ε is the static dielectric constant, and μ is the reduced mass of exciton.

An excitonic radiative recombination probability of exciton is very high due to very large oscillator strength. Therefore, an excitonic radiative recombination process is expected to achieve very high efficiency in a comparison with electron-hole plasma (EHP), which is unique lasing mode in conventional compound semiconductor LDs.[22] It is necessary for ahieving excitonic recombination at room temperature that the exciton binding energy is much larger than thermal energy of room temperature (kT=25 meV). ZnO has much larger exciton binding energy (60 meV) than kT and those of ZnSe (22 meV), ZnS (40 meV), and GaN (25 meV), which have been used for short wavelength LEDs and LDs. This is one of the reasons why we chose ZnO for realizing an excitonic laser. In addition, ZnO, as a metal *oxide*, is superior over selenides and nitrides in chemical and thermal stability, and resistance to oxidation.

ZnSe based LDs has been investigated for a long time, however, the device life time is significantly short due to rapid degradation mechanism initiated from crystalline defects.[23] While, GaN based on LEDs and LDs are now commercially available. Surprisingly, lifetime of LDs has been achieved to be as long as 10^4 h in spite of very high defect density and large threshold.[24] Very high growth temperature (~1200° C) is applied to grow *device-grade* film. This practical issue suppresses possible application range. In case of ZnO, an optimum growth temperature is found at 500° C. Useful advantages such as large excitonic binding energy and relatively low growth temperature can be expected to give us an opportunity to accomplish high efficiency of the devices and further to expand the possibility towards wide-range device application.

Here explanation of radiative recombination processes associating with excitonic interaction is presented. Figure 1-2 shows a schematic illustration of excitonic spontaneous emission. An electron is simultaneously excited into the conduction band by the absorption of a photon having larger energy than the band gap, and then an electron-hole pair is formed due to Coulomb interaction. The excited electron-hole pair falls down into the free exciton level whose energy is lower than the band gap by exciton binding energy. At low temperature, the exciton can be located at local potential minima due to donor and/or acceptor impurities, resulting in formation of donor or acceptor bound exciton. An exciton located at one of those energy levels can recombine rapidly to emit a photon. Typical lifetime of exciton is as short as several nanoseconds in case of high-quality bulk semiconductors.

Radiative recombination mechanism depends not only on crystal temperature but also on actual density of the photo-generated carriers. As seen in a schematic diagram (Figure 1-3), we can define three carrier density regimes, in which different quasi-particles are responsible for the dominant radiative recombination mechanisms, (1) the dilute bozon gas regime, in which the exciton density (n) is as low as 10^{16} cm^{-3}. Under this situation, the decay of free- and/or bound- exciton is the main radiative recombination channel. (2) The intermediate density range (n~10^{17} cm^{-3}), in which excitonic molecules (bi-exciton) and inelastic excitonic scattering processes contribute additional decay mechanisms to the characteristics of luminescence spectra. (3) The high-density range (n~10^{18} cm^{-3}), where screening of the Coulomb interaction leads to exciton ionization. In this range, all optical transitions originate from the radiative decay of free carriers in a dense EHP. Figure 1-3 also shows that below a certain critical temperature (T_C) and under suitable conditions phase transitions may occur, like the Bose condensation of excitons[25] or the transition from EHP to electron-hole liquid (droplets).[26]

There is a long history in the studies on optical characterization of ZnO. Considering only reports, in which radiative recombination processes under strong excitation conditions are discussed, the first observation of ultraviolet lasing was reported in 1966 with using high-energy electron beam as an excitation source excitation at a cryogenic temperature.[27] As for laser action upon optical pumping, the first observation was reported by Reynolds *et al*. in 1996.[28] Stimulated emission from optical pumped ZnO bulk crystal has been intentionally investigated in 1970's in order to understand the radiative recombination mechanism in dense excitonic system. The stimulated emission mechanisms such as exciton-longitudinal optical phonon (LO) interaction[29], exciton-electron interaction[30], exciton-exciton scattering[31,32], and exciton-molecule (bi-exciton)[33] have been observed at cryogenic temperatures under high excitation conditions.

These stimulated emission processes, however, quench rapidly with increasing temperature due to poor crystalline quality so that room temperature stimulated emission had not been reported until 1997. We observed excitonic stimulated emission from ZnO epitaxial films upon optical pumping at room temperature (See Chapter 2).[34] Exciton-exciton collision process dominates the stimulated emission, giving rise to a very low threshold (24 kW/cm^2). This triggered the intensive research of thin film growth. The observation of laser action at room temperature was reported independently by Bagnall *et al.*[35], and us.[36] In our case, threshold was as low as 40 kW/cm^2. This threshold was the lowest one among the reported thresholds in ZnO and even in GaN and related materials at that time.[37] One can expect that ZnO is a possible candidate for fabrication of ultraviolet LEDs and LDs once a certain quantum well structure and *p*-type material are available.

1.3. Laser Molecular-Beam Epitaxy

Laser molecular-beam epitaxy (L-MBE) is a process, especially useful for epitaxial layer-by-layer growth of metal oxide thin films directly from sintered ceramic targets.[5] L-MBE was first developed by Cheug *et al.*, and was mostly employed for sequential deposition of compound semiconductors.[38] Our group have been improving the L-MBE systems and operating conditions. We could establish the epitaxy technique of oxide thin films having high crystalline quality comparable to that of semiconductor. L-MBE has some advantages for fabricating oxide heterostructures, which never be obtained simultaneously with other growth methods such as MBE, sputtering and metal organic chemical vapor deposition (MOCVD), as follows. (1) High energy density, (2) wide applicable pressure range, (3) simple setup. A pulsed laser can condense energy into a very short time period, and can achieve very high peak energy. Thus, material of a sintered target can be evaporated without any change of the composition ratio if the vapor pressures of each element are not so high at a growth temperature. The instantaneous energy of a pulsed laser can be much higher than a continuous wave (cw) mode laser at the same average power. This is the biggest advantage of L-MBE for fabricating metal oxide thin films, which generally have a high melting point. Especially, an UV laser such as an excimer laser is useful for achieving a high energy density because the laser light is absorbed in a smaller volume near the surface due to relatively large absorption coefficient.

In contrast to semiconductors and metals, metal oxide films have to be grown at a high oxygen partial pressure. In order to achieve the desired oxygen stoichiometry in these materials, it is necessary to use a wide range of oxygen partial pressures (P_{O2}) from ultrahigh vacuum (UHV) to atmospheric pressure and substrate temperatures (T_s) ranging from room temperature to well over 1000 °C. Metal oxide film growth mode and characteristic electrical properties are sensitive to these two process parameters. A deposition system capable of operation over wide ranges of P_{O2} and T_s , and compatible with *in-situ* reflection high energy electron diffraction (RHEED) monitoring is required for the study of oxide thin film growth mechanisms, for fabricating higher quality films, and for finding new applications for the various crystal phases. A significant advantage of L-MBE is the ability to change the oxygen pressure easily during deposition from UHV to mTorr range by adjusting the gas inlet and exhaust valves and thus controlling the stability of crystal phases and the oxygen stoichiometry of the deposited films. This feature is particularly useful for making heterojunctions of various materials by changing the P_{O2} depending on the material being grown. The ability to pump the chamber to UHV level is important for maintaining a clean deposition environment and allows various kinds of *in-situ* surface analysis instrument.

The L-MBE setup is very simple as shown in Fig. 1-4. A system basically requires only an excimer laser and an UHV chamber so that any evaporator source or plasma generating systems is not necessary

inside the deposition chamber, resulting in a clean atmosphere during the deposition without any degas contaminants.

In our case, a growth chamber with size of 50 *l* is evacuated by a turbo molecular pump (Varian Co., Ltd., V700) and combined with a loading chamber across a gate valve. The loading chamber is used for sample preparation and help to maintain a low base pressure in the main deposition chamber, which is only exposed to high-purity oxygen. Background pressure is as low as 10^{-10} Torr. Residual gases are mostly consisted of oxygen, hydrogen and a bit of oxy-carbonates, judging from analyses using a quadruple mass spectrometer. Chamber pressure is always monitored by an ion gauge or a pirani gauge.

Laser light can pass through a transparent solid, liquid or gas at the laser light wavelength. It enables us to make films in wide pressure range, from ultra-high vacuum (UHV) to atmospheric pressure. An infrared (IR) lamp (1kW halogen lamp) focused on the backside of the sample holder is used for substrate heating. The sample holder is made of inconel-600 (a metal alloy comsisted of Ni, Cr, Fe, and Mn), which has strong resistance to oxidation. Single-crystalline substrates are mounted on the holder by metal clamps. An optical pyrometer located outside the chamber is used for measuring the substrate temperature through a pyrex glass view port. The pyrometer detection wavelength is 2 μm and had a measurement range of 170–1400° C. Measurement spot size on the sample surface is about 2 mm in diameter.

The excimer laser pulses can be introduced into the vacuum chamber through a quartz window to ablate a ceramic target, which is designed as small as 20 mmϕ × 5 mm*t*. The target is mounted on a SUS holder using silver paste and then placed on the rotatable carrousel. Multiple targets up to 4 can be placed in the deposition chamber. It is possible to fabricate heterostructures and superlattices by simply changing the target during PLD.

The laser-solid interactions can be divided into two parts. The first part is the interaction of the laser beam with the target surface. The laser beam is absorbed and the target material is thermally evaporated. The second part is the interaction of the laser beam with the evaporated materials. Laser pulses generate plasma with oxide particles (both charged and neutral ones), high-energy ions, and electrons near the target. Next, the evaporated materials expand adiabatically and collide with each other or environmental oxygen gases. Only some ions are neutralized during collision processes in this region because the mean free path of evaporated species is much larger than the distance between the target and the substrate surface in low oxygen pressure such as 10^{-6}~10^{-5} Torr. Finally, the evaporated species arrive at the substrate and condense on the substrate surface. The atomic species reach the substrate surface without vapor phase oxidation. The atomic species diffuse and react with the O atoms to form a metal oxide (MO) phase on the substrate surface. This reaction proceeds kinetically with the participation of the O atoms.

The mobility of the absorbed atoms can be high because the supply of oxygen atoms is small. The high mobility can be useful for achieving two-dimensional growth.

1.4. Outline of the Thesis

Title of the present thesis is “Quantum Structures and Ultraviolet Light Emitting Devices Based on ZnO Thin Films Grown by Laser Molecular-Beam Epitaxy”. Quantum structures based ZnO epitaxial films were grown on oxide substrates by laser molecular-beam epitaxy technique and the optical and electronic properties were investigated.

This thesis is composed of eight chapters. Background and general interest for this work are described in Chapter 1. In Chapter 2, epitaxial growth of ZnO nanocrystalline films on sapphire substrates and the optical properties of the films are discussed by focusing excitonic photoluminescence properties under strong excitation conditions at room temperature. The observation of ultraviolet laser action in naturally formed longitudinal cavity is also presented. Chapter 3 describes epitaxial growth of ZnO single-crystalline films on sapphire substrates and structural characterizations, showing systematic studies for improving the electronic properties. Chapter 4 discusses band gap engineering based on ternary alloys, $Mg_xZn_{1-x}O$ and $Zn_{1-x}Cd_xO$. Thermal stability of the supersaturated $Mg_xZn_{1-x}O$ is also discussed to examine applicability for actual device applications. In Chapters 5, fabrication of ZnO/$Mg_xZn_{1-x}O$ superlattices and demonstration of quantum size effects are described. Another substrate is used instead of sapphire to improve the film quality. The electronic and optical properties of ZnO films grown on lattice-matched $ScAlMgO_4$ (0001) structures are presented in Chapter 6. Combining all these results, high-throughput optimization of doped and alloy films and parallel syntheses of quantum well structures are performed with the aid of the combinatorial approach, presented in Chapter 7. In Chapter 8, the results are discussed generally, summarizing and drawing conclusions.

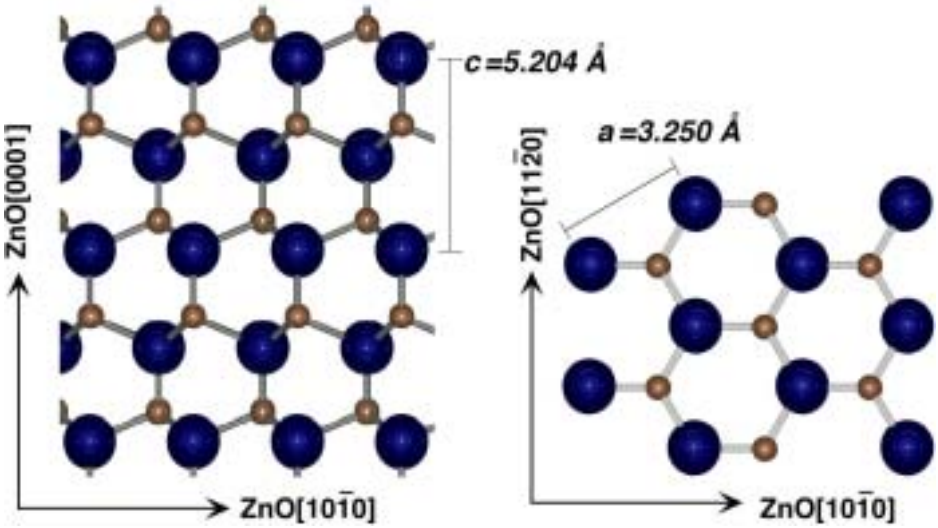

Figure 1-1. Crystal structure of ZnO (wurtzite). The left and right figures show the views from the directions of ZnO[11-20] (left) and ZnO [000-1] (right), respectively. Large and small circles indicate oxygen and ZnO ions, respectively.

Table 1-1. Basic material properties and typical growth temperatures for the candidate materials for a short wavelength laser diode.

Material	E_g (eV)	a (Å)	c (Å)	m_e	m_h	μ	ε	E_b^{ex} (meV)	r_B (Å)	T_m (° C)	T_g (° C)
ZnO (WZ*)	3.37	3.25	5.20	0.28	1.8	0.31	8.5	60	18	1970	~500
GaN (WZ)	3.4	3.19	5.19	0.2	0.8	0.16	9.5	24	31	1700	~1000
ZnSe (ZB#)	2.7	5.67	-	0.12	0.42	0.14	9.1	22	35	1520	~400
ZnS (ZB)	3.6	5.41	-	0.39	0.42	0.2	8.3	40	22	1850	~400

* wurtzite, #zincblend

E_g: band gap at room temperature
a and c: lattice constants
m_e and m_h: effective masses of electrons and holes
μ: reduced exciton mass
ε: dielectric constant
E_b^{ex}: exciton binding energy
r_B: Bohr radius
T_m: melting point
T_g: typical growth temperature

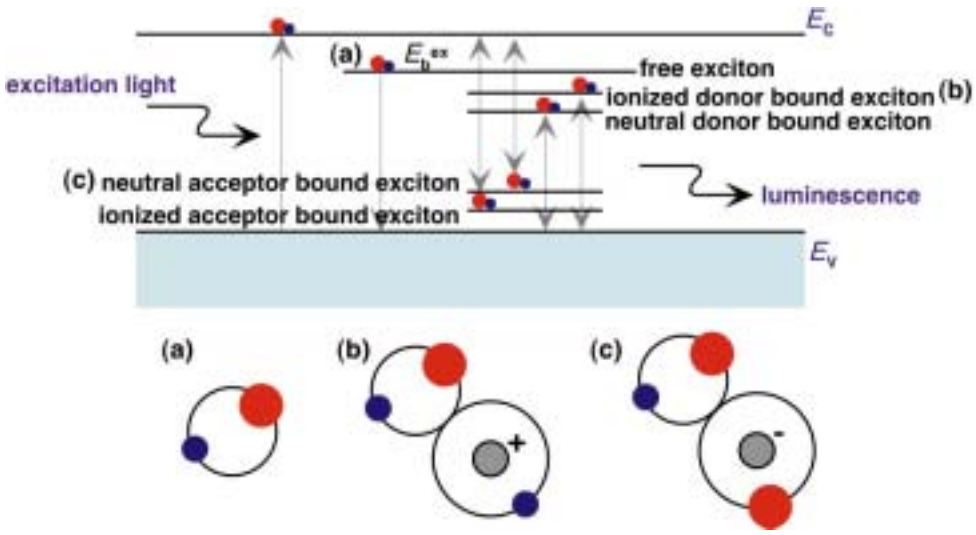

Figure 1-2. Schematic band diagram explains various kinds of excitonic radiative recombination processes resulting in spontaneous photoluminescence such as, (a) free exciton, (b) donor bound exciton, and (c) acceptor bound exciton luminescence.

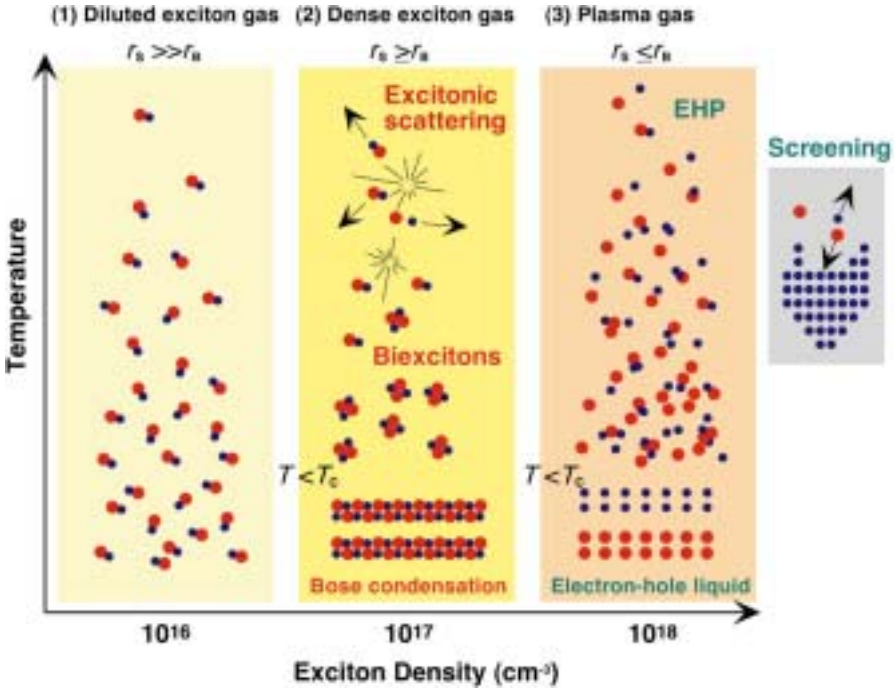

Figure 1-3. Schematic illustration of radiative recombination mechanisms, which are categorized to three carrier density regimes (See text in details).

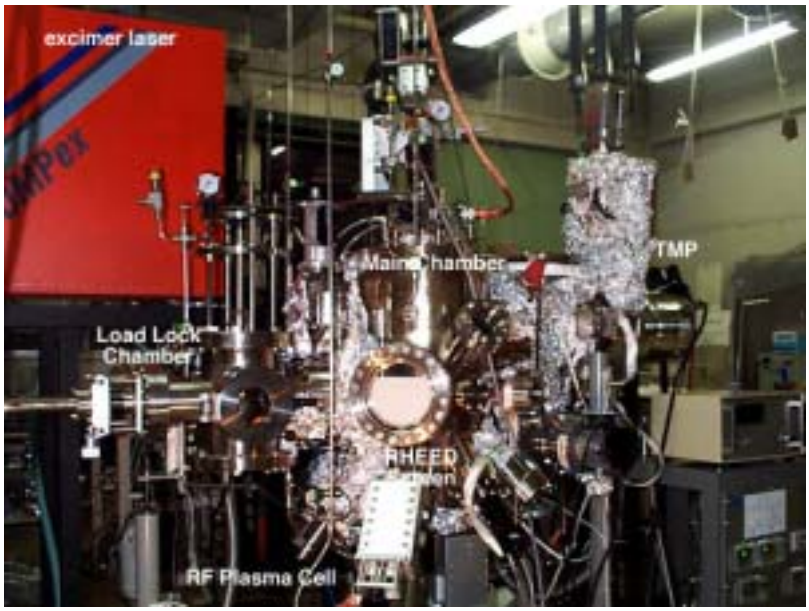

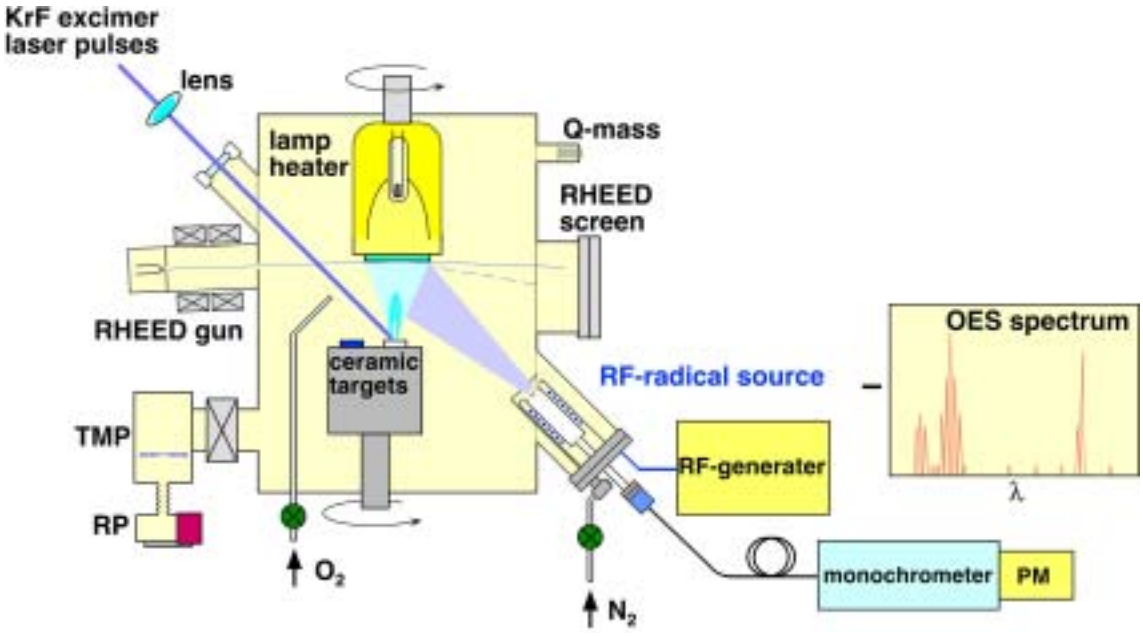

Figure 1-4. A photograph of the L-MBE setup in our laboratory (top) and schematic illustration of the L-MBE system equipped with RHEED and RF-plasma source (bottom).

References

[1] M. A. Haase, J. Qui, J. M. Puydt, and H. Cheng, Appl. Phys. Lett. **59**, 1272 (l991).

[2] S. Nakamura, T. Mukai, and M. Senoh, Appl. Phys Lett. **64**, 1687 (1994).

[3] S. Nakamura, M. Senoh, S. Nagahama, N. Iwasa, T. Yamada, T. Matsushita, Y. Sugimoto, and H. Kiyoku, Appl. Phys. Lett. **69**, 4056 (1996).

[4] H. Amano *et al*., Appl. Phys. Lett. **48**, 353 (1986).

[5] S. Nakamura *et al*., Jpn. J. Appl. Phys. **31**, 2883 (1992).

[6] S. Nakamura *et al*., Jpn. J. Appl. Phys. **31**, L1457 (1992).

[7] A. Usui, H. Sunakawa, A. Sakai, and A. A. Yamaguchi, Jpn. J. Appl. Phys. **36**, L899 (1997).

[8] J. G. Bednorz and and K. A. Muller, Z. Phys. B **64**, 189 (1986).

[9] See, for example, K. Chahara, T. Ohono, M. Kasai, and Y. Kozono, App1. Phys. Lett. **63**, 1990 (1993)., and S. Jin *et al*. Science **264**, 413 (1994).

[10] H. Koinuma, MRS Bull. **19**, 21 (1994).

[11] M. Kawasaki, K. Takahashi, T. Maeda, R. Ryuta, M. Shinohara, O. Ishiyama, T. Yonezawa, M. Yoshimoto, and H. Koinuma, Science **266**, 1540 (1994).

[12] H. Koinuma, M. Kawasaki, and M. Yoshimoto: Mat. Res.Soc. Symp. Proc. **474** (1997) 303.

[13] R. Tsuchiya, M. Kawasaki, H. Kubota, J. Nishino, H. Sato, H. Akoh, and H. Koinuma, Appl. Phys. Lett. **71**, 1570 (1997).

[14] See for example, F. A. Kroger *et al*., *The Chemistry of Imperfect Crystals, vol. 2*, (North-Holland, 19XX), p. 743.

[15] D. C. Look, J. W. Hemsky, J. R. Sizelove: Phys. Rev. Lett. **82** (1999) 2552.

[16] T. Minami, H. Sato, H. Nanto and S. Tanaka, Jpn. J. Appl. Phys. **23**, L280 (1984).

[17] T. Minami, H. Sato, H. Nanto and S. Tanaka, Jpn. J. Appl. Phys. **24**, L781 (1985).

[18] T. Minami, H. Sato, H. Nanto and S. Tanaka, Jpn. J. Appl. Phys. **25**, L776 (1986).

[19] J. Hu and R. G. Gordon, Sollor Cells **30**, 437 (1991).

[20] G. Blatter and F. Greuter: Phys. Rev. **B33** (1985) 3952.

[21] T. K. Gupta, J. Am. Ceram. Soc. **73**, 1817 (1990).

[22] See for example, Y. Yamada, T. Mishima, Y. Masumoto, Y. Kawakami, J. Suda, S. Fujita, and S. Fujita, Phys. Pev. **B52**, 2289 (l995)., and S. Chichibu, T. Sota, K. Wada, S. Nakamura, J. Vac. Sci. Technol. B **16**, 2204 (1998).

[23] H. Wenisch, M. Behringer, M. Fehrer, M. Klude, A. Isemann, K. Ohkawa, and D. Hommel, Jpn. J. Appl. Phys. **38**, 2590 (1999).

[24] S. Nakamura, M. Senoh, S. Nagahama, N. Iwasa, T. Yamada, T. Matsushita, H. Kiyoku, Y. Sugimoto, T. Kozaki, H. Umemoto, M. Sano, and K. Chocho, Jpn. J. Appl. Phys. **37**, L627 (1998), and S. Nakamura, M. Senoh, S. Nagahama, T. Matsushita, H. Kiyoku, Y. Sugimoto, T. Kozaki, H. Umemoto, M. Sano, and T. Mukai, Jpn. J. Appl. Phys. **38**, L226 (1999).

[25] D. W. Smoke, J. P. Wolfe, and A. Mysyrowicz, Phys. Rev. Lett. **64** (1990) 2543.

[26] See, for example, *Electron-hole droplets in semiconductors*, edited by C. D. Jeffries and L. V. Keldysh, (North-Holland, 1983).

[27] F. H. Nicoll, Appl. Phys. Lett. **9**, 13 (1966).

[28] D. C. Reynolds, D. C. Look, and B. Jogai, Solid State Comm. **99**, 873 (1996).

[29] G. H. Jensen and E. Mollow, Phys. Stat. Sol. **B60**, 169 (1973).

[30] S. Iwai and S. Namba, Appl. Phys. Lett. **19**, 41 (1971)., and J. M. Hvam, Phys. Rev. **B14**, 4459 (1971).

[31] J. M. Hvam, Solid. State. Commun. **12**, 95 (1973)., and Phys. Stat. Sol. B **63**, 511 (1974).

[32] C. Klingshirm, Phys. Stat. Sol. **B71**, 547 (1975).

[33] H. Schrey and C. Klingshirm, Solid. State. Commun. **28**, 9 (1978).

[34] P. Yu, Z. K. Tang, G. K. L. Wong, M. Kawasaki, A. Ohtomo, H. Koinuma, and Y. Segawa, *23rd International Conference on the Physics of Semiconductors*, edited by M. Scheffler and R. Zimmermann (World Scientific, Singapore, 1996), p. 1453.

[35] D. M. Bagnall, Y. F. Chen, Z. Zhu, T. Yao, S. Komiya, M. Y. Shen, and T. Goto, Appl. Phys. Lett. **70**, 2230 (1997).

[36] Y. Segawa, A. Ohtomo, M. Kawasaki, H. Koinuma, Z. K. Tang, P. Yu, and G. K. L. Wong, Phys. Stat. Sol. **B202**, 669 (1997).

[37] M. Kawasaki, A. Ohtomo, R. Tsuchiya, J. Nishino, and H. Koinuma, Mat. Sci. Soc. Symp. Proc. **474**, 303 (1997).

[38] J. T. Cheung, G. Niizawa, J. Moyle, N. P. Ong, B. M. Paine, and T. Vreeland Jr., J. Vac. Sci. Techno1. A**4**, 2086 (1986).

Chapter 2. Excitonic Ultraviolet Laser Emission at Room Temperature from Naturally Made Cavity in ZnO Nanocrystalline Thin Films

Abstract

Hexagonally shaped ZnO nanocrystalline thin films were fabricated on sapphire (0001) substrates by laser molecular-beam epitaxy. Nanocrystalline structure was investigated by atomic force microscopy and transmission electron microscopy. Epitaxial growth of ZnO nanocrystalline thin films on sapphire substrates was found to occur in a spiral and grain growth mode. The grain growth mode was interrupted by taking higher order epitaxial relationship of oxygen sub-lattice units between ZnO and sapphire into account. Nanocrystal size could be tuned from 50 to 200 nm by controlling film thickness, growth conditions and stoichiometry of the target. The films having small nanocrystal size of about 50 nm showed excitonic stimulated emission having peak energy of 3.2 eV at room temperature with a very low threshold (24 kW/cm^2). Mode transition from excitonic stimulated emission to electron-hole-plasma appeared above another threshold (50 kW/cm^2). Well-defined Fabry-Perot cavity mode was observed in the emission spectra measured from side edge of the film. It was concluded that the grain boundaries between nanocrystals serve not only as potential barriers confining excitons but also as cavity mirrors.

2.1. Introduction

Metal oxides have recently shown such excitonic properties as high temperature superconductivity and colossal magnetoresistance, tempting us to expect the birth of a new field of microelectronics based on hetero-epitaxial oxide structures.[1] As a process especially suitable for atomic scale control of the epitaxy of metal oxides, we have developed laser molecular-beam epitaxy (MBE)[2] and demonstrated that it can be used for manufacturing quantum structures and exploring novel properties of oxides.[3] As a novel function of metal oxides, we have recently reported an excitonic laser action at room temperature in ZnO thin films composed of hexagonally shaped nanocrystalline thin films.[4,5]

Very recently, a laser diode based on III-nitrides has achieved continuous-wave blue lasing at room temperature.[6] Some critical issues, however, have still been remaining to be solved for practical use. In widegap semiconductors, high carrier concentration is needed to achieve a gain enough high to give laser action in electron-hole plasma (EHP) process[7], which is a laser operation mode in a high threshold for lasing[8], unless much more efficient lasing process is taken into account. Moreover, it is difficult to fabricate *p*-type materials having low resistivity in widegap semiconductors. In III-nitride laser diode, most of the applied power is needed consumed in the *p*-type laser and the interface with contact metal, resulting in Joule heating.

In order to decrease threshold for lasing, current trend in compound semiconductor laser is concentrated on the fabrication of low-dimensional structures such as quantum well, wire and dot.[9] This is because the quantum size effect modifies the profile of density of states so that the transfer integral at the band-edge becomes much larger than that of bulk semiconductor, facilitating efficient stimulated emission. The use of excitonic recombination is another approach to enable intrinsically large matrix element because of its bosonic nature. Therefore, the threshold of excitonic laser action was predicted[10] and verified[11] to be much lower than conventional EHP lasers.

For achieving efficient excitonic laser action at room temperature, exciton binding energy (E_b^{ex}) has to be much larger than the thermal energy at room temperature (26 meV). In this viewpoint, ZnO is a suitable material for ultraviolet light emission. ZnO has room temperature band gap of 3.37 eV and has a much larger E_b^{ex} (60 meV) than those of ZnSe (22 meV), ZnS (40 meV), and GaN (25 meV). However, stimulated emission from ZnO bulk crystals has been observed only at cryogenic temperatures and it quenched rapidly at higher temperatures probably due to crystalline defects.[12] It should be possible to overcome these problems by fabricating high-quality ZnO thin films with using modern oxide epitaxial technique.

In this chapter, fabrication of ZnO nanocrystalline films and optical properties, including excitonic lasing at room temperature, are described.

2.2. Experimental

ZnO films were grown by laser MBE (compact laser MBE system; Pascal Co., Ltd.) equipped with reflection high-energy electron diffraction (RHHED. The background pressure was better than 1×10^{-9} Torr. Ceramic ZnO targets (5N) were placed in the chamber and ablated with KrF excimer laser (248 nm, 10 Hz, 30 ps) pulses focused into a spot of 0.5 × 2mm with a fluence of 0.6 Jcm^{-2}. Sapphire (0001) substrates (14 mmϕ × 0.4 mmt), polished on the both sides, were mounted on a holder placed 50 mm away from the target and heated by an infrared lamp focused on the backside of the holder. Pure oxygen (6N) was introduced into the chamber with a pressure of 1×10^{-6} Torr. Before the film deposition, the substrate was heated to 750° C in 1×10^{-6} Torr of oxygen for 30 min to remove carbon contaminants from the surface. The film was deposited at a temperature of 550° C. The film thickness was varied from 50 to 500 nm with a deposition rate of 5×10^{-3} nm per pulse. As-deposited films were annealed at 550° C for 1 h in 1 atm of oxygen in the chamber and cooled down to room temperature. By this annealing, we expected to reduce such defects as interstitial Zn and oxygen vacancy.

The structure of the films was investigated by *in-situ* RHEED, low energy electron diffraction (LEED), a four circle x-ray diffraction apparatus (XRD, Philips, X'-pert MRD). The surface morphology of the films was observed by means of contact-mode atomic force microscopy (AFM, Seiko, SPI-3700) in air. Further surface observation was carried out by mean of an UHV-scanning tunneling microscope (STM, Omicron, Compact lab.). Cross-sectional view of the film is examined by a transmission electron microscope (TEM, Hitachi, H-9000). The TEM samples were prepared by focused Ga ion beam (FIB, Hitachi, FB-2000LP) to expose the cross-sections.

Optical properties were characterized by using photoluminescence (PL) spectroscopy with an excitation by 325 nm line of a cw He-Cd laser beam and standard absorption and reflectance spectroscopies at temperature ranging from 2 to 295 K. Frequency tripled pulses (355 nm, 10 Hz, 15ps) from a mode-locked Nd: YAG laser (Coherent) was used for lasing experiments. The laser beam was focused with a cylindrical lens into a stripe on the sample surface at normal incidence. Measurements were performed at various stripe lengths, which could be adjusted by changing a slit length. Emission spectra were taken with a monochrometer (SPEX 1680) equipped with a photomultiplier and a boxcar integrator.

2.3. Results and Discussions

2.3.1. Epitaxial structure of ZnO films grown on sapphire (0001)

X-ray diffraction pattern of the films showed only ZnO (000*l*) peaks together with the sapphire (000*l*) peaks, as seen in θ-2θ pattern for a 200 nm-thick film shown in Fig. 2-1 (a). Φ-scans for asymmetric planes of the ZnO (10-11) and the sapphire (11-23) revealed in-plane orientation with 30°-rotation to the substrate as shown in Fig. 2-1 (b). When 2 μm-thick film obtained under optimal growth condition was measured by high-resolution XRD, full width at half maximum (FWHM) for the ZnO (0002) Bragg peak and for rocking curve was as small as 50 and 210 arcsec, respectively, indicating very high crystallinity. In-plane mosaicness (twisting) of the same film was evaluated to be 470 arcsec by Φ–scan of ZnO (10-11). The in-plane crystal orientation relationship was again found to be ZnO [11-20]//sapphire [10-10] from RHEED and LEED observations (Figures 2-2 and 2-3 show typical diffraction patterns of RHEED and LEED, respectively) as well as x-ray pole figure. This orientation relationship is also the case for GaN/sapphire.[13] A direct lattice mismatch between ZnO and sapphire is as large as 18.3 %, if oxygen sub-lattice units are taken into account.

Figure 2-4 (a) and (b) shows AFM images of 200 nm and 55nm-thick films, respectively. As more clearly seen in Fig. 2-4 (a), hexagonally shaped nanocrystals assembled closely each other. Step with a height of about 0.5 nm, corresponding to the *c*-axis length of ZnO, and atomically flat terraces are clearly seen on each grain. The center of the grain shows screw dislocation, indicating that these crystals grew in a spiral growth mode. This growth mode provides a chance for the crystal to grow in a step-flow mode at each step edge with under thermal equilibrium conditions, resulting in high crystallinity films. The facets of ZnO hexagons correspond to the {10-10} plane, which is known to have lower free energy than the other {11-20} plane.[14] This faceted structure is also strong evidence for the fact that our growth condition is sufficient for achieving thermal equilibrium at the growth surface. When the film thickness was regulated as small as 50 nm, apparent grain size was approximately 50 nm, as shown in Fig. 2-4 (b). In any case, the size distribution of nanocrystals are about 30 %, indicating that the nanocrystal size distribution is much more sharp compared with so-called quantum dots in III-V materials formed by other growth techniques.[15,16,17] Figure 2-5 shows a STM image of the 55 nm-thick film. The image has a similar morphology as the AFM image shown in Fig. 2-4 (b). A purely hexagonally shaped nanocrystal is clearly seen at the center of the figure. The side of the nanocrystals are atomically flat and perfectly parallel to the ZnO {11-20} direction. The surface on the top of the nanocrystal is flat except for a small corrugation. The depth of pin-poles between the nanocrystals is about 3 nm, corresponding to five to six times of the ZnO *c*-axis length. There is a small hollow at the center of the nanocrystal, corresponding to the center of a spiral dislocation. When we measured scanning tunneling spectroscopy (STM) on the top of the nanocrystal, band gap of about 3 eV clearly was observed in the tunnel spectrum. Judging from STS spectra, a band bending at the surface was estimated to be about 1 eV.

Figure 2-6 shows a cross-sectional bright field TEM image of a film having thickness of 50 nm. There can be clearly seen many grain boundaries (indicated by arrows) running parallel from the interface between ZnO and sapphire to the film surface. The average spacing of grain boundaries in TEM image is approximately 50 nm, corresponding to the nanocrystal size seen in AFM image. Therefore, this ZnO film consists of close-packed hexagonal columns, having a volume, which can be as small as about $\{50\ (\mathrm{nm})\}^3$.

2.3.2. Formation of nanocrystalline structures

Figure 2-7 shows lateral nanocrystal size evaluated from AFM observation as a function of film thickness. When we used a pre-ablated ZnO targets, the apparent nanocrystal size evaluated from AFM images increased linearly with the film thickness as indicated by closed circle along with a linear fit line (solid line). When the film thickness was smaller than 70 nm, the lateral nanocrystal size could be reduced further by using a fresh ZnO target (triangles surrounded by solid line). A ZnO target was gradually deoxidized by the laser irradiation and obtained a metallic color instead of the original white color of ceramic. This difference in lateral nanocrystal size is considered to be caused by kinetic effect, where well-oxidized target produces precursors having less diffusivity on sapphire surface, resulting in more nucleus formation. When partly reduced target is used, precursors having high diffusivity form fewer nucleuses and induce coalescence to result in larger nanocrystals.

The results of time of flight mass spectrometry (TOF-MASS) analyses partly supported the above speculation. A high purity Zn metal and fresh ZnO ceramic target used the deposition experiments were ablated by N_2 laser (337.1 nm, 2 ns) and time of flight of the ablated species were measured. This technique is relatively popular as a mass analysis of organic materials, and an apparatus is commercially available. Figure 2-8 shows TOF-MASS spectra taken from (a) Zn and (b) ZnO. Zn isotope signals are clearly observed in the spectrum, thus this method can be applicable for mass analyses of ablation species. On the other hands, number of oxidized particles such as ZnO^+, Zn_2O^+, and etc. is seen at the ZnO as shown in Fig. 2-8 (b). This can be strong evidence that the ZnO-related species are provided to the substrate surface. In case of MBE growth, this advantage of highly oxidizing and high kinetic energies of precursors can never be obtained. As can be seen in Fig. 2-9, ion intensity of both $^{64}Zn^+$ and $^{80}ZnO^+$ gradually increases with increasing number of laser shot, however, the intensity of $^{64}Zn^+$ ion increases much rapidly compared with that of $^{80}ZnO^+$, indicating laser irradiation damage resulting in much higher ablation rate and oxygen deficiency. Thus, it is concluded that the target surface condition strongly affects nanocrystal size.

Here we explain formation of the nanocrystal with taking higher order epitaxy[18,19] into account. The hexagonal oxygen sublattice of sapphire, which is rotated by 30° from the principal hexagonal unit cell ($a_{sapphire}$=0.4759 nm) of this compound, has a lattice constant ($a'_{sapphire}=a_{sapphire}/\sqrt{3}$) of 0.2748 nm and has a lattice mismatch of 18.3 % compared with a'_{ZnO}=0.3250 nm. If we take higher order matching into account, 11 times a_{ZnO} has excellent matching with 13 times $a_{sapphire}$ with a mismatch of 0.085 %. If ZnO matches to sapphire, lattice parameter of the matching unit will be 6.19 nm. When we supply species on the sapphire surface, ZnO islands nucleate with keeping this higher order relationship, but the coherency between the nuclei is not necessarily maintained as shown in Fig. 2-10. As these nuclei grow laterally on the sapphire surface, perfect in-plane orientation can be maintained but the grain boundaries between adjacent hexagonal islands should be formed. We presume these incoherent boundaries are the ones seen in AFM and TEM images.

2.3.3. Room temperature excitonic lasing

Temperature dependence of PL spectra is shown in Fig. 2-11. Below 70 K, PL spectra are dominated by *I*-line, which is located at lower energy than *A*, *B*-exciton absorption peak. Thus, *I*-line can be assigned to an emission from a shallow bound exciton state. As the temperature was increased above 80 K, the *I*-line gradually disappeared and a strong new emission peak appeared at the higher energy side. Since the peak energy of this emission is the same as the energy of *A*, *B*-exciton absorption peak, this emission can be assigned to free exciton emission. This emission is still presented up to room temperature with the peak position shifting to lower energy side due to temperature dependence of the band gap.

Figure 2-12 (a) shows the pumping intensity dependence of PL spectra measured at room temperature. PL intensity is also plotted in Fig. 2-12 (b). At lower pumping intensities, spontaneous free exciton emission (E_{ex}) increased linearly as the pumping intensity. At higher pumping intensities, the E_{ex} was gradually replaced by a new emission line denoted as P_2, which is assigned to spontaneous emission generated by exciton-exciton (*ex-ex*) collision process, where one of excitons radiatively recombine to generate one photon and the other exciton is excited into the n=2 state.[20] The P_2-line intensity quadratically increased as shown in Fig. 2-12 (b), agreeing with the second order process. As the pumping intensity was still increased above a threshold of 24 kW cm^{-2}, a new emission, *P*-line, with a much narrower line width appeared at the lower energy shoulder of the P_2-line. The intensity of the *P*-line increased rapidly with increasing pumping intensity, exhibiting a eighth power dependence. The narrow line width of the *P*-line, the super-linear behavior of its intensity, and the suppression of the broad spontaneous emission background indicate that stimulated emission took place. The intensity of the *P*-line started to decrease as the pumping intensity was increased above 50 kW cm^{-2} and a new narrow line

denoted as *N* appeared. The *N*-line can be attributed to the stimulated emission due to radiative recombination of EHP. The peak energy of the *N*-line shifted towards the lower energy side as the pumping intensity was increased. This red shift is attributed to band gap renormalization that can occur at high pumping intensities when the screening of the Coulomb interaction leads to ionization of excitons and the formation of a dense EHP.

The P_2- and *P*-line were not seen in the films having larger nanocrystal size. At lower pumping intensities, only spontaneous E_{ex} emission was present and the *N*-line appeared at larger pumping intensity over a threshold (typically 60 kW cm^{-2}). There is a optimum crystal size of $(50\ nm)^3$ for observing excitonic stimulated emission. The physics behind this observation is not clear, yet. One possible explanation is that the giant oscillator strength effect that can occur in high-quality nanocrystals with dimensions larger than the exciton Bohr radius but smaller than the optical wavelength enable the excitonic stimulated emission in nanocrystalline thin films.[10,21] For thicker films, which also have larger grain size, the superradiance effect becomes weak because the *ex-ex* collision process can not occur.

2.3.4. Formation of natural cavity

When the emission spectrum was measured from the side edge of the film, many peaks with small bandwidth and nearly equal energy separation were observed, suggesting the presence of longitudinal cavity modes. Figure 2-13 shows polarized emission spectra for the electric field perpendicular (*TE*) and parallel (*TM*) to the direction of *c*-axis. As can be clearly seen, spontaneous emission has both components whereas *P*-line was perfectly polarized in the *TE* mode. The inset figure shows mode spacing (ΔE) dependence on the reciprocal excitation stripe length (L^{-1}) for the pumping laser pulses indicating good agreement with a theoretical curve indicated by a solid line. These observations guarantee that we observed ultraviolet lasing at room temperature.

The peculiar fact is that we did observe laser action consistent with a well-defined cavity, although we did not intentionally make a cavity. Moreover, the pumping laser stripe was actually introduced inside the edge of the film in order to avoid the influence of the edges of the film and substrate. Cracks generated by lattice mismatch or thermal expansion mismatch have been suggested to act as laser cavity mirror.[22] However, this phenomenon can not be applied to our results because any of these kinds of structures were not observed by using AFM, TEM and scanning electron microscope (SEM). For II-VI semiconductors, cleaved edge of the specimen on one of the sides could be used as a mirror.[23] For this kind of cavity structure, Fabry-Perot mode can not be as clear as we observed because the photo-generated carriers diffuse to make the distribution of refractive index difference broad. Since the both edges of the excited stripe region worked as laser cavity mirror in our case, there should be sharp

difference of refractive index at the both edges. One of the possible reason for very clear Fabry-Perot node is the described below.

As AFM and TEM results confirmed, the ZnO film is composed of hexagonally shaped nanocrystals and there are distinct grain boundaries between adjacent grains. If excitons are confined in the nanocrystals and cannot travel across the grain boundaries, there must be a discontinuous distribution of carrier density for the grains around the ends of pumping stripe. Since the refractive index is a function of carrier density, the grain boundaries facing different refractive index should be able to act as mirrors. This boundary, which consists of a series of many facets of nanocrystals, should be able to serve as a mirror. The laser action will take place by selecting the mirrors at the right position of the stripe edge so that laser gain is maximum. Inside of the pumping laser stripe, carrier concentration becomes larger resulting in the larger refractive index. The grain boundaries in the cavity can act as barriers for excitons but they have only a small influence except for scattering of light because the refractive index is similar. The optical gain of *P*-line emission at the threshold was evaluated to be g=320 cm^{-1} by gain spectroscopy measurements. If we take into account this number and the refractive index difference of 2 % estimated from the carrier concentration difference, laser emission spectra as shown in Fig. 2-13 could be well fitted by theoretically calculated curve.[24]

When laser light was detected through a pin-pole slit and the specimen was rotated in the plane, the laser light intensity showed clear maximum at every 60° as shown in Fig. 2-14. Since the nanocrystals have a six fold symmetry as shown in Fig. 2-4 (a), the effective cavity formation is limited to the directions, where pumping stripe is aligned perpendicular to the {10-10} crystal planes. This natural cavity formation in hexagonally shaped nanocrystal array suggests a possibility to form a laser cavity without cleavage and etching, *i.e.*, confinement of injection carriers in *p-n* injection by metal contact electrode may be enough to form a laser cavity.

It can be attracting challenge to accomplish a bright flat panel display (FPD) having a monolithic UV-LED and field effect transistor (FET) array, which can selectively excite each red-green-blue (RGB) pixels of fluorescence materials attached in the front of the LEDs. Such FPD would be fabricated easier rather than the conventional FPDs having RGB-LEDs consisted of various compounds. Figure 2-15 shows photographs of demonstration of ultraviolet lasing and RGB-color light emissions. The dye cells are excited by ultraviolet laser light from the optically pumped ZnO film. Beautiful thin laser traces inside the dye cells can be clearly seen. We believe such displays would be available, once ZnO based LEDs and FETs[25] are obtained. In fact, crystalline quality ZnO films can be readily grown even on glass substrate.[26] Moreover, there is the most intensive research to discover efficient fluorescence materials being suitable to various excitation wavelengths[27].

2.4. Conclusions

We have reviewed our progress on ZnO nanocrystal ultraviolet laser research. The structure and formation mechanism of hexagonally shaped nanocrystal was described. Excitonic stimulated emission and laser cavity formation were discussed in relation with the nanocrystal structure.

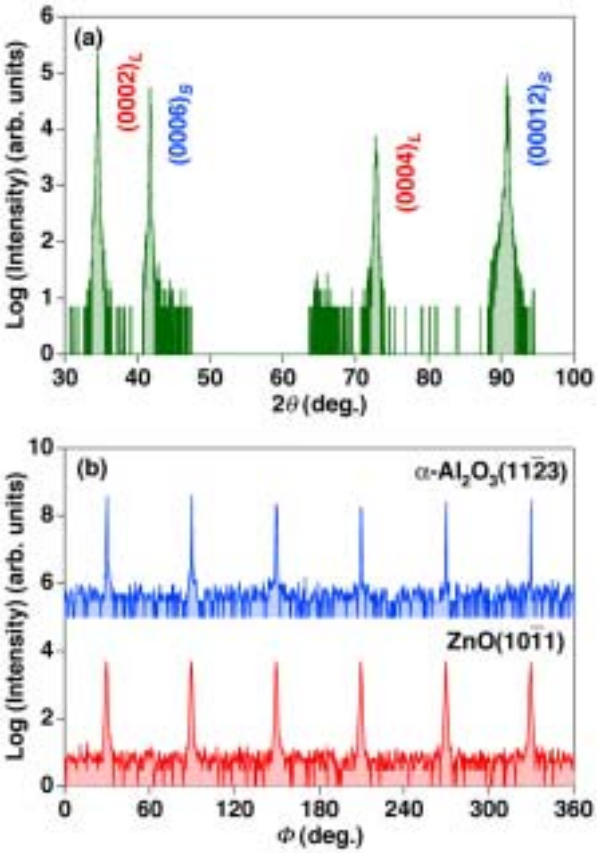

Figure 2-1. (a) θ-2θ x-ray diffraction pattern of 200 nm-thick ZnO film grown on sapphire (0001) substrate. $(000l)_L$ and $(000l)_S$ stand for diffraction peaks of the ZnO (000*l*) and sapphire (000*l*), respectively. (b) Φ-scans of ZnO (10-11) and sapphire (11-23) for the same sample. The epitaxial relationship is determined to be ZnO [0001]//sapphire[0001] and ZnO [11-20]//sapphire [10-10].

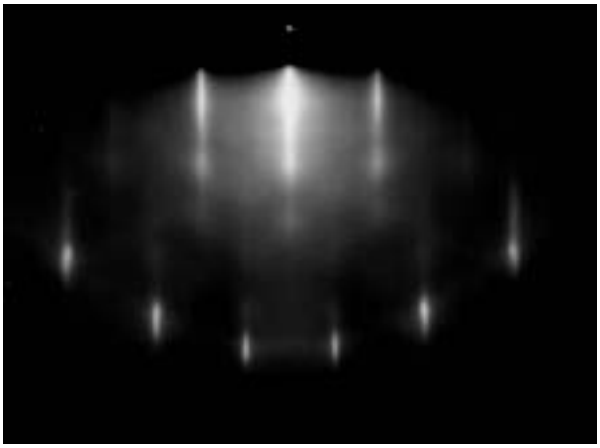

Figure 2-2. A RHEED pattern along the [10-10] direction at a ZnO film grown on sapphire substrate.

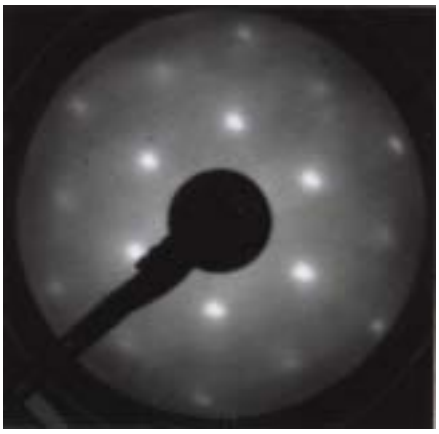

Figure 2-3. A LEED pattern with normal incidence at a ZnO film grown on sapphire substrate.

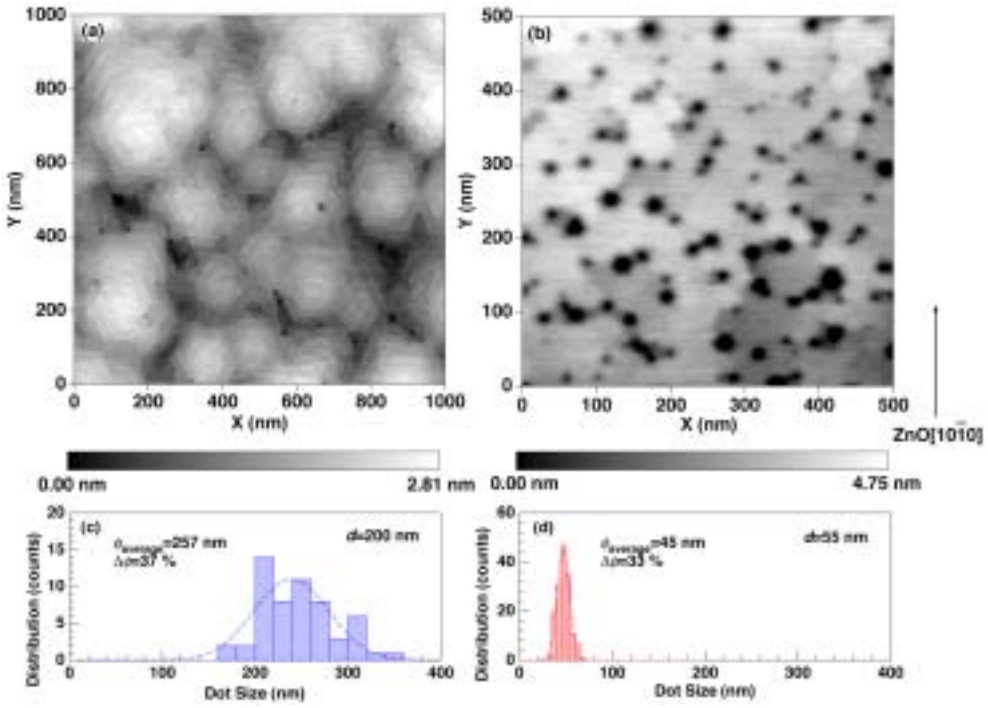

Figure 2-4. AFM images of ZnO films grown on sapphire substrates. (a) 200 nm-thick and (b) 55 nm-thick films. (c) and (d) show distributions of nanocrystal size evaluated from the image of (a) and (b), respectively.

Figure 2-5. A STM image of the film having thickness of 55 nm (image scale: 100 nm × 100 nm) taken with sample voltage of –3.0 V and tunnel current of 0.3 nA. Brack and white level difference is about 5.5 nm.

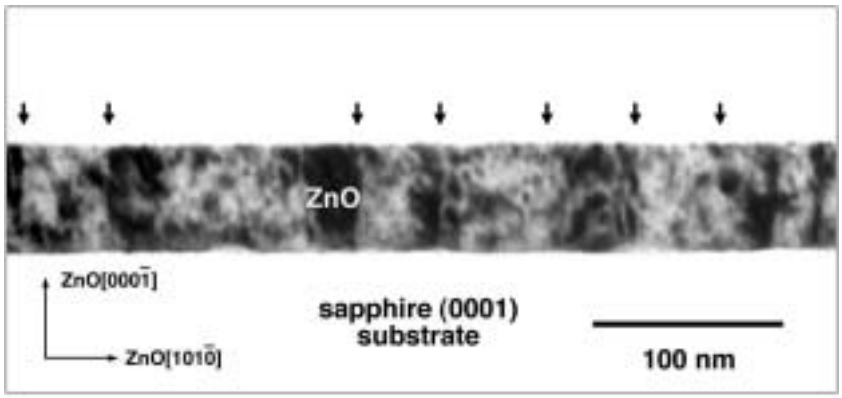

Figure 2-6. A cross-sectional TEM image of the film having thickness of 55 nm (Arrows indicate positions of the incoherent grain boundaries).

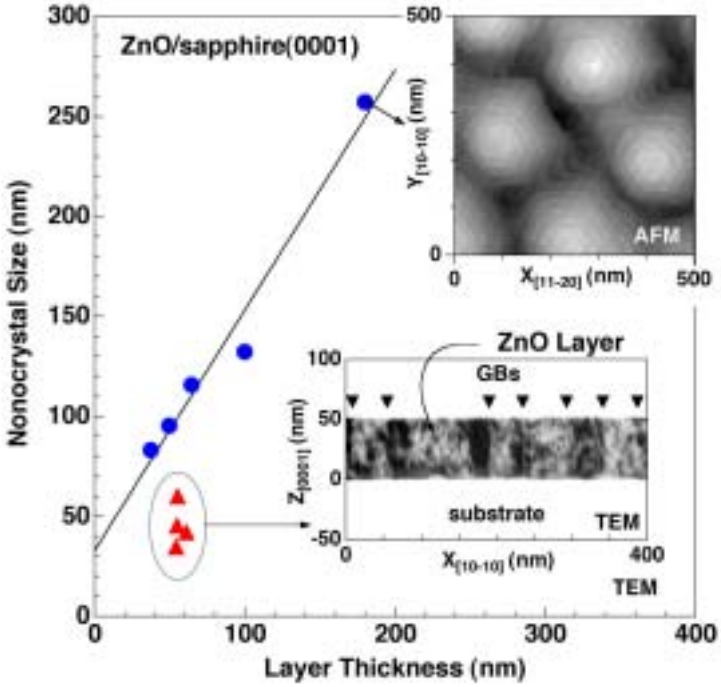

Figure 2-7. Nanocrystal size as a function of film thickness. The films denoted by closed circles and closed triangles were grown with using a fresh target and a reduced target, respectively.

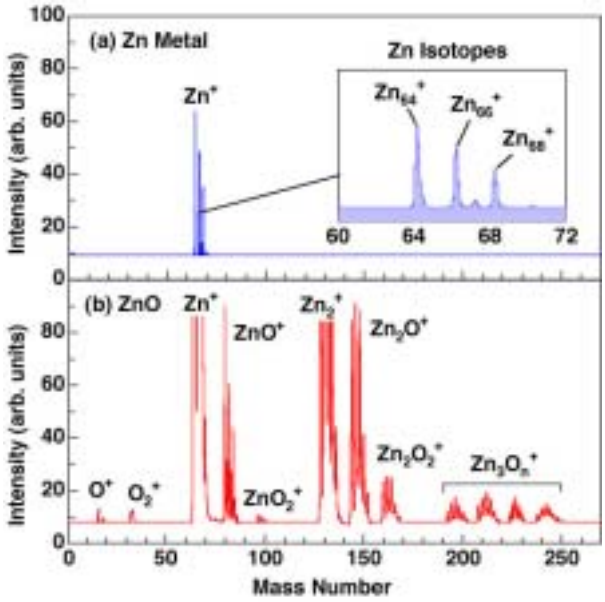

Figure 2-8. Time of flight mass spectra of ablation species from (a) Zn metal and (b) ZnO ceramic target. Only Zn^+ ions are seen from the Zn metal, while number of zinc oxides peaks with Zn-related signals are detected from the ceramic ZnO.

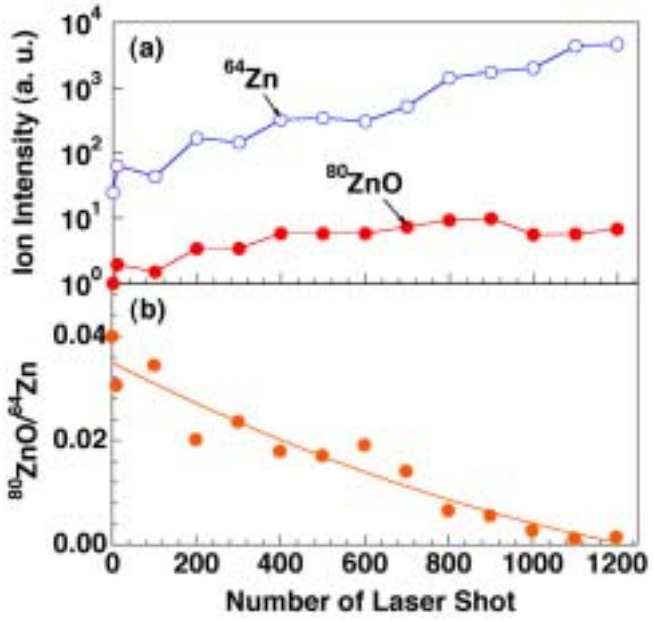

Figure 2-9. (a) Ion intensities of $^{64}Zn^{+}$ and $^{80}ZnO^{+}$ peaks from the ZnO target and (b) intensity ratio of $^{80}ZnO^{+}/^{64}ZnO^{+}$ as a function of number of laser shot.

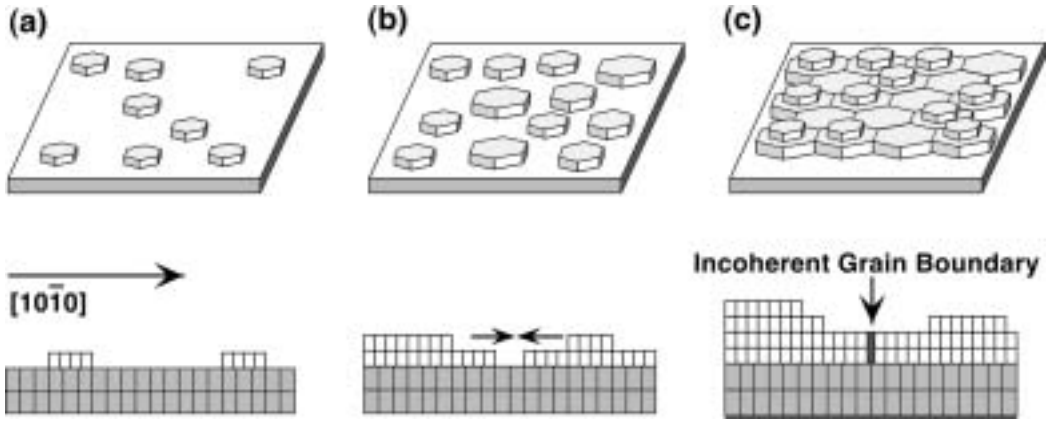

Figure 2-10. Schematic diagram explains the formation of incoherent grain boundaries during higher order epitaxial growth in large lattice-mismatch system. In this case, the higher order relationship was $4a_{film}=3a_{substrate}$, where a_{film} and $a_{substrate}$ are in-plane lattice constants of elementary cells of the film and substrate, respectively. Film growth proceeds as, (a) formation of nuclei, (b) lateral growth of nuclei, and (c) formation of incoherent boundaries.

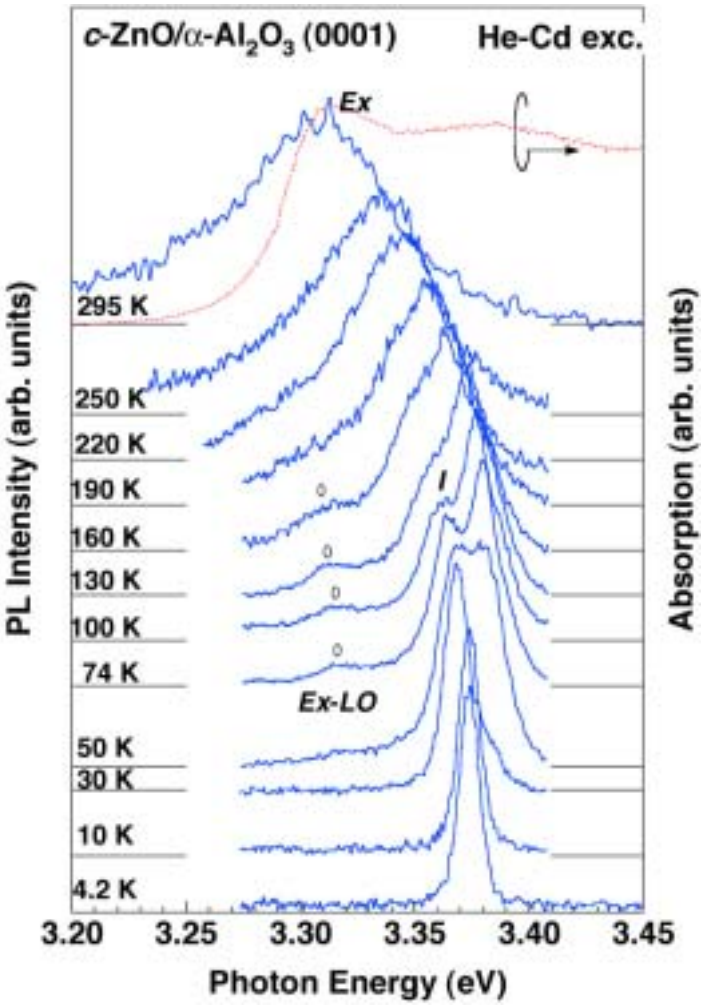

Figure 2-11. Temperature dependence of PL and absorption spectra o a ZnO nanocrystal film. *I*, E_{ex}-*LO*, and E_{ex} are bound exciton emission, free exciton-longitudinal optical phonon replica emission, and free exciton emission, respectively.

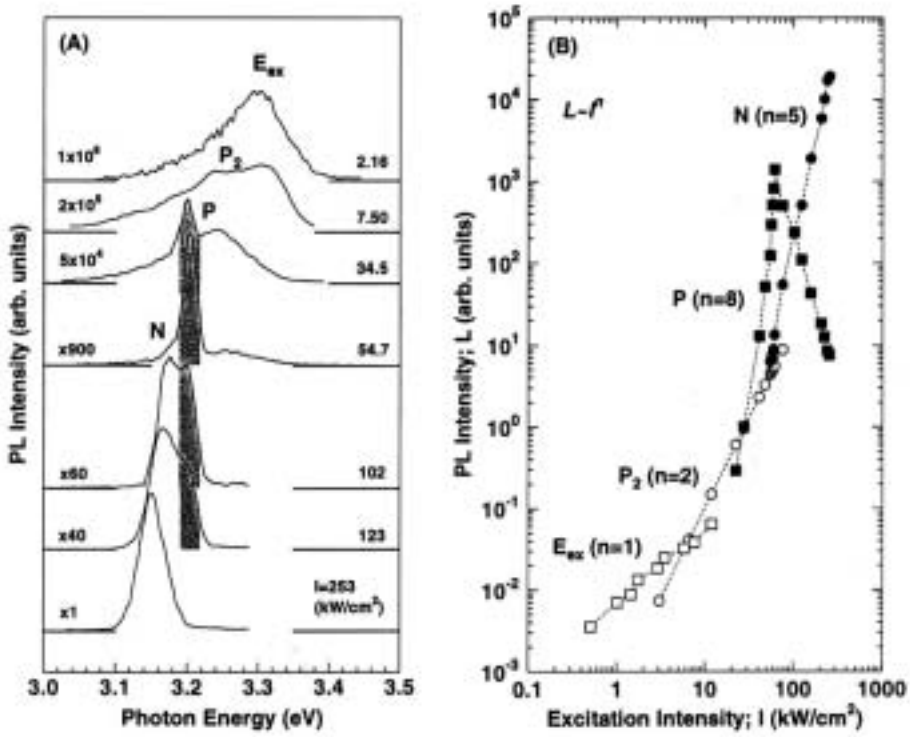

Figure 2-12. (a) PL spectra at room temperature under various excitation intensity. (b) PL intensity dependence on excitation intensity.

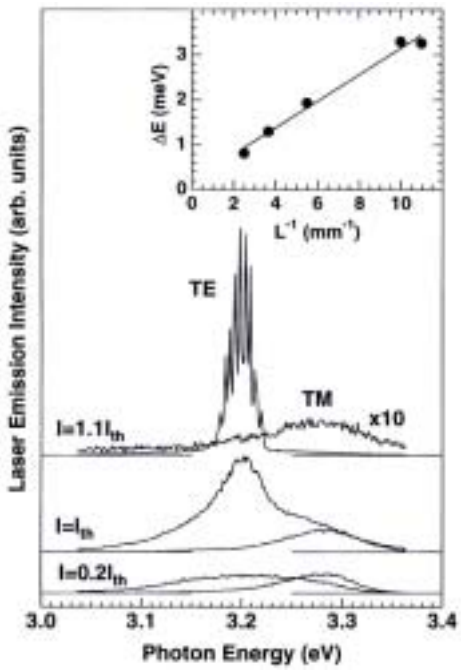

Figure 2-13. Polarized *P*-line emission spectra for the electric field perpendicular (*TE*) and (*TM*) to the *c*-axis direction (I_{th}=24 KW/cm^2)

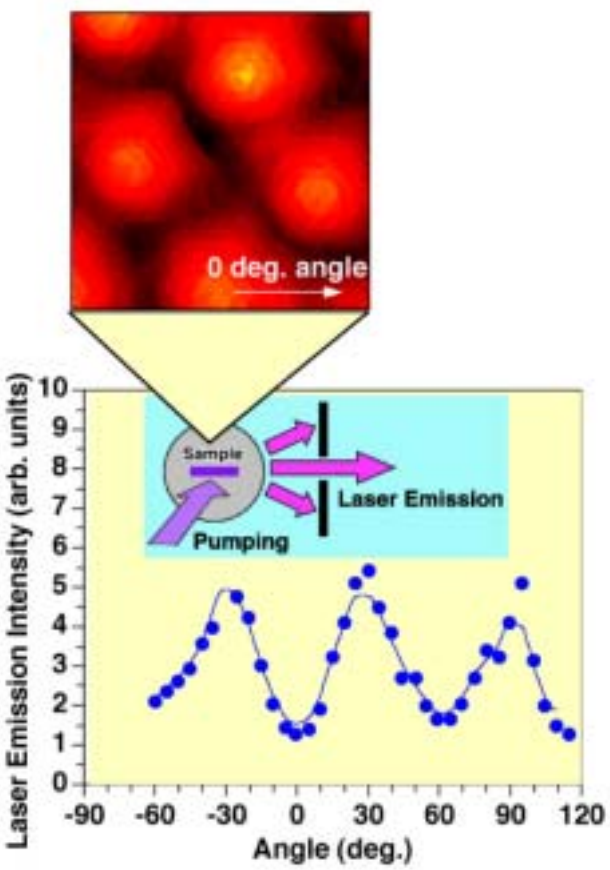

Figure 2-14. *P*-line intensity as a function of the angle between pumping stripe and in-plane crystallographic direction. The inset depicts experimental configuration.

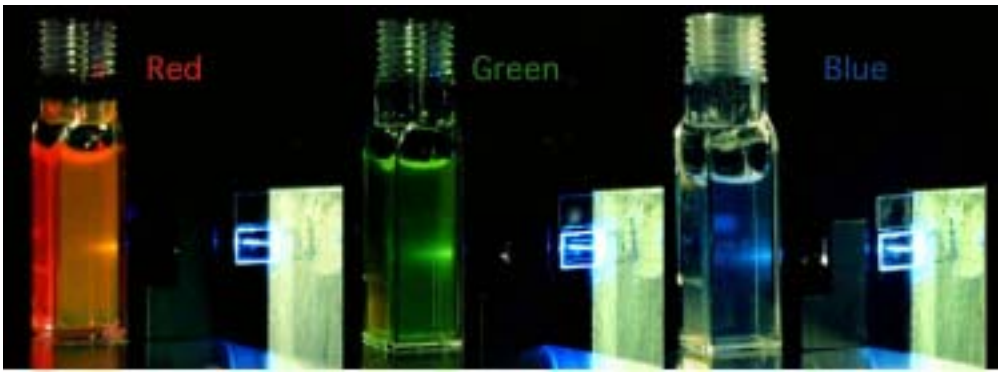

Figure 2-15. Demonstration of fluorescence emission of RGB-colors. Dye cells are excited by laser light from ZnO nanocrystalline films.

References

[1] H. Koinuma, MES Bull. **19** (9), 21 (1994).

[2] H. Koinuma, M. Kawasaki, and M. Yoshimoto, Mat. Res. Soc. Symp. Proc. **397**, 145 (1996).

[3] M. Kawasaki, A. Ohtomo, R. Tsuchiya, J. Nishino, and H. Koinuma, Mat. Res. Soc. Symp. Proc. **474**, 303 (1997).

[4] Z. K. Tang, P. Yu, G. K. L. Wong, M. Kawasaki, A. Ohtomo, H. Koinuma, and Y. Segawa, Solid State Commun. **103**, 459 (1997).

[5] Y. Segawa, A. Ohtomo, M. Kawasaki, H. Koinuma, Z. K. Tang, P. Yu, and G. K. L. Wong, Phys. Stat. Sol. **B 202**, 669 (1997).

[6] S. Nakamura, M. Senoh, S. Nagahama, N. Iwasa, T. Yamada, T. Matsushita, Y. Sugimoto, and H. Kiyoku, Appl. Phys. Lett. **69**, 4056 (1996).

[7] R. Cingolani, and K. Ploog, Adv. Phys. **40**, 535 (1991).

[8] M. Asada *et al*., IEEE J. Quantum Electron. **21**, 434 (1985).

[9] Y. Arakawa and A. Yariv, IEEE J. Quantum Electron. **22**, 1887 (1986).

[10] Y. Kayamura, Phys. Rev. **B38**, 9797 (1988).

[11] W. Wegscheider, L. N. Pfeiffer, M. M. Dignam, A. Pinczuk, K. W. West, S. L. McCall, and R. Hull, Phys. Rev. Lett. **71**, 547 (1993).

[12] C. Klingshirn, Phys Stat. Sol. **B71**, 547 (1975).

[13] M. Sano and M. Aoki, Jpn. J. Appl. Phys. **15**, 1943 (1976).

[14] Y. S. Park and D. C. Reynolds, J. Appl. Phys. **38**, 756 (1967).

[15] M. Kitamura, M. Nishioka, J. Oshinowo, and Y. Arakawa, Appl. Phys. Lett. **66**, 3663 (1995).

[16] A. Sasaki *et al.*, J. Cryst. Growth **160**, 27 (1996).

[17] V. Dmitriev, K. Irvine, A. Zubrilov, D. Tsvetkov, V. Nikolaev, M. Jackobson, D. Nelson, A. Sitnikova, Mat. Res. Soc. Symp. Proc. **395**, 295 (1996).

[18] J. Narayan, P. Tiwari, X. Chen, J. Singh, R. Chowdhary, T. Zheleva, Appl. Phys. Lett. **61**, 1290 (1992).

[19] E. J. Tersa, M. D. Graef, D. R. Clarke, A. C. Gossard, and J. S. Speck, J. Appl. Phys. **73**, 3276 (1993).

[20] P. Yu, Z. K. Tang, G. K. L. Wong, M. Kawasaki, A. Ohtomo, H. Koinuma, and Y. Segawa, *23_{rd} International Conference on the Physics of Semiconductors*, edited by M. Scheffler and R. Zimmermann (World Scientific, Singapore, 1996), p. 1453.

[21] E. Hanamura, Proc. *SPIE-Int'l. Soc. Optical Eng.* Vol. **2168**, 96 (1990).

[22] D. M. Bagnall and K. P. O'Donnell, Appl. Phys. Lett. **68**, 31 (1996).

[23] X.H. Yang, J. Hays, W. Shan, J.J. Song, E. Cantwell, J. Aldridge, Appl. Phys. Lett. **60**, 926 (1992).

[24] Z.K. Tang, P. Yu, G.K.L. Wong, M. Kawasaki, A. Ohtomo, H. Koinuma, and Y. Segawa, Nonlinear Optics **18**, 355 (1997).

[25] K. Saikuda, A. Ohtomo, H. Ohno, and M. Kawaskai, unpulished.

[26] N. Fujimura, T. Nishihara, S. Goto, J. Xu, and T. Ito, J. Cryst. Growth **54** (1981) 185.

[27] E. danielson, J. Golden, Eric W. McFarland, C. M. Reaves, W. Henry Weinberg, and Xin Di Eu, Nature **389** (1997) 944.

Chapter 3. High-Electron Mobility ZnO Films Grown on Sapphire (0001) Substrates

Abstract

ZnO films were grown on sapphire substrates at temperatures ranging from 350° C to 1000° C by laser molecular-beam epitaxy. With increasing growth temperature and/or film thickness, crystalline quality became higher, judging from x-ray rocking curve analyses. X-ray reciprocal space mapping technique was further applied to determine lateral grain size of the films, which cannot be evaluated from x-ray rocking analyses because of overlapping of mosaic spread. As the growth temperature was increased with keeping layer thickness constant at 1 μm, the lateral grain size systematically increased resulting in improved electron mobility. When the film was grown at 1000° C, the electron mobility as large as 90 cm^2/Vs was achieved. By annealing in 1 atm of oxygen at 1000° C, thin films having much larger grain size (> 5 μm^2) and higher mobility (~120 cm^2/Vs) comparable with those for bulk single crystals could be obtained.

3.1. Introduction

A wide-gap oxide semiconductor, ZnO has attracted considerable attention because it is expected to be applied for ultraviolet light emitting devices and invisible field effect transistors. Such semiconductor device applications of ZnO have become feasible by the observation of ultraviolet laser action due to an exciton-exciton collision process occurring in optically pumped ZnO nanocrystal films deposited on sapphire(0001) substrates[1]. The films are composed of closely packed hexagonal columns separated by grain boundaries[2]. We have found the grain boundaries can serve not only for potential barriers resulting in carrier confinement, but also for mirrors to form a cavity[3,4]. Although such unique functions are realized, the grain boundaries are usually thought to be a detrimental for high-performance semiconductor devices. In fact, such nanocrystalline films have much smaller Hall mobility of about 10 cm^2/Vs than that of bulk single crystals (~200 cm^2/Vs) at room temperature. This rather low mobility is presumably due to the negatively charged potential barriers located in the grain boundaries[5].

In this short chapter, a systematic study to elucidate the relationship between Hall mobility and lateral grain size is presented for the films grown at various growth temperatures and the films annealed at 1000° C. Thin films having very large in-plane grain size (~5 μm^2) and high Hall mobility (> 100 cm^2/Vs) can be made by the annealing.

3.2. Experimental

ZnO thin films were deposited on sapphire (0001) substrates by laser molecular-beam epitaxy (L-MBE) by ablating a sintered ZnO ceramic target (purity of 99.999 %) with KrF excimer laser pulses[6]. Films having thickness ranging from 20 nm to 2 μm were deposited at various growth temperature (T_g) of 350~1000° C in an oxygen pressure of 1×10^{-6} Torr with observing reflection high-energy electron diffraction (RHEED) patterns. After the characterization experiments, the films were annealed at 1000° C in 1 atm of oxygen.

The crystallinity was characterized by a powder x-ray diffraction (XRD) or a high-resolution four-circle XRD apparatuses (Philips, X'-pert MRD) equipped with a four crystal monochrometor and an analyzer crystal of which resolutions are 0.005° and 0.008°, respectively. Rocking curves for ZnO (0002) and (10-11) were measured for the films having thickness of 20~400 nm. Reciprocal space mapping (RSM) for an asymmetric ZnO(11-24) diffraction was measured to evaluate the crystallographic tilting and lateral grain size for 1 μm-thick films. The surface morphology was observed by atomic force microscopy (AFM) in air. Indium ohmic electrodes were deposited to perform Hall measurement with van der Pauw configuration.

3.3. What's Key for Improving the Crystallinity

We have grown number of ZnO films having various thickness grown under the constant condition (T_g=550° C and P_{O2}=1 × 10^{-6} Torr) to investigate optical characteristics because it was found that the film thickness significantly affected with the lasing properties[4]. FWHM values ($\Delta\omega$) of the ZnO (0002) XRD rocking curves for those films are plotted as a function of film thickness (d) in Fig. 3-1 (a). $\Delta\omega$ decreases rapidly up to d~100 nm, and then shows gradual decrease with increasing d. This dependence agrees with the fact that when film thickness is increased, nanocrystal size evaluated by AFM observations also increases, as was discussed in Chapter 2. $\Delta\omega$ depends on twofold crystallographic imperfections, that is, tilting mosaicness and lateral grain structure, as be discussed later in detail. We suppose that larger $\Delta\omega$ for thinner films is attributed to much smaller lateral grain size as seen in AFM images. In order to know optimal growth condition, 200 nm-thick films were grown at various temperatures ranging from 550 to 800° C. Both of FWHM ($\Delta\phi$) of the ZnO (10-11) XRD rocking curves and $\Delta\omega$ systematically decreases with increasing growth temperature as shown in Fig. 3-1 (b). Thus, higher growth temperature was better to improve crystalline quality, therefore thick films (~1 μm) were further grown at temperatures up to 1000° C in following studies.

3.4. Lateral Grain Size and Electron Mobility in ZnO Epitaxial Films

3.4.1. An effect of thermal annealing: surface morphology

About 1 μm-thick c-axis oriented films were obtained by 2 hours-deposition with a repetition of 10 Hz and a fluence of 0.6 J/cm^2 of KrF excimer laser pulses. The RHEED patterns for the films grown at T_g below 650° C showed sharp streaks. Above 650° C, V-shaped weak diffraction spots appeared along with the streaks, indicating that the surface became slightly rough due to the appearance of vicinal facets. From AFM observations, T_g dependence of the surface morphology was revealed as follows, (1) T_g=350~450° C; round-shaped nanocrystals with a lateral size of about 100 nm were seen, (2) T_g= 500~650° C; hexagonally-shaped nanocrystals with a size of 300 nm were observed as shown in Fig. 3-2 (a) (These morphologies are similar to those of the films reported previously[2]), (3) T_g >650° C; hexagonally faceted pits with depth and lateral size of about 50 nm and 300 nm, respectively, appeared on atomically flat surface. After these films were annealed at 1000° C, all films showed very smooth surface as seen in Fig. 3-2 (b) regardless T_g. The surface is composed of atomically flat terraces and 0.26 nm-high steps (a charge neutral unit of ZnO), as seen in the top panel profile. A curious fact in this image is that there can be seen ramps of which slope is about 0.1° as clearly depicted in the cross-sectional profile given in the right side of the AFM image. The slope angle agrees with the crystallographic tilting angle, deduced from x-ray RSM analysis to be discussed later. Despite the ramps are merged to form up and down structure,

the atomically flat terraces and steps are seen continuous. Therefore, it is natural to think that the (0001) planes are bent to form the slopes rather than assume the presence of distinct low angle grain boundaries. For further elucidate the structure, transmission electron microscope study is needed. As can be seen in lower magnification image of Fig. 3-2 (c), the bending structure randomly distributes with the spacing between peak and valley of about 5 μm, which is again agreed with the grain size deduced from XRD.

3.4.2. X-ray reciprocal space mapping

X-ray RSM technique and an analysis method have been improved to evaluate the lateral grain size of the films having large lattice mismatch[7]. Fig. 3-3 schematically indicates the principle of the RSM measurement to explain briefly the difference between a conventional rocking curve (ω-scan) and RSM analyses. The shape of x-ray diffraction pattern is responsible for crystallographic imperfections such as mosaicness, crystal size, and residual strain. In reciprocal space, the direction of the spread due to out-of-plane crystallographic tilting ($\Delta\theta$) is parallel to ω-axis, while a spread ($\Delta\xi^{-1}$) due to a finite lateral grain size ($\Delta\xi$) appears parallel to the horizontal axis (Q_x). The $\Delta\theta$ component arises from both of mosaicness and substrate bending. The substrates used in this study show no bending, therefore $\Delta\theta$ can be considered to represent only the former component. These two components can not be independently measured by a conventional rocking curve for a symmetric lattice plane due to the overlapping ($\Delta\theta$ // $\Delta\xi^{-1}$). While, their directions are not parallel to each other for an asymmetric plane, so that each component can be analytically evaluated to yield $\Delta\xi^{-1}$ value.

Figure. 3-4 (a) and (b) show RSMs of the ZnO (10-14) for the same films shown in Fig. 3-2 (a) and (b), respectively. From analyzing these contour mappings, we obtain 0.11° and 0.15° as $\Delta\theta$, and 1.3×10^{-3} and 2.8×10^{-5} as $\Delta\xi^{-1}$ for the as-grown and the annealed samples, respectively. $\Delta\xi$ and $\Delta\theta$ become much larger by annealing. As seen in the insets of the figures, FWHM of the symmetric ZnO (0002) ω-scan decreases after annealing, and this reduction is due to reduction of grain size during annealing. The value of $\Delta\theta$ for the annealed film shows good agreement with the bending angle (0.18 (0.09 × 2)°) shown in Fig. 3-2 (b).

3.4.3. A role in the structural and electronic properties

Crystallographic parameters and electronic properties for the films grown at various T_g ranging from 350° C to 1000° C are plotted as a function of T_g in Fig. 3-5. In case of the as-grown films, the FWHM values of ω-scan ($\Delta\omega$) and $\Delta\theta$ decrease up to 800° C and then increase again at 1000° C, while $\Delta\xi^{-1}$ monotonously decreases with increasing T_g as shown in Fig. 3-5 (a)~(c). The annealed films have larger values of $\Delta\omega$ and $\Delta\theta$ except for the film grown at 350° C and smaller $\Delta\xi^{-1}$ values. The latter result can be

much clearly seen in Fig. 3-5 (d) ($\Delta\xi$ vs. T_g plot). The original T_g dependence of $\Delta\xi$ for the as-grown films is kept even after annealing, indicating that the grain growth during annealing is kinetically limited by atom migration. This is also supported by the fact that $\Delta\xi$ value of the film annealed for 7 h (×) is larger than that of the film annealed for 2 h. Since the $\Delta\xi$ value directly corresponds to the average of the lateral grain size, it is concluded that the lateral grain size can be increased more than 5 μm^2, which corresponds equipment resolution, by increasing T_g and high temperature annealing. In Fig. 3-5 (e), Hall mobility of electrons (μ) measured at room temperature is plotted for the same samples. As T_g increases, electron mobility systematically increases for the as-grown films. Obviously, electron mobility of the as-grown films has good correlation with the lateral grain size. This can be explained if the strong carrier scattering at the grain boundaries is taken into account. After annealing, electron mobility becomes larger. Maximum electron mobility achieved in this study is as large as 120 cm^2/Vs, which is close to that (160 cm^2/Vs) of a bulk crystal grown by hydrothermal method (Litton Airtron Co., Ltd). However, the mobility shows almost constant value of about 100 cm^2/Vs, although the lateral grain size varies by one order of magnitude with the growth temperatures. This means that another factor plays an important role to determine electron mobility.

Here, we consider that the electron scattering takes place due to the double Schottky potential barriers located in the grain boundaries. When there is a deep trap level at the grain boundaries, electrons are trapped at the grain boundaries to induce carrier depletion around grain boundaries and to build double Schottky barrier[5]. The annealed films have larger carrier concentrations (10^{17}~10^{18} cm^{-3}) than those of the as-grown films (10^{16}~10^{17} cm^{-3}) as shown in Fig. 3-5 (f). It is likely that high carrier concentration makes the depletion layer thin by Coulomb screening effect to enhance effectively the electron mobility.

Finally, lattice constants calculated from peak maximum positions in RSMs are plotted in Fig. 3-5 (g). As T_g increases, the *a*- and c- axis lattice constants gradually deviate from those of bulk crystal (a_0=3.250 Å and c_0=5.204 Å). This is presumably due to compressive strain parallel to the (0001) plane caused by a negative thermal expansion mismatch (1.2×10^{-6} K^{-1}) between ZnO and sapphire. Since lattice constants are recovered to the almost original bulk values after annealing, the residual strain is released during grain growth.

Electron mobility is plotted as a function of the lateral grain size ($\Delta\xi$) in Fig. 3-6 for all of the films discussed above. As can be much clearly seen, Hall mobility increases with increasing $\Delta\xi$ for the as-grown films, indicating that scattering loss during carrier transport decreases with decreasing grain boundary density, resulting in larger electron mobility. After annealing, electron mobility becomes larger. Maximum Hall mobility is achieved to be as high as 120 cm^2/Vs, which is close to that (160 cm^2/Vs) of a bulk crystal grown by hydrothermal method (Litton Airtron Co., Ltd) denoted by ▲ in Fig. 3-6. Note

that a square root value of etch pit density (~10^4 cm^2) is used for $\Delta\xi$ of this crystal because the $\Delta\xi^1$ value of bulk crystal is too small to evaluate by x-ray reciprocal space analysis.

The electron mobility measured in this study is still smaller than the highest reported value for a bulk single crystal (230 cm^2/Vs)[8]. Further improvement should be expected if much larger grain size, smaller mosaicness, and lower impurity concentration could be achieved. Actually, when we used a lattice-matched substrates to grow single-crystalline films, high mobility (~100 cm^2/Vs) and low residual carrier concentration (~10^{15} cm^{-3}) could be simultaneously achieved even for the film grown at 350° C.[9] (See chapter 6)

3.5. Conclusions

ZnO thin films having various lateral grain sizes (0.02~5 μm^2) were fabricated by varying growth temperatures as well as sample annealing at 1000° C. Room temperature electron mobility of the as-grown films is found to increase with increasing the lateral grain size evaluated by x-ray reciprocal space analyses. The lateral grain size and electron mobility becomes much larger by the annealing process. The electron mobility as large as 100 cm^2/Vs could be reproducibly obtained by the annealing.

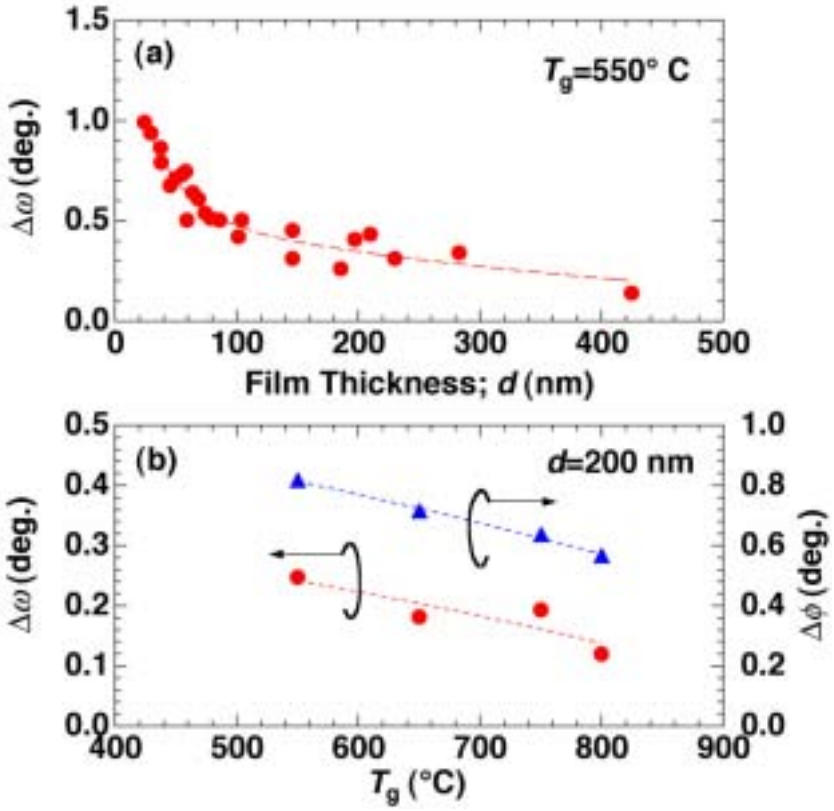

Figure. 3-1. (a) Film thickness (d) dependence of FWHM ($\Delta\omega$) of x-ray rocking curve peak for ZnO (0002). (b) $\Delta\omega$ and $\Delta\phi$ (FWHM of x-ray rocking curve peak for ZnO (10-11)) as a function of growth temperature (T_g).

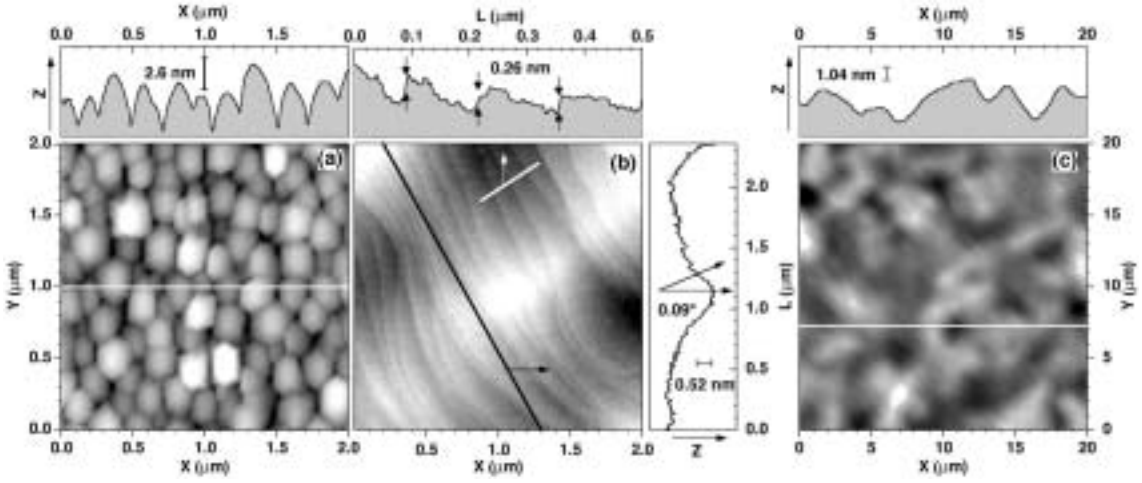

Figure. 3-2. (a) AFM image (2×2 μm^2) of a films grown at 550° C. (b) and (c) AFM images of the same film after annealing at 1000° C with scales of 2×2 μm^2 and 20×20 μm^2, respectively. The cross-sections are shown on the top of the each image. The makers in the profiles show z-axes scales. As seen in (b) and the right-side profile, terrace plane is slightly curved, indicating that the (0001) plane is bending.

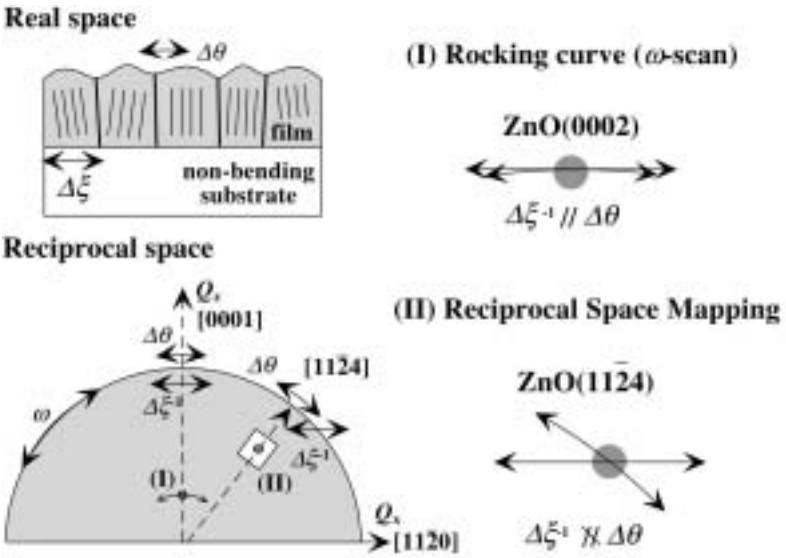

Figure. 6-3. Schematic illustrations of the crystalline imperfections in a real space (left-top) and a reciprocal space (left-bottom), and the directions of spreads due to the crystallographic tilting ($\Delta\theta$) and finite lateral grain size ($\Delta\xi^{-1}$) for the (0002) and (11-24) diffraction patterns are shown.

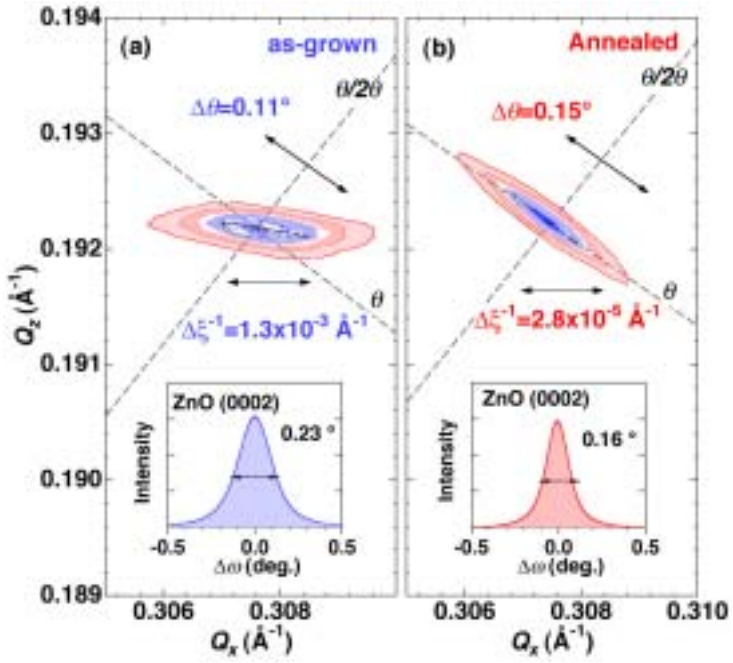

Figure. 6-4. (a) reciprocal space mapping (RSM) of ZnO(10-14) for a film grown at 550° C. (b) RSM of the same film after annealing at 1000° C for 7 h. The broken lines show the directions for Bragg diffraction ($\omega/2\theta$) and rocking curve (ω). Insets show rocking curves of ZnO (0002) for each films.

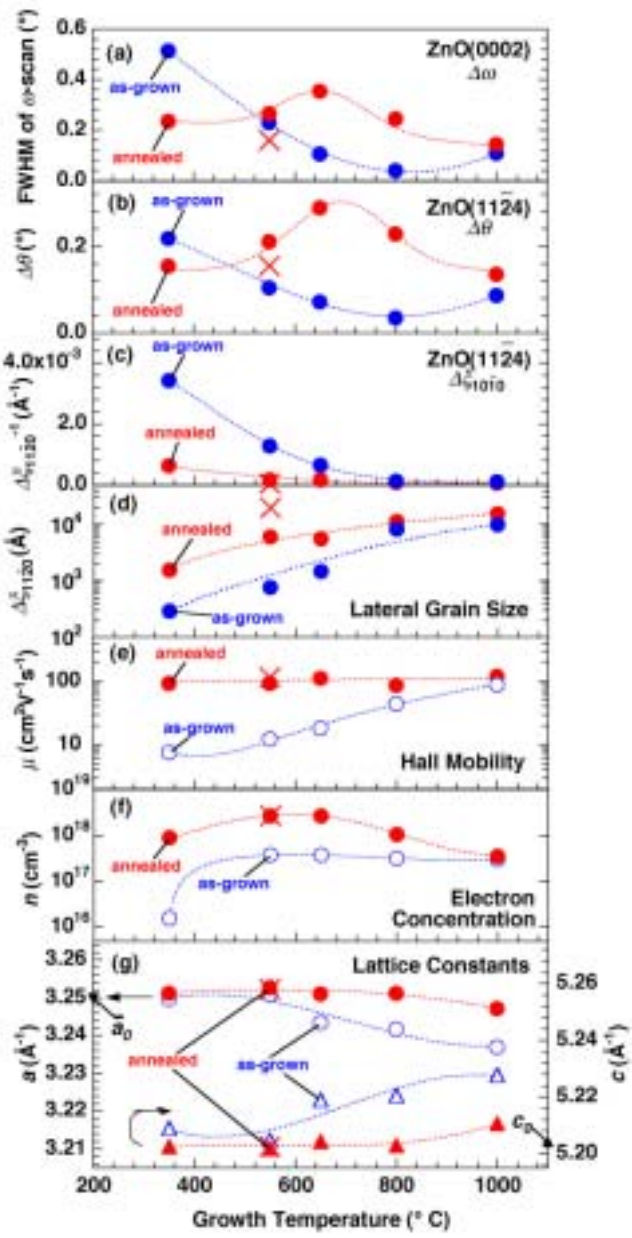

Figure. 3-5. Growth temperature dependence of (a) FWHM of ZnO (0002) ω–scan, (b) crystallographic tilting ($\Delta\theta$), (c) lateral coherence length ($\Delta\xi^{-1}$) evaluated from RSMs for ZnO (11-24), (d) lateral grain size ($\Delta\xi$), (e) electron mobility (μ) and (f) carrier concentration (n), measured at room temperature, (g) lattice constants in the direction of a- and c-axes for the as-grown films and annealed films having thickness of about 1 μm. a_0 and c_0 is the lattice constants for the bulk single crystal. Open symbols are for the as-grown films and closed symbols are for the same films annealed at 1000° C for 2 h. One of the films denoted by × was annealed at 1000° C for 7 h.

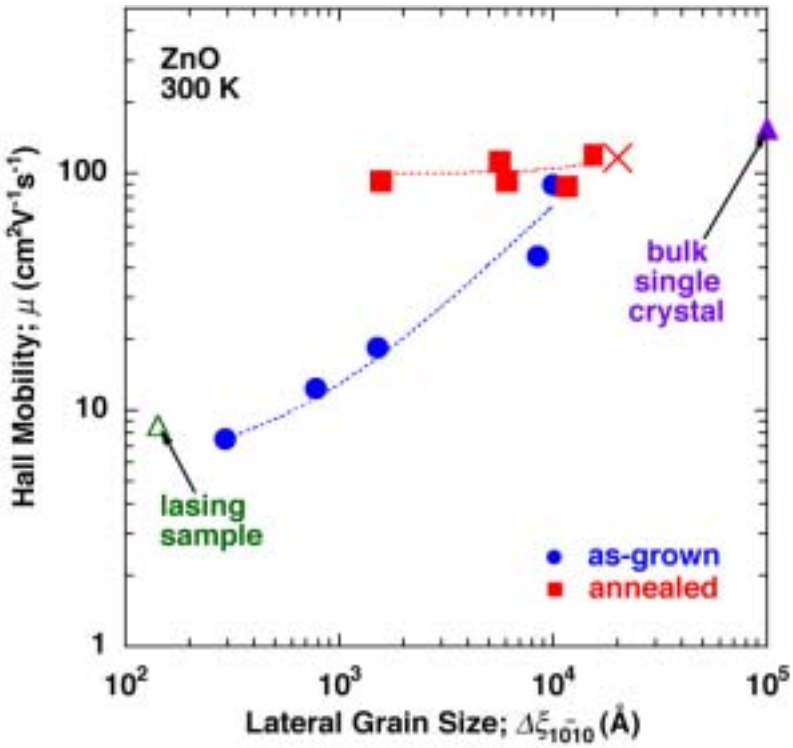

Figure. 3-6. Lateral grain size ($\Delta\xi$) dependence of Hall mobility (μ) for as-grown (◯) and the annealed films (●). The maximum mobility is as large as 120 cm^2/Vs. The values of a commercial bulk crystal and a nanocrystalline film showing laser action are plotted by ▲ and △, respectively.

References

[1] M. Kawasaki, A. Ohtomo, I. Ohkubo, H, Koinuma, Z.K. Tang, P. Yu, G.K.L. Wong, B.P. Zhang, Y. Segawa, Mat. Sci. Eng. **B56**, 239 (1998).

[2] A. Ohtomo, M. Kawasaki, Y. Sakurai, Y. Yoshida, H. Koinuma, P. Yu, Z.K. Tang, G.K.L. Wong, Y. Segawa, Mat. Sci. Engi. **B54**, 24 (1998).

[3] Z.K. Tang, G.K.L. Wong, P. Yu, M. Kawasaki, A. Ohtomo, H. Koinuma and Y. Segawa, Appl. Phys. Lett. **72**, 3270 (1998).

[4] P. Yu, Z.K. Tang, G.K.L. Wong, M. Kawasaki, A. Ohtomo, H. Koinuma, Y. Segawa, J. Cryst. Growth **184/185**, 601 (1998).

[5] G. Blatter, F. Greuter, Phys. Rev. **B33** (1985) 3952.

[6] H. Koinuma, M. Kawasaki, and M. Yoshimoto, Mat. Res. Soc. Symp. Proc. **474**, 303 (1997).

[7] P. F. Fewster, *X-ray and Neutron Dynamical Diffraction: Theory and Application*s, eds. P. F. Fewster et al. (Plenum Press, New York, 1996) 269.

[8] D. C. Look, J. W. Hemsky, J. R. Sizelove, Phys. Rev. Lett. **82** (1999) 2552.

[9] A. Ohtomo, K. Tamura, K. Saikusa, K. Takahashi, T. Makino, Y. Segawa, H. Koinuma, M. Kawasaki, Appl. Phys. Lett. **75** (1999) 2635.

Chapter 4. Band Gap Engineering of ZnO: $Mg_xZn_{1-x}O$ and $Zn_{1-x}Cd_xO$ Ternary Alloy Films

Abstract

We propose novel II-VI semiconductor alloys, $Mg_xZn_{1-x}O$ and $Zn_{1-y}Cd_yO$, for tuning emission energy and fabricating heteroepitaxial ultraviolet light emitting devices based on ZnO. The single-phase alloy films with *c*-axis orientation and alloying compositions up to x=0.33 for $Mg_xZn_{1-x}O$ and y=0.07 for $Zn_{1-y}Cd_yO$ were epitaxially grown by pulsed laser deposition on sapphire (0001) substrates using mixed ceramic targets. Band gap of the alloy films systematically varies from 3.0 eV (y=0.07) to 4.0 eV x=0.33 at room temperature. PL peak position at 4.2 K could be tuned from 3.19 eV for y=0.07 to 3.87 eV for x=0.33. Impurity phase (rock-salt phase) segregated at x>0.33 for the $Mg_xZn_{1-x}O$ alloy, whereas, no impurity phase was detected in the $Zn_{1-y}Cd_yO$ alloy up to 0.07. *a*-axis lattice constants of the alloy films increased resulting in in-plane lattice mismatches at heterointerfaces with pure ZnO to be +1.1x (%) for $Mg_xZn_{1-x}O$, and +5.1y (%) for $Zn_{1-y}Cd_yO$, respectively. We have also examined the thermal stability of wurtzite-phase $Mg_xZn_{1-x}O$ alloy films and ZnO/$Mg_xZn_{1-x}O$ bilayer films with x exceeding the reported solubility limit of 0.04. When a $Mg_{0.22}Zn_{0.78}O$ film was annealed, the segregation of MgO started at 850° C and the band gap was reduced to the value of that for a x=0.15 film after annealing at 1000° C. $Mg_{0.15}Zn_{0.85}O$ films showed no change of the band gap even after annealing at 1000° C. Therefore, we conclude that the thermodynamic solubility limit of MgO in $Mg_xZn_{1-x}O$ epitaxial film is about x=0.15. The thermal diffusion of Mg across the $Mg_xZn_{1-x}O$/ZnO interface was observed only after annealing above 700° C. Unlike other II-VI semiconductors, ZnO-based alloy films and heterointerfaces are stable enough for the fabrication of high-crystallinity heterostructures.

4.1. Widegap Semiconductor Alloy: $Mg_xZn_{1-x}O$

4.1.1 Introduction

A heterojuction is one of the key structures for constructing various electronic and optical devices using compound semiconductors. Modulation of the band gap with keeping the lattice constants similar to each other is essential for this purpose. For instance, a double heterostructure (DH) composed of thin well layer sandwiched between two barrier layers has been utilized in laser diodes to facilitate radiative recombination by carrier confinement.[1] We recently reported that stimulated emission due to excitonic recombination could be observed at room temperature by optically pumped ZnO nanocrystalline thin films epitaxially grown on sapphire substrates.[2] Laser action with a very low threshold intensity (24 kW/cm^2) took place using naturally occurring grain boundaries as cavity mirrors.[3] For fabricating a DH laser diode using a ZnO active layer, two critical materials challenges are *p*-type doping[4] and bad gap engineering in alloy semiconductors. We concentrate on the latter in this chapter.

4.1.2. Experimental

In case of ZnSe-based lasers, the $Zn_{1-x}Mg_xS_ySe_{1-y}$ alloy with x up to 0.4 has been used for barrier and cladding lasers.[5] Wide range solubility of Mg in the zinc blend structure was expected because the tetrahedral ionic radius of Mg^{2+} (0.57 Å) is similar to that of Zn^{2+} (0.60).[6] Here, we propose a novel II-VI oxide semiconductor alloy system, $Mg_xZn_{1-x}O$, which has excellent optical properties and similar lattice constants to those of ZnO.

$Mg_xZn_{1-x}O$ thin films were grown on sapphire (0001) substrates, polished on both sides, by pulsed laser deposition in an ultrahigh vacuum chamber.[7] Predetermined amounts of ZnO (5N) and MgO (4N) powders were mixed, calcined, and sintered to form targets with Mg content ranging from x=0 to x=0.18. The x-ray diffraction (XRD) spectra of the targets showed no detectable MgO peaks for x<0.10, whereas clear MgO peaks was observed for x>0.13. The targets were placed at a distance of 4 cm from the substrate and ablated by KrF excimer laser pulses (248 nm, 10 Hz, 30 ns) with a fluence of 1 J/cm^2. The films (~300 nm-thick) were deposited at a temperature ranging 350-800 °C in 5×10^{-5} Torr of pure oxygen (6N). The results will be discussed with the films grown at 600° C as far as any comment is not given. Mg content in the $Mg_xZn_{1-x}O$ films was determined by inductively coupled plasma (ICP) optical emission spectroscopy by dissolving the films in HNO_3 solution. The surface morphology of the films was examined by means of contact-mode atomic force microscopy (AFM). The crystal structure of the films was analyzed by θ-2θ XRD and four-circle XRD (Philips, *X'* Pert-MRD) with a resolution of 0.005°. Out-of-plane and in-plane mosaicness were evaluated by setting the Bragg diffraction angle to the ZnO

(0002) and (10-11) reflections, respectively, where -1 stands for negative value of Miller index. Optical properties were characterized by absorption and photoluminescence (PL) spectroscopies. A continuous He–Cd laser (325 nm) and a pulsed XeCl excimer laser (308 nm, 10 Hz) were used for the PL measurements.

4.1.3. Film composition and structural properties

Deposition rate of the films was 1.5×10^{-2} nm/pulse regardless Mg content in the targets. Figure 4-1 shows growth temperature (T_g) dependence of the Mg content in the films as a function of that in the targets. At T_g=350° C, the Mg content in the films was same as that in the targets. At T_g=500° C, the Mg content in the films was larger than in the targets by a factor of 2 up to the Mg content in the target of 0.10. Above 0.10, film composition is a constant at x=0.20 regardless target compositions. At much higher growth temperature (600~650° C), the Mg content in the films monotonously increases with increasing that in the targets showing an enrichment factor of about 2.5. Mg condensation can be attributed to the fact that the vapor pressures of ZnO and Zn are much larger than those of MgO and Mg at growth temperatures.[8] Zn-related species can easily desorb from the growing surface and lead to the condensation of Mg-related species on the surface.

Single-phase alloy films having wurtzite structure and *c*-axis orientation could be prepared with x up to 0.25, as verified by XRD analyses. When Mg content was larger than 0.36, small peaks due to an impurity phase [(111) oriented MgO] were observed. At x=0.33, very weak signal could be detected at 2θ~78° where MgO(222) peak should appear. However the intensity was much smaller than ZnO(0002) peak by factor of 10^{-4}, therefore, the solubility limit of MgO in ZnO for the films prepared in this study should be as large as 33 mol %. The thermodynamic solubility limit of MgO in ZnO has been reported to be less than 4 mol %, according to the phase diagram of the ZnO–MgO binary system.[9] The $Mg_xZn_{1-x}O$ films reported here can therefore be considered as metastable phases. Pulsed laser deposition is a suitable growth method for fabricating such metastable phase films because of the high peak energy of the laser light. Target material is instantaneously evaporated during the laser ablation, providing gas phase precursors with a fairly high energy (several tens of eV).[10] The precursors arrive at the substrate surface and are rapidly cooled, crystallizing at the substrate temperature. The nonequilibrium nature of this crystal growth enabled us to fabricate solid solution films well above the thermodynamic solubility limit. Lattice constants measured by the four-circle XRD are plotted as a function of the Mg content in Fig. 4-2. The *a*-axis length gradually increases, while the *c*-axis length decreases with increasing Mg content. Consequently, the cell volume [$\sqrt{3}/2a^2c$] hardly changed, agreeing with the fact that ionic radii of Zn^{2+} and Mg^{2+} have similar values. Since the lattice constants still showed gradual change up to x=0.33, where impurity MgO phase started to appear in XRD, we can conclude that the solubility limit under these

conditions was between x=0.33 and 0.36. In-plane (0002) ω-scans and an out-of-plane (10-11) ϕ-scans are shown for the $Mg_{0.32}Zn_{0.68}O$ films (T_g=750° C) and pure ZnO film (T_g=800° C) in Fig. 4-3. Full width at half maximum (FWHM) of (0002) and (10-11) rocking curves were 0.13° and 0.55°, respectively. These values are comparable to those for the pure ZnO films (0.12° and 0.56°, respectively). The in-plane crystal orientation was determined to be $Mg_xZn_{1-x}O(10\text{-}10)//\alpha\text{-}Al_2O_3(11\text{-}20)$, which is the same as that of $ZnO/\alpha\text{-}Al_2O_3$ and $GaN/\ \alpha\text{-}Al_2O_3$.[11]

4.1.4. Optical properties

Here we discuss optical characteristics of the $Mg_xZn_{1-x}O$ alloy films such as band gap and luminescence energy measured at 4.2 K and at 295 K. Figure 4-4 shows absorption spectra measured at room temperature by conventional ultraviolet-visible spectrometer. As can be clearly seen, the absorption edge shifted as a function of x when x<0.36, saturating at higher Mg content. This result is in good agreement with the appearance of the MgO impurity phase detected by XRD. For evaluating the band gap (E_g) we employed an α^2 vs. E_g plot for the spectra to fit the data assuming an $\alpha^2 \propto (h\nu - E_g)$ relationship, where α is the absorption coefficient and $h\nu$ is the photon energy. The band gap is shown as a function of x in the inset of Fig. 4-4. E_g linearly increased up to 4.15 eV for $0<x<0.36$, indicating that the $Mg_xZn_{1-x}O$ alloy is a suitable material for potential barrier layers in ZnO based devices having the band gap offset as large as 0.85 eV.

Figure 4-5 shows PL and absorption spectra taken at 4.2 K of samples with x<0.33, where single-phase films could be grown. With increasing x, the luminescence peak shifted to higher energy. The luminescence peak of pure ZnO film (x=0) had slightly lower energy than those of *A* and *B* exciton peaks clearly visible in the absorption spectrum.[2] This emission can be attributed to a bound exciton emission line (*I*), *i.e.*, the recombination of excitons trapped in shallow impurity levels. The alloy film with x =0.03 showed a luminescence peak at an energy close to the absorption edge. This is probably due to the screening effect, where excitons are no longer trapped at intrinsic impurities because the Mg ions become the major impurity. When x >0.07, the luminescence peak showed Stokes shift to the lower energy side of the absorption edge. The broadening and Stokes shift of the luminescence peak are frequently observed in alloy semiconductors,[12] where carriers feel different potentials depending on the local concentration and/or arrangement of the substituting elements. This effect is larger in ZnO than in III–V semiconductor, because the Bohr radius of excitons in ZnO is as small as 18 Å and the excitons are therefore more sensitive to local inhomogeneity. On the lower energy side of the emission peaks for x<0.14 samples, small peaks can be seen at a constant interval (about 72 meV) as denoted by filled triangles in Fig. 4-5. These peaks can be attributed to the LO-phonon replicas,[13] indicating high quality of the films in terms of crystallinity and optical properties. Thus, $Mg_xZn_{1-x}O$ films can be considered not

only as barrier layers for the ZnO active layer, but also as an ultraviolet light emitting material, the luminescence energy of which can be tuned from 3.36 (x=0) to 3.87 eV (x=0.33) by adjusting the Mg content (x).

Strong luminescence peaks but broad peak width were observed from all the samples even at room temperature. Figure 4-6 (a) shows room temperature PL and absorption spectra taken by using XeCl excimer laser excitation of samples with $0<x<0.45$. Much broader spectrum shape and larger Stokes shift is seen for the films having $x \geq 0.36$, where the films contain impurity phase. Recently, Sharma *et. al*. reported improvement of the optical characteristics of the $Mg_xZn_{1-x}O$ films grown by PLD and annealed at a high temperature (~750° C).[14] They showed sharper PL line width as can be seen in Fig. 4-6 (b). Since crystallinity of our films is higher than that of their films, the difference of spectral widths can be attributed to different Mg content fluctuations. Post-annealing process at an optimum temperature would be useful to achieve homogeneous composition. Optical transition energies for both PL and absorption, and PL peak width are summarized in Fig. 4-7. At 4.2 K, PL peaks starts to show considerable broadening and Stokes shifts at x=0.19 as shown in Fig. 4-7 (a). This agrees with the fact that thermodynamic solubility limit is x=0.15, as was determined experimentally and discussed in the next section. Therefore, the film having x>0.15 can be considered to have microscopic fluctuation of Mg content. Alloy broadening of exciton line width in II-VI semiconductors can be described by using theoretical formula.[15] The calculated values are plotted against Mg content in the inset of Fig. 4-7. Significant deviation between experimental and theoretical values starts at x=0.15, which again agrees with above speculation.

For fabricating ZnO/$Mg_xZn_{1-x}O$ quantum well structures and superlattices, it is important to regulate the film surface and interface flatness. The alloy films deposited directly on sapphire had relatively rough surface compared to pure ZnO films. The root mean square (rms) roughness of the x=0.33 film was 10 nm. The film with x>0.36 showed many particles on the surface probably due to MgO precipitates. However, by inserting a buffer ZnO film (100 nm), the surface of the alloy films (x<0.33) became as smooth as that of pure ZnO films and the rms value for roughness of the 300 nm-thick film was as small as 1 nm. This surface smoothness is acceptable for fabricating superlattices and quantum well structures.

4.1.5. Conclusions

In summary of this section, we have fabricated $Mg_xZn_{1-x}O$ films by PLD. The optical band gap and PL peak can be tuned to the larger energy side maintaining high crystallinity without any significant change of the lattice constant. Sharp PL line is observed from the films with x<0.15. $Mg_xZn_{1-x}O$ film should be a suitable material for fabricating ZnO based heterostructures.

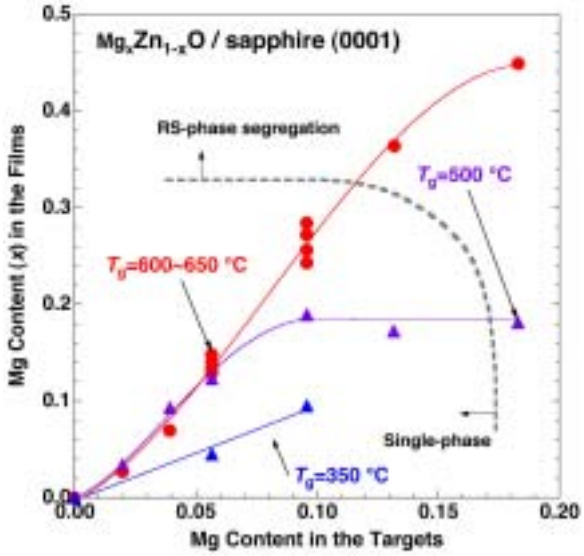

Figure 4-1. Growth temperature dependence of Mg content in the $Mg_xZn_{1-x}O$ epitaxial films as a function of Mg content in the targets. The dotted line indicates boundary between single-phase films and mixed-phase film.

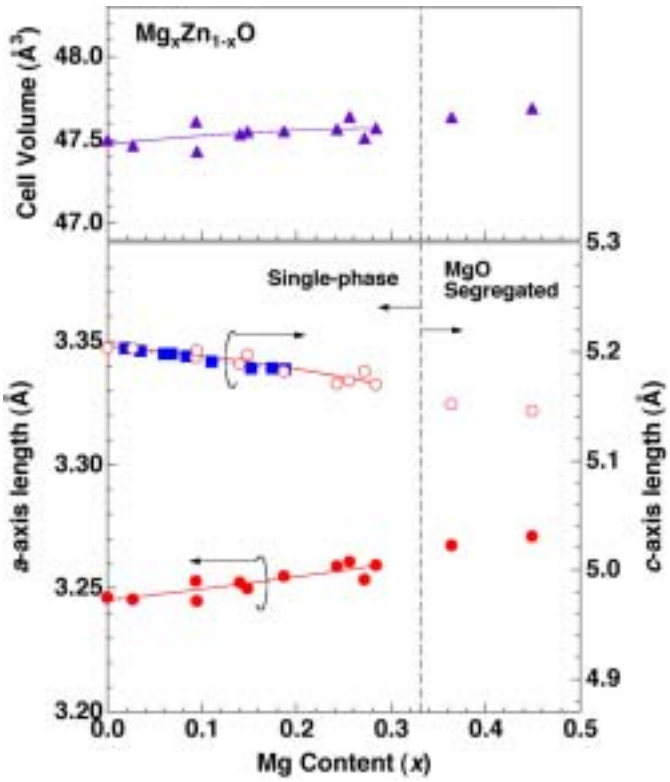

Figure 4-2. Mg content dependence of the *a*- and *c*-axis lattice parameters and the cell volume of $Mg_xZn_{1-x}O$ films. Segregation of the MgO impurity phase was observed for x>0.33 of Mg content. The values indicated by ■ are taken from Y. Matsumoto *et. al.*, Jpn. J. Appl. Phys. **38**, L603 (1999).

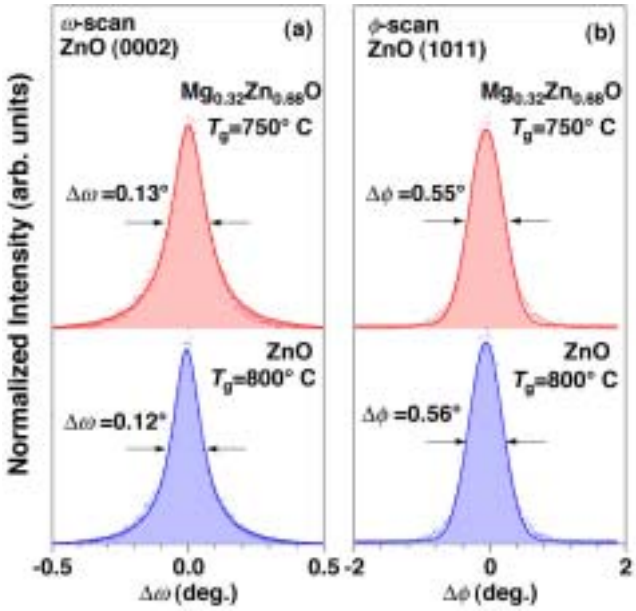

Figure 4-3. X-ray diffraction rocking curves showing (a) (0002) ω- and (b) (10-11) ϕ–scans of a $Mg_{0.32}Zn_{0.68}O$ film grown at 750° C, and a ZnO film grown at 800° C. The FWHM widths of the peaks are comparable to the pure ZnO films.

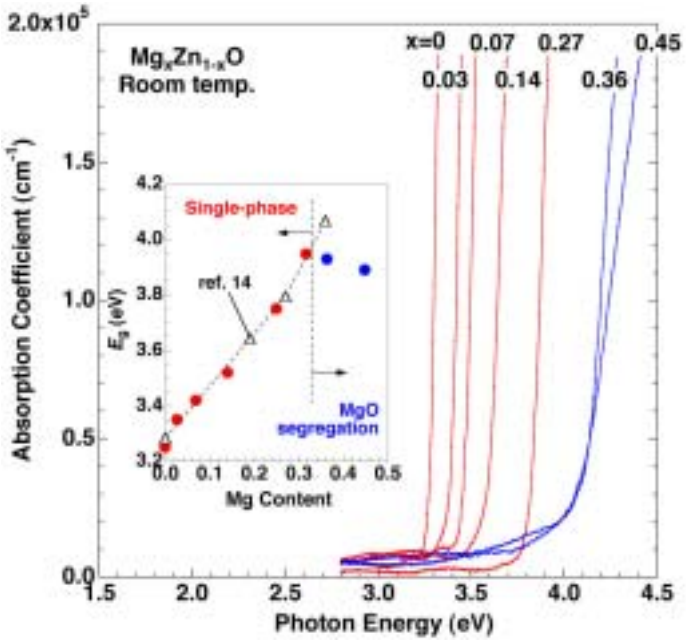

Figure 4-4. Absorption spectra of $Mg_xZn_{1-x}O$ films measured at room temperature. The inset shows the band gap (E_g) determined from the spectra assuming an $\alpha^2 \propto (h\nu - E_g)$ dependence, where α and $h\nu$ are the absorption coefficient and the photon energy, respectively. Open triangles in the inset show the E_g values reported in Ref. 14.

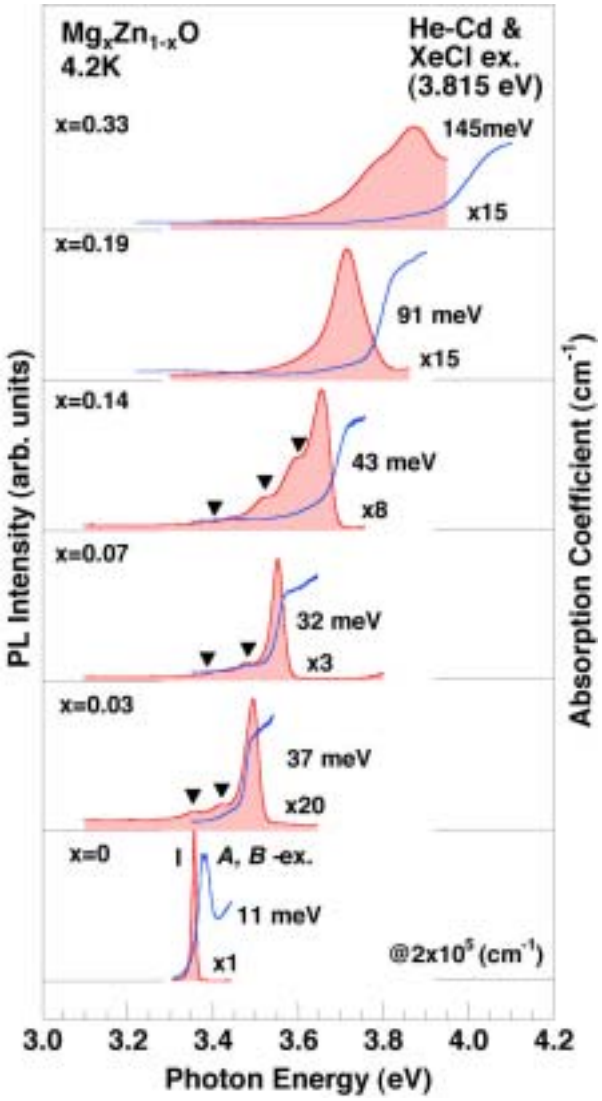

Figure 4-5. PL (solid lines) and absorption spectra (dotted lines) of $Mg_xZn_{1-x}O$ films ($0<x<0.33$). The spectra were taken at 4.2 K. For the films with $0<x<0.14$, He–Cd laser excitation (3.81 eV) was employed. For the films with $0.19<x<0.33$, XeCl laser pulses (4.03 eV) were used. Solid triangles corresponded to the peaks due to phonon replicas. FWHM values of the PL peaks and magnifications are given at the right side of the spectra.

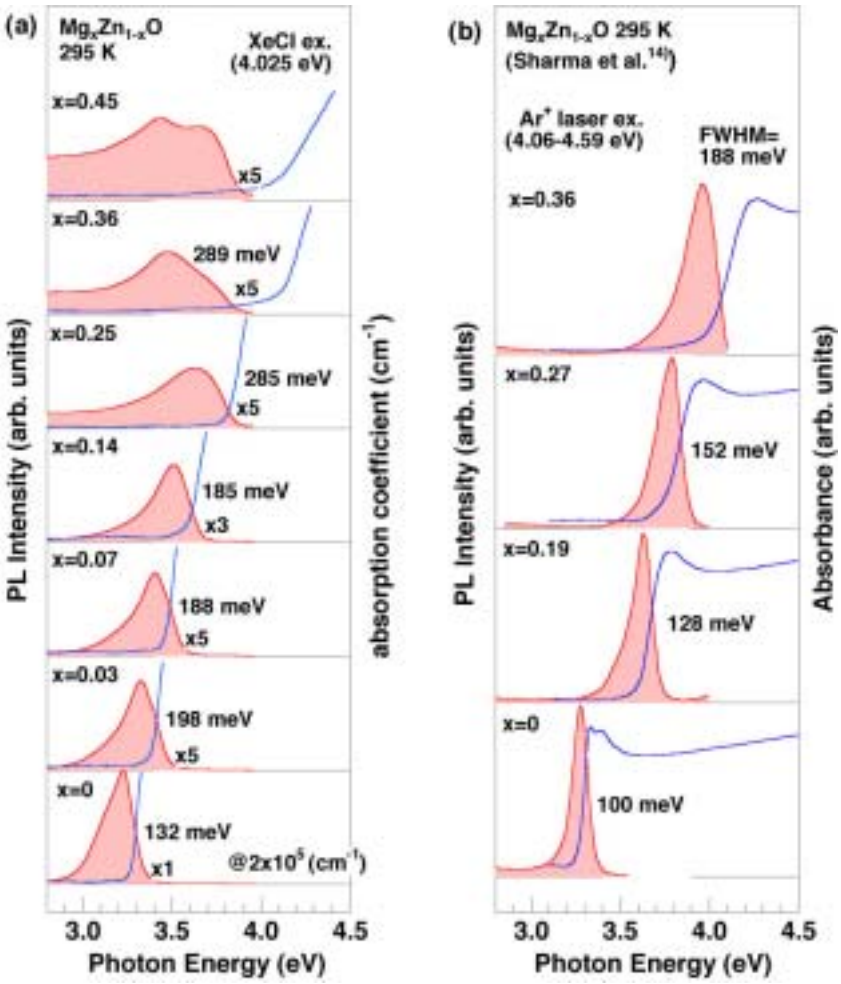

Figure 4-6. Room temperature PL and absorption spectra of (a) $Mg_xZn_{1-x}O$ films ($0<x<0.45$) grown in this study. (b) A similar spectra reported by Sharma *et al.*[14] In our case, XeCl excimer laser pulses (10 Hz, 4.025 eV) was used. FWHM values of the PL peaks and magnifications are given at the right side of each spectrum.

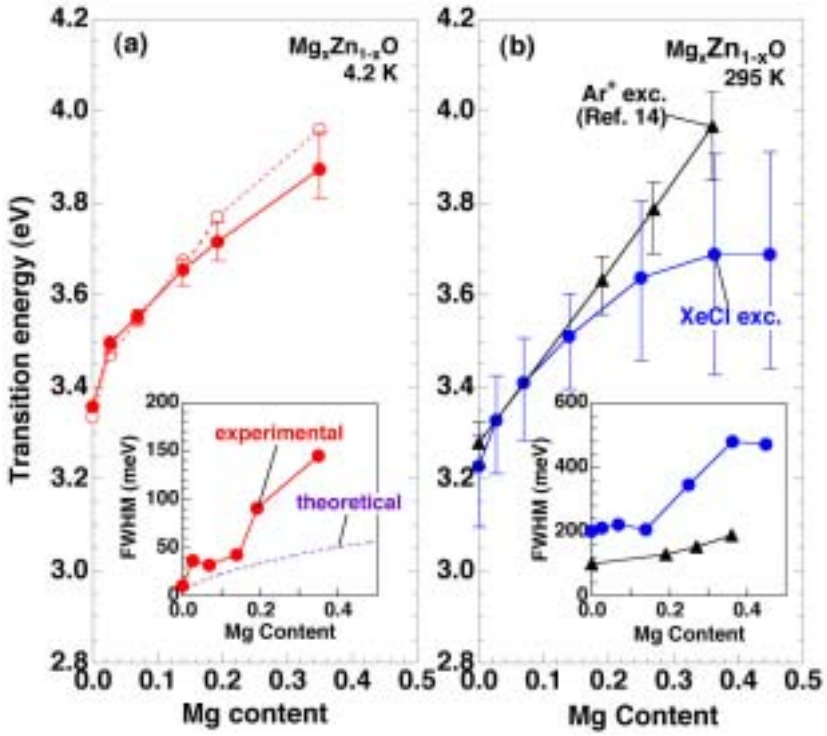

Figure 4-7. Optical transition energies of $Mg_xZn_{1-x}O$ films as a function of the Mg content measured at (a) 4.2 K and (b) 295 K. Closed and open circles are PL peak and band gap energies, respectively. Closed triangle in (b) shows PL peak energy taken from Ref. 14. Error bars indicate FWHM of PL peaks. FWHM values as a function of Mg content are plotted in the insets with the same symbols. Theoretical curve of FWHM is also denoted by a dotted line.

4.2. Thermal stability of Supersaturated $Mg_xZn_{1-x}O$ Alloy Films and $Mg_xZn_{1-x}O$/ZnO Heterointerfaces

4.2.1. Introduction

Two important requirements for realizing devices based on *p-n* junctions such as LEDs and laser diodes are valence control of ZnO to produce *p*-type material, and band gap engineering. The former is under intensive study both experimentally[16] and theoretically[17]. The latter has been partly fulfilled by the development of alloy semiconductors of $Mg_xZn_{1-x}O$ (ref.18, 19) and $Zn_{1-x}Cd_xO$ (ref. 20) to span the band gap region between 3.0 and 4.0 eV at room temperature. ZnO/$Mg_xZn_{1-x}O$ superlattices have been readily prepared to demonstrate quantum size effects (See Chapter 5).[21] Alloy films having x>0.04 in wurtzite-phase (WZ) $Mg_xZn_{1-x}O$, however, should be considered as a metastable phase because the solubility limit in the MgO-ZnO binary system was reported to be 4 mol% of MgO (Ref. 9). Therefore, it is important to know the stability of supersaturated alloy films, and their interfaces with pure ZnO films.

In this section, we have annealed $Mg_xZn_{1-x}O$ films (x=0.15, 0.22) and $Mg_xZn_{1-x}O$/ZnO heterostructures (x=0.15, 0.23) at various temperatures up to 1000° C to examine the thermal stability.

4.2.2. Experimental

The films were grown on sapphire (0001) substrates at a substrate temperature of 550° C by laser molecular-beam epitaxy (L-MBE) from sintered ceramic targets in 1×10^{-6} Torr of oxygen atmosphere. The Mg content of the as-deposited films, determined by inductively coupled plasma emission analysis was found to be more than that of the targets, as reported previously.[18] The crystalline structure was examined by powder x-ray diffraction (XRD). The transmission spectrum in the ultraviolet-visible region was measured at room temperature to determine the band gap (E_g) by using the relationship $\alpha^2 \propto h\nu - E_g$, where α is the absorption coefficient and $h\nu$ is the photon energy. The films were successively annealed at 400, 550, 700, 850, and 1000° C for 1 hour in 1 atm of oxygen. Transmission spectroscopy, scanning electron microscopy (SEM), and XRD measurements were carried out after each annealing.

4.2.3. Thermal stability of supersaturated $Mg_xZn_{1-x}O$ alloy films

In this subsection, we will discuss thermal stability of supersaturated $Mg_xZn_{1-x}O$ alloy films having Mg content above the reported solubility limit (x=0.04) to determine the actual limit. Figure 4-8 shows the XRD patterns for a 150 nm-thick $Mg_{0.22}Zn_{0.78}O$ alloy film. The as-deposited film was a highly crystalline single phase as verified by sharp (0004) doublet peaks due to Cu$K\alpha_1$ and $K\alpha_2$ for *c*-axis oriented WZ $Mg_xZn_{1-x}O$, with no detectable rock-salt-phase (RS) impurity (MgO). Up to an 850° C

annealing temperature, the impurity phase peak was hardly observed. After the film was annealed at 1000° C, a small RS(200) peak appeared at 42.82° of 2θ, indicating that the supersaturated film precipitates RS $Mg_xZn_{1-x}O$ as a secondary phase. The lattice constant of RS $Mg_xZn_{1-x}O$ was calculated to be 4.221 Å, slightly larger than that of pure MgO (4.211 Å). This lattice constant corresponds to that of RS $Mg_{0.46}Zn_{0.54}O$ bulk ceramic.[22] The crystallinity of the WZ $Mg_xZn_{1-x}O$ matrix was considerably degraded due to the segregation. A SEM image of the film annealed at 1000° C shows rectangular shaped precipitates of about 400 nm × 50 nm size, as shown in the inset of Fig. 4-8. Much smaller (100 nm × 40 nm) precipitates could be seen in the SEM image for the film annealed at 850° C, indicating the initiation of segregation. For a 150 nm-thick $Mg_{0.15}Zn_{0.85}O$ film, successive annealing up to 1000° C did not result in any segregation of RS impurity.

The E_g values for the annealed films are plotted in Fig 4-9. For the x=0.15 film, the E_g value stayed constant at about 3.56 eV. The x=0.22 film showed a decrease of E_g after annealing at 850° C and finally E_g was decreased to a value identical to that of the x=0.15 film. Therefore, the segregation of RS precipitates left the saturated WZ $Mg_xZn_{1-x}O$ matrix with lower x. Here we conclude the thermodynamic solubility limit of MgO in ZnO is x=0.15 at 1000° C.

4.2.4. Thermal stability of the $Mg_xZn_{1-x}O$/ZnO heterointerface

Now, we examine the thermal stability of the $Mg_xZn_{1-x}O$/ZnO heterointerface with x=0.15 (just at the solubility limit) and x=0.23 (far above the solubility limit). The thickness of the $Mg_xZn_{1-x}O$ was 170 nm and 230 nm for the x=0.15 and x=0.23 films, respectively, and that of ZnO was 150 nm for both the films. Figure 4-10 (a) shows the absorption spectra for the x=0.15 bilayer. The spectra for films as-deposited and annealed at 700° C showed clear absorption edges at 3.29 eV and 3.56 eV, corresponding to the band-edge of ZnO and $Mg_{0.15}Zn_{0.85}O$ layers, respectively. A- and B-exciton (A, B) and LO phonon assisted excitonic absorption (A, B-LO)[23] peaks are also clearly seen as indicated by the dotted lines. After annealing at 850° C, the absorption edge became broad. Upon annealing at 1000° C, the absorption spectrum looks like that of the x=0.08 film, showing a single band-edge at 3.43 eV. The XRD patterns shown in Fig 4-10 (b) also clearly indicate similar Mg interdiffusion behavior. Below 850° C, XRD patterns of a bilayer heteroepitaxial film having different c-axis lattice constants can be seen. After annealing at 1000° C, the XRD pattern demonstrates a single component film. We summarize the E_g values for the two heteroepitaxial bilayers (x=0.15 and x=0.23) in Fig. 4-11. Below 700° C, the bilayer structure is stable. For the bilayer having supersaturated (x=0.23) $Mg_xZn_{1-x}O$, the thermal diffusion is completed after annealing at 850° C. When thermodynamically stable $Mg_xZn_{1-x}O$ (x=0.15) is combined

with pure ZnO, a better thermal stability is demonstrated by the fact that thermal diffusion of Mg starts at 850° C and is completed after the annealing at 1000° C.

The stability of alloy films and heterostructures is summarized in Fig. 4-12. Below 700°C, supersaturated films and heterointerfaces are stable. The thermal stability of these heterointerfaces is much better than that of other II-VI semiconductors. For instance, a few minutes annealing in nitrogen ambient induced considerable interdiffusion in $ZnSe/ZnS_{0.16}Se_{0.84}$ (<650° C)[24] and $Zn_{0.79}Cd_{0.21}Se/ZnSe$ (<600° C)[25]. However, when supersaturated $Mg_xZn_{1-x}O$ with x>0.15 compositions are used in heteroepitaxial devices, considerable instability due to microscopic segregation has to be taken into account. In fact, when we made superlattices composed of ZnO and $Mg_xZn_{1-x}O$ with x=0.10 and 0.20 (Ref. 27), the former superlattice showed clear quantum size effects as seen in other III-V compound semiconductors, whereas the latter showed nonideal properties which can be attributed to the inhomogenous Mg distribution in the $Mg_xZn_{1-x}O$ barrier layers. Therefore, although the present study indicates that the supersaturated $Mg_xZn_{1-x}O$ films can be stable below 700° C, the microscopic distribution of Mg may have inhomogeneity when x exceeds 0.15.

4.2.5. Conclusions

In summary, we have examined the thermal stability of $Mg_xZn_{1-x}O$ alloy films and their heterostructures with pure ZnO. An apparent solubility limit was determined as x=0.15. Supersaturated alloy films with x=0.22 showed segregation of MgO starting around 850° C and reaching steady state at 1000° C. $ZnO/Mg_xZn_{1-x}O$ heterostructures were stable up to 700° C. These temperatures give us enough margin for the fabrication of high quality thin films and heterostructures based on ZnO, which have typical deposition temperatures around 550° C.

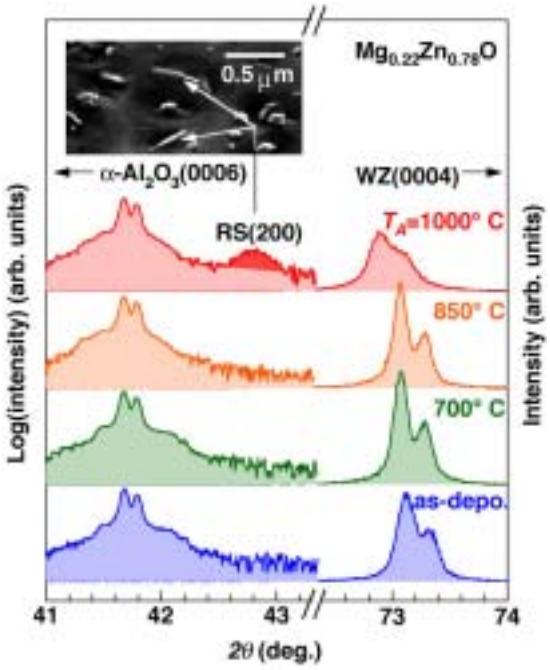

Figure 4-8. X-ray diffraction (XRD) pattern for as-deposited $Mg_{0.22}Zn_{0.78}O$ film and those after annealing at T_A=700, 850, and 1000° C. The left-hand traces containing peaks for the substrate and rock-salt-phase (RS) $Mg_xZn_{1-x}O$ (200) segregation, are plotted on a logarithmic scale, whereas the right-hand traces showing wurtzite-phase (WZ) $Mg_xZn_{1-x}O$ (0004) are plotted on a linear-scale. The inset shows a SEM image of the film surface having precipitates after annealing at 1000° C.

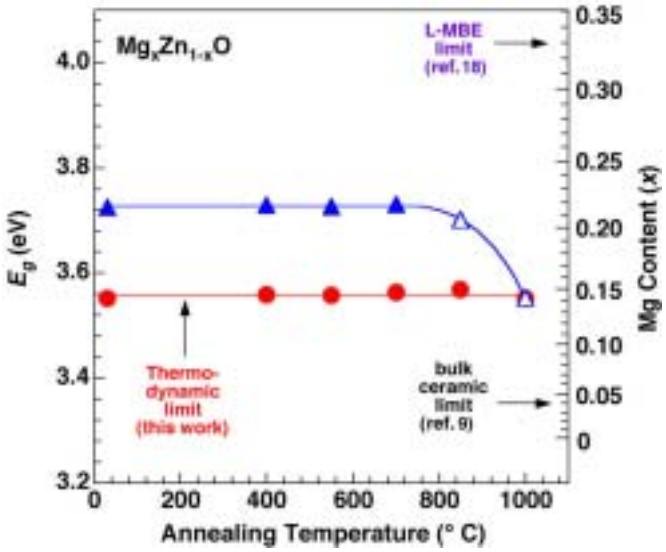

Figure 4-9. Band gap (E_g) of $Mg_{0.15}Zn_{0.85}O$ (●) and $Mg_{0.22}Zn_{0.78}O$ (▲ and △) films after annealing for 1 hour at temperatures given on the horizontal axis. Open triangles correspond to the samples having a rock-salt-phase as precipitates. The thermodynamic solubility limit found in this study was x=0.15, much higher than the reported value (x=0.04) for bulk ceramic material. The metastable solubility limit of x=0.33 for as-grown epitaxial films is also shown by the arrow denoted as L-MBE limit.

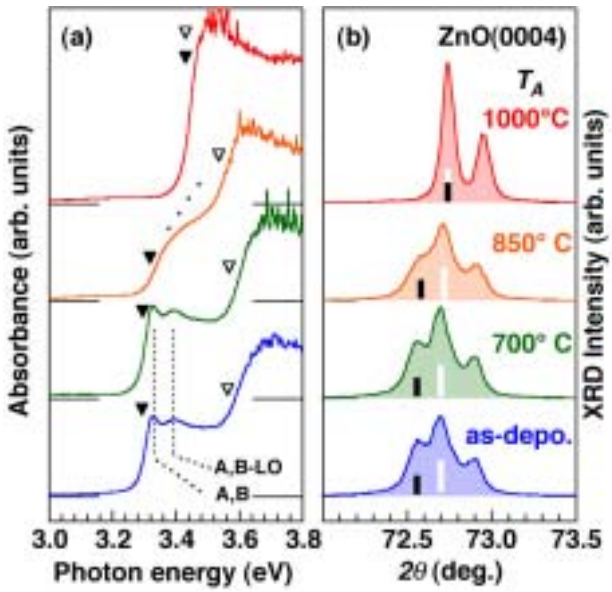

Figure 4-10. Absorption spectra (a) and x-ray diffraction patterns (b) of a $Mg_{0.15}Zn_{0.85}O$/ZnO bilayer film annealed at various temperatures. Open and closed triangles in (a) show the band-edges of $Mg_{0.15}Zn_{0.85}O$ and ZnO, respectively. White and black bars in (b) indicate the position and integrated intensity of the $K\alpha_1$ diffraction peak from the $Mg_{0.15}Zn_{0.85}O$ and ZnO layers, respectively. After 850° C annealing, considerable broadening was observed in both the absorption spectrum and the XRD pattern, indicating Mg diffusion across the heterointerface. After 1000° C annealing, diffusion was completed to form a $Mg_{0.08}Zn_{0.92}O$ alloy film.

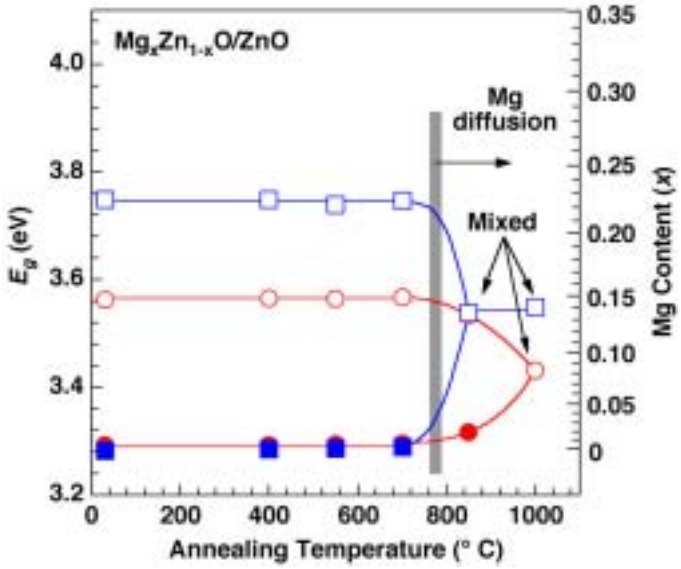

Figure 4-11. Band gap (E_g) of $Mg_xZn_{1-x}O$ (open symbols) and ZnO layers (closed symbols) deduced from the absorption spectra in Fig. 4-10 (a). ● and ○ are for the bilayer of $Mg_{0.15}Zn_{0.85}O$/ZnO an ■ and □ are for the bilayer of $Mg_{0.23}Zn_{0.77}O$/ZnO. Mg diffusion occurred when annealing was done at temperatures above 850° C for both samples. The x=0.23 sample showed complete alloying at a lower temperature than the x=0.15 sample. The vertical band denotes the temperature at which Mg diffusion initiates.

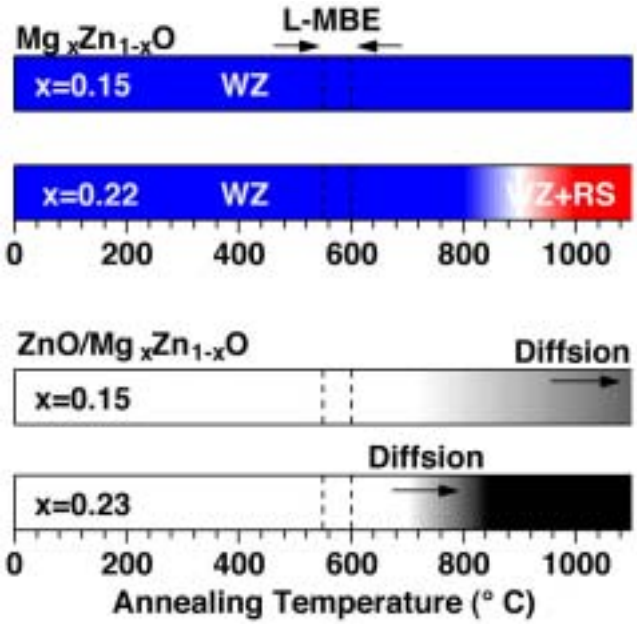

Figure 4-12. The instability of supersaturated $Mg_xZn_{1-x}O$ alloy films and $Mg_xZn_{1-x}O$/ZnO heterointerfaces is summarized. The typical L-MBE temperature range for epitaxial growth is much lower than the segregation threshold temperature (~800° C) and diffusion threshold temperature (~700° C).

4.3. Narrow Gap Semiconductor Alloy: $Zn_{1-x}Cd_xO$

4.3.1. Introduction

Wurtzite-phase $Mg_xZn_{1-x}O$ alloy having x up to 0.33 has been successfully grown to show wider band gap energy, as was discussed in the previous sections. It should be interesting to tune the band gap to lower energy side because such lower band gap material is used for an active layer in II-VI and III-nitride devices. $Zn_{1-x}Cd_xSe$ alloy has been used in blue-green ZnSe-based quantum well lasers.[26] $In_xGa_{1-x}N$ has been attracting much attention since high-brightness blue light emitting diodes based on $In_xGa_{1-x}N$ was demonstrated.[27] Very high quantum efficiency of $In_xGa_{1-x}N$ single quantum well (SQW) LED was explained by a effect due to strong localization of exciton enhanced by large compositional fluctuation of In.[28] Besides, it was reported that Indium additives is useful to reduce density of nonradiative recombination center.[29]

In this section, we have fabricated $Zn_{1-x}Cd_xO$ binary alloy by using PLD. The choice of CdO is based on the fact that ionic radius of Cd^{2+} (0.74 Å) is close to that of Zn^{2+} (0.60 Å), that is, wurtzite phase alloy can be expected in spite of RS structure of CdO. The thermodynamic solubility limit of CdO in ZnO has been reported to be less than 2 mol %, according to the phase diagram of the ZnO–CdO-P_2O_5 ternary system.[30]

4.3.2. Experimental

$Zn_{1-x}Cd_xO$ films were grown on sapphire (0001) substrates, polished on both sides, by pulsed laser deposition in an ultrahigh vacuum chamber. High purity ZnO (5N) and CdO (5N) powders were mixed to form the targets (20 mm in diameter) with Cd content ranging from x=0 to x=0.30. Pressed pellets were sintered at temperature from 600 to 750° C in air. Relatively low sintering temperature was used for the targets with $0.15 \leq x \leq 0.30$ to suppress decomposition and vaporization of Cd-related species. The Cd contents in the obtained targets were found slightly lower than the original contents by judging from electron probe microanalyses (EPMA). The target color changed from yellowish white to dark brown with increasing Cd content. The target having x>0.30 was hardly prepared because of high vapor pressure of Cd. The targets were placed at a distance of 4 cm from the substrate and ablated by KrF excimer laser pulses (248 nm, 10 Hz, 30 ns) with a fluence of 1 J/cm^2. The films (~200 nm-thick) were deposited at a temperature ranging from 400 to 600° C in 5×10^{-5} Torr of pure oxygen (6N). Some of the films were annealed in air after the deposition. The results will be discussed with the films grown 400° C as far as any note is given. The Cd content in the $Zn_{1-x}Cd_xO$ films was determined by EPMA and ICP optical emission spectroscopy. The surface morphology of the films was examined by means of contact-mode

atomic force microscopy (AFM). The crystal structure of the films was analyzed by a high-resolution XRD apparatus. Optical properties were characterized by absorption and PL spectroscopies at room temperature and at 4.2 K. A continuous He–Cd laser (325 nm, 5mW) were used for the PL measurements.

4.3.3. Film composition and structural properties

Deposition rate of the films was about 5×10^{-3} nm/pulse. Figure 4-13 (a) shows growth temperature (T_g) dependence of the Cd content in the films as a function of that in the targets. In contrast to $Mg_xZn_{1-x}O$ alloy[18], Cd content in the $Zn_{1-x}Cd_xO$ films is smaller than that in the targets, as shown in the inset. The dilution factors are 20 and 5 for the films grown at T_g=400 and 600° C, respectively. This behavior can be again attributed to the difference between vapor pressures of Cd and Zn. Vapor pressures of Mg, Zn, and Cd are plotted as a function of temperature in Fig. 4-13 (b). Here is surprising fact that the maximum Cd content of x=0.07 is larger than the reported value. This advantage associated with nonequiliblium nature of PLD growth further gives us opportunity to investigate novel alloy systems based on ZnO.[31] The solubility limit of Cd into wurtzite ZnO could not be evaluated in this study because of Cd incorporation due to the high vapor pressure.

All the films had *c*-axis orientation and WZ-phase without any impurity phase such as RS and spinel phase. The crystallinity of the films was measured by XRD ω- and ω-2θ scans for the ZnO (0002). As the Cd content increases, FWHM for both scans increases, as shown in Fig. 4-14 (a). Above x=0.05, considerable degradation is observed presumably due to large compositional fluctuation. The cell volume ($\sqrt{3}/2a^2c$) and *a*- and *c*-axis length measured by high-resolution XRD are plotted as a function of Cd content in Fig. 4-14 (b) and (c), respectively. The cell volume varies 1.5 % at x=0.07 compared to pure ZnO, showing a good agreement with the variation of mean cation radius (1.6 %) at the same *x*. Both lattice constants gradually increase, with increasing alloying composition *x*. The *x* dependence of the *a*- and *c*- axis lengths can be fitted by a=3.252+0.143x-0.147x^2 and c=5.204+0.956x-5.42x^2, respectively. Assuming strain is not included in the films, the *c*-axis length increases much rapidly than the *a*-axis length with increasing *x*. A ratio of *c*/*a* in the wurtzite crystal depends on electronegativity of the compounds.[32] Much smaller electronegativity causes increasing *c*/*a*.[33] Therefore, this behavior is attributed to the smaller electronegativity of Cd ions than that of Zn ions. As for $Mg_xZn_{1-x}O$ alloy films[18], we have observed a contrast behavior due to relatively larger electronegativity of Mg ions.

We have tested the thermal stability of the $Zn_{1-x}Cd_xO$ films. A 700° C annealing is found to be essential for improving compositional homogeneity and crystallinity. When the samples were annealed at 800° C in air, considerable reduction of the Cd concentration took place due to Cd evaporation during the annealing. After an 1000° C annealing, Cd content became close to zero.

4.3.4. Optical properties

The $Zn_{1-x}Cd_xO$ alloy films showed narrower band gap energies. Figure 4-15 shows absorption spectra of the as-grown films measured at room temperature. Clear band gap shift towards lower energy side can be clearly seen according the Cd content. Broad shoulder seen in the spectrum of the x=0.073 film indicates formation of Cd-rich phase but a bit of amount compared to the major matrix. The highest E_g values of this film was evaluated to be 2.99 eV. The fitting curve for the measured E_g values at $0 \leq x \leq 0.043$ extrapolates this E_g value well so that we could obtain a formula, $E_g(x)=3.29-4.40x+5.93x^2$, to express the x dependence of E_g value at room temperature, as shown in the inset.

Figure 4-16 shows PL and absorption spectra of the as-grown films taken at room temperature. Single PL lines can be seen at each absorption edge. PL peak width does not increase dramatically with increasing Cd content. Figure 4-17 shows PL spectra of the as-grown films (dotted lines) and annealed films (solid lines) taken at 4.2 K. Low temperature PL spectroscopy is a suitable method to detect inhomogeneous potential fluctuation because the photo-excited carriers cannot travel long distance, resulting in radiative recombination after relaxation into local potential minima. PL peak energy for all the samples is plotted as a function of Cd content in Fig. 4-18. In contrast to room temperature PL spectra, PL peak width of the as-grown films rapidly increases with growing lower energy shoulder as x increases. This is presumably due to larger compositional fluctuation or poorer crystallinity for larger x films. While, the annealed films show much shaper line widths and smaller low-energy tailings, although the broadening behavior is still remained. This considerable broadening can be explained by so-called *alloy broadening effect*. Alloy broadening of exciton line width in II-VI semiconductors was theoretically expressed by the following equation, if Gaussian line shape is assumed,[15]

$$\Delta(x) = 2\sqrt{2\ln 2}\,[dE_x(x)/dx]\sqrt{x(1-x)V_0(x)/V_{ex}(x)} \qquad (4\text{-}1),$$

where $\Delta(x)$ is the FWHM value of an excitonic PL line, $E_{ex}(x)$ is the exciton transition energy which is dependent on x, $V_0(x)$ is the cell volume as was defined above, $V_{ex}(x)$ is the excitonic volume expressed by $V_{ex}(x)=8\pi r_B^3(x)$, where $r_B(x)$ denotes the Bohr radius of exciton.[15] Assuming $r_B(x)$ in the alloy is a constant at the value of pure ZnO (18 Å), calculated $\Delta(x)$ shows excellent agreement with the observed FWHM values at $0<x<0.022$, as can be seen in the inset of Fig. 4-18. Considerable deviation between experimental and theoretical curves above x=0.043 might be attributed to crystalline defect. It is also likely that there is microscopic compositional fluctuation in the films including larger x. Actually, integrated luminescence intensity of the annealed samples increases up to x=0.022, and then rapidly

decreases towards x=0.073. The intensity of x=0.022 is 15 times larger than that of the pure ZnO film, indicating possible reduction of non-radiative recombination center.

Much smaller PL peaks observed in the annealed films can be seen in Fig. 4-19 with logarithmic scales of the vertical axis. Here we note the small PL peaks at 3.367 eV, which are observed for all the films. We never observed these luminescence lines in the as-grown samples. It is natural to think that phase separation takes place during thermal annealing because these PL peak positions locate between I and E_A^{ex}, where I is neutral donor bound exciton emission, and E_{AB}^{ex} is A-, and B- exciton energy for the pure ZnO. At lower energy side, some small peaks, which can be assigned by donor-acceptor pair (DAP), and LO-phonon replicas (*ex*-1LO and *ex*-2LO) of the exciton lines (*ex*) is also seen. Visible DAP lines indicates less crystalline quality. Nonetheless, rather larger PL intensity could be demonstrated as was discussed above. In addition, the structural property of the $Zn_{1-x}Cd_xO$ films gives us unique advantage if this material is used to fabricate the heterostructures with $Mg_xZn_{1-x}O$ alloy. The structural and optical properties of the both alloys are summarized in a plane of the a-axis length and the room temperature E_g value as shown in Fig. 4-20. Using these alloy films, we can construct novel heterostructure having band offset up to 0.9 eV achieving *perfect lattice-matching*, because the a-axis lengths for the both alloys increase with increasing alloying compositions. Such a novel property can never be obtained for III-nitrides alloy system. $In_xGa_{1-x}N$ shows very large variation of the a-axis length. If strain exists along the in-plane direction of a wurtzite crystal, piezoelectric field is induced in the c-axis direction. In case of quantum well, electrons and holes confined in well layers are spatially separated due to internal electric field. In fact, extremely large piezoelectric field induced by strain is a significant issue in III-nitrides based on devices.[34] Even though it is difficult to obtain high-crystalline quality $Zn_{1-x}Cd_xO$ films due to necessary low temperature growth, we can conclude that this material is potential candidate for an active layer in blue LED based on ZnO.

4.3.5. Conclusion

New II-VI semiconductor alloy $Zn_{1-x}Cd_xO$ films with x up to 0.07 have been grown by pulsed laser deposition. Band gap could be tuned to lower energy side by 0.3 eV at x=0.07. Post-annealing was found to improve the crystalline quality of the films, resulting in excellent luminescence properties. The a- and c-axis lengths increased as x increases but the variation was quite small. If this alloy is applied in a heterostructure with $Mg_xZn_{1-x}O$ alloy, strain-free quantum well structures with the band offset up to 0.9 eV would be fabricated.

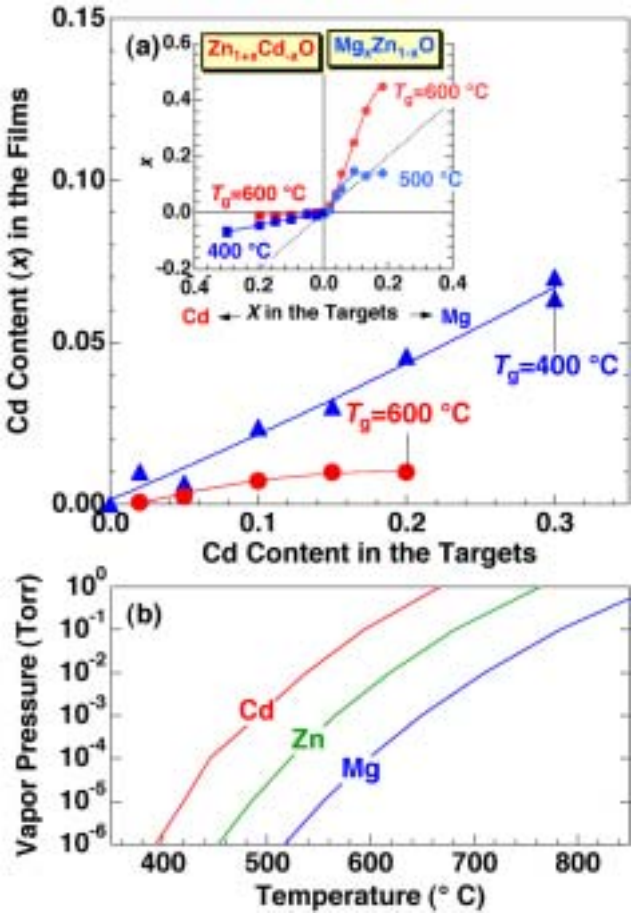

Figure 4-13. (a) Growth temperature dependence of Cd content in the $Zn_{1-x}Cd_xO$ epitaxial films as a function of Cd content in the targets. Inset shows similar plot togather with the case of $Mg_xZn_{1-x}O$ alloy films reported in Ref. 18. (b) Temperature dependence of vapor pressures for Cd, Zn and Cd. The dilution ($Zn_{1-x}Cd_xO$) and concentration ($Mg_xZn_{1-x}O$) of alloy compositions is attributed to the differences of vapor pressures.

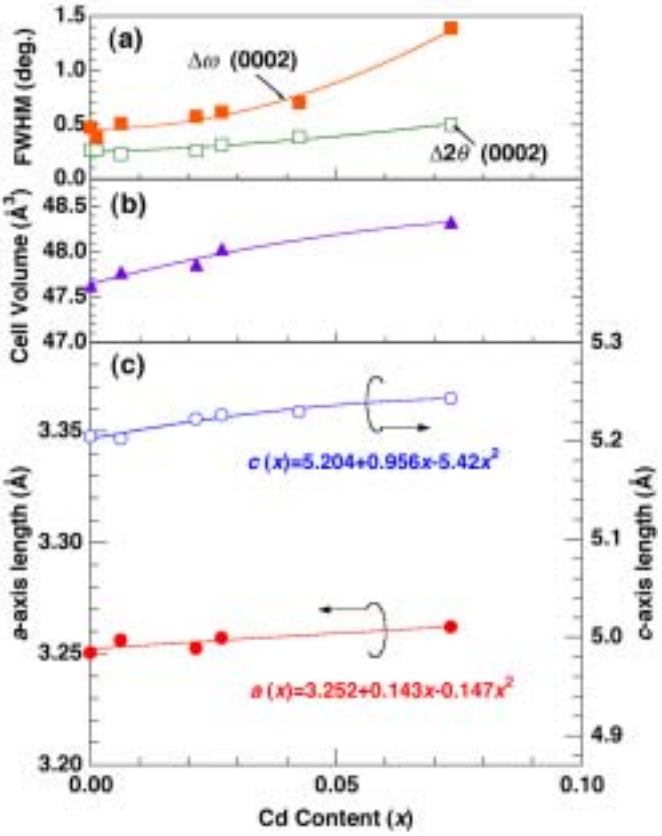

Figure 4-14. Cd content dependence of (a) FWHM values of ω- and ω-2θ scans for the ZnO (0002) peak, (b) cell volume, and (c) the *a*- and *c*-axis lattice constants of the $Zn_{1-x}Cd_xO$ films. The solid lines in (c) are fitted lines expressed as a=3.252+0.143x-0.147x^2 and c=5.204+0.956x-5.42x^2.

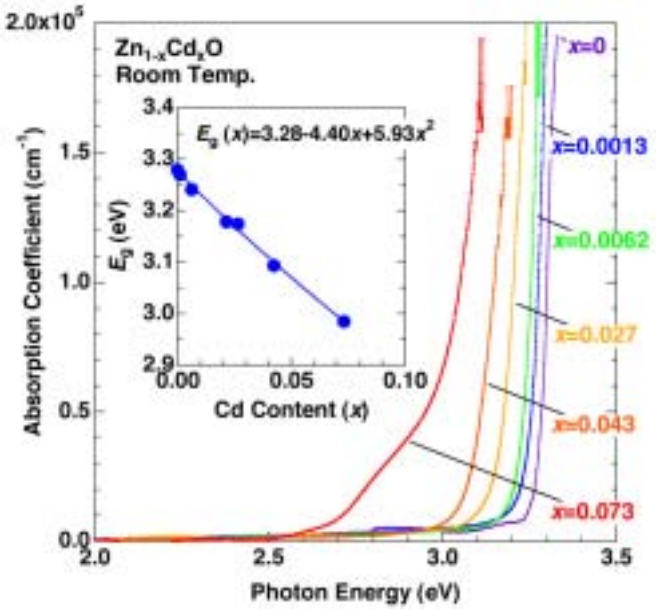

Figure 4-15. Absorption spectra of $Zn_{1-x}Cd_xO$ films measured at room temperature. The inset shows band gap (E_g) as a function of Cd content.

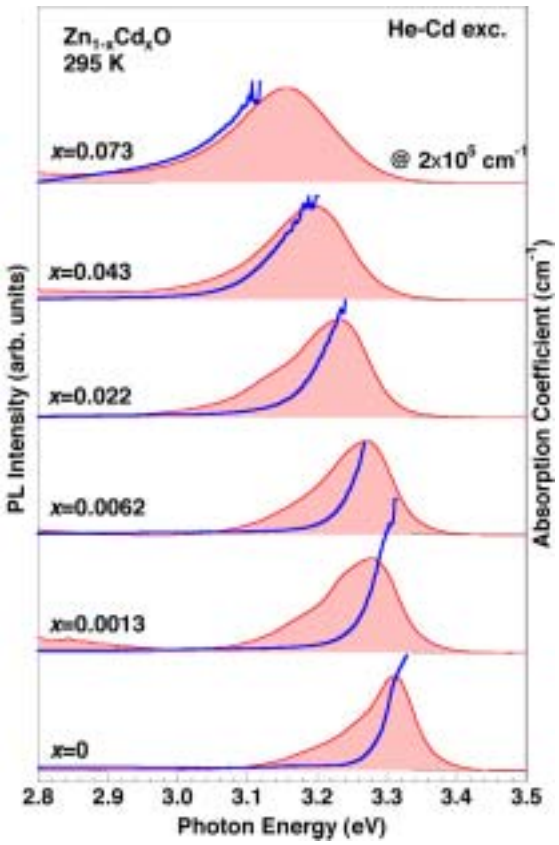

Figure 4-16. Room temperature PL and absorption spectra of the $Zn_{1-x}Cd_xO$ films ($0<x<0.073$) grown at 400° C.

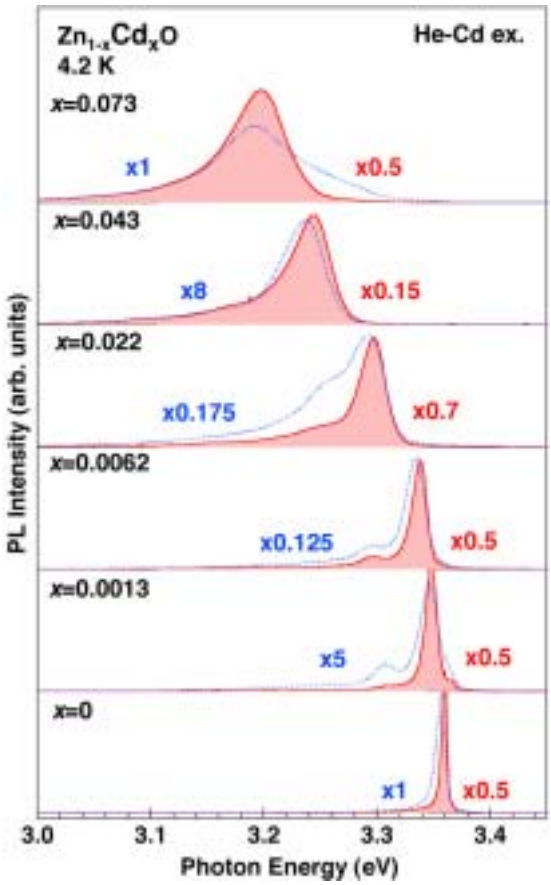

Figure 4-17. PL spectra of the as-grown (dashed lines) and the annealed $Zn_{1-x}Cd_xO$ (solid lines) films measured at 4.2 K. Vertical magnifications are given in the sides of the spectra.

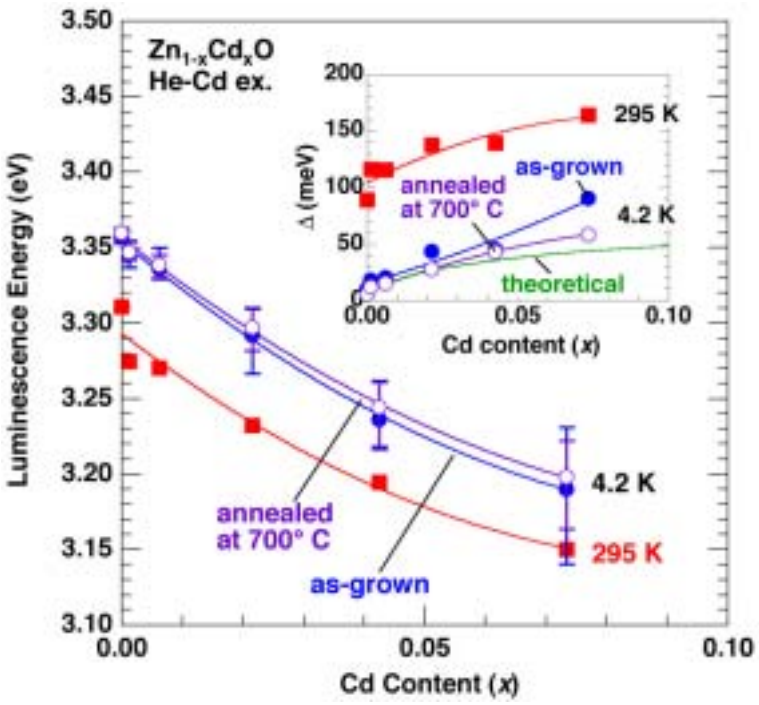

Figure 4-18. Photoluminescence peak energies of $Zn_{1-x}Cd_xO$ films as a function of Cd content measured at 4.2 K (● and ○) and 295 K (■). ● and ○ are for the as-grown and the annealed films, respectively. Error bars indicate FWHM of PL peaks. The FWHM values as a function of Cd content are plotted in the inset with the same symbols. Theoretical curve of FWHM value at 0 K is also presented.

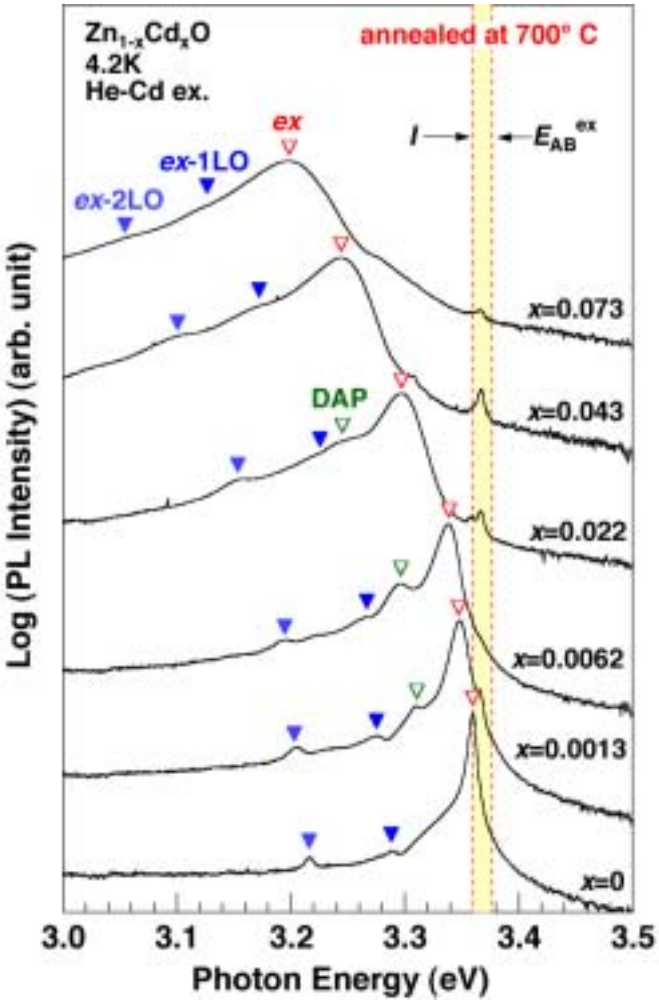

Figure 4-19. PL spectra of the annealed $Zn_{1-x}Cd_xO$ films, which are same to those shown in Fig. 4-17 (solid lines). Vertical axis is presented in logarithmic scale. *I* and E_{AB}^{ex} are neutral bound exciton energy and free-exciton energy of *A* and *B* excitons, respectively, which are observed in pure ZnO films. DAP and ex-*n*LO (*n*=1, 2) stands for the peaks assigned to donor-acceptor pair emission and LO-phonon replicas of the exciton emission (*ex*).

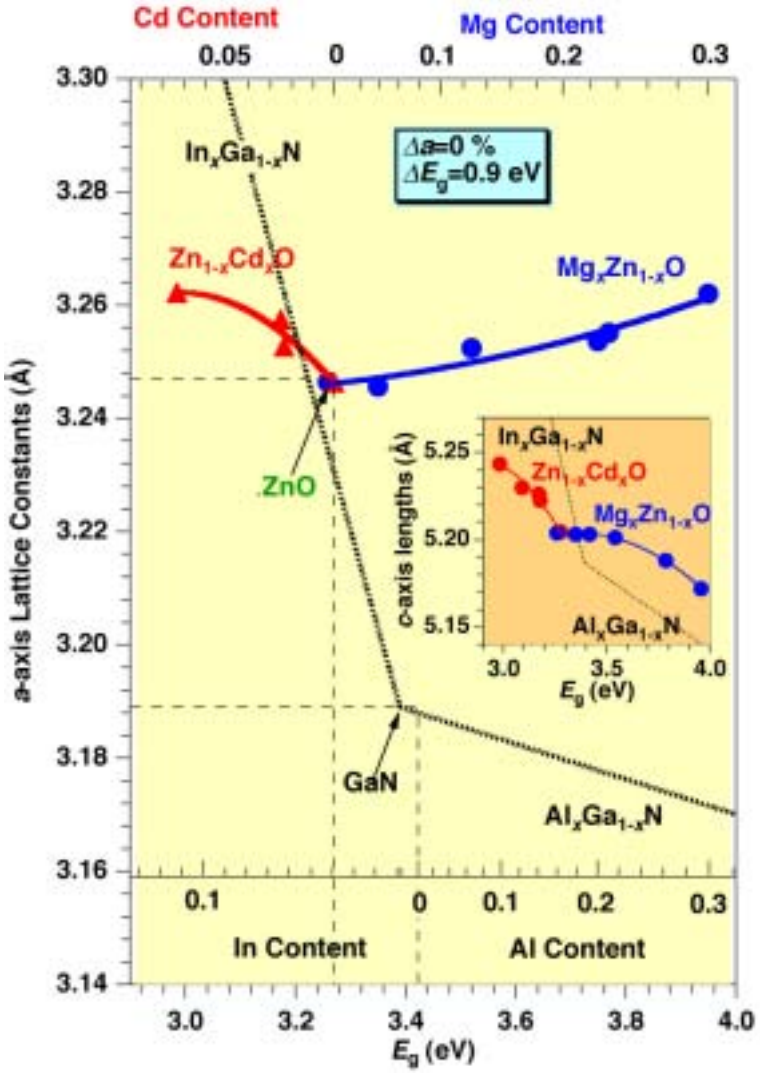

Figure 4-20. The optical and structural parameters of $Zn_{1-x}Cd_xO$ and $Mg_xZn_{1-x}O$ alloy films are mapped out in a plane of *a*-axis length and band gap at room temperature. Similar plot for $In_xGa_{1-x}N$ and $Al_xGa_{1-x}N$ alloy are also shown. Scales of alloy compositions are attached in the top and inside of the figure. Inset depicts similar plots for the *c*-axis length.

References

[1] I. Hayashi, M. B. Panish, P. W. Foy, and S. Sumski, Appl. Phys. Lett. **17**, 109 (1970).

[2] Z. K. Tang, P. Yu, G. K. L. Wong, M. Kawasaki, A. Ohtomo, H. Koinuma, and Y. Segawa, Solid State Commun. **103**, 459 (1997).

[3] Y. Segawa, A. Ohtomo, M. Kawasaki, H. Koinuma, Z. K. Tang, P. Yu, and G. K. L. Wong, Phys. Stat. Sol. **B202**, 669 (1997).

[4] K. Minegishi, Y. Koiwai, Y. Kikuchi, K. Yano, M. Kasuga, and A. Shimizu, Jpn. J. Appl. Phys. **36**, L1453 (1997); J. T. Cheung (private communication).

[5] H. Okuyama, K. Nakano, T. Miyajima, and K. Akimoto, Jpn. J. Appl. Phys. **30**, L1620 (1991).

[6] R. D. Shannon, Acta Crystallogr. Sect. A: Cryst. Phys. Diffr. Theor. Gen. Crystallogr. **32**, 751 (1976).

[7] H. Koinuma, M. Kawasaki, and M. Yoshimoto, Mat. Res. Soc. Symp. Proc. **397**, 145 (1996).

[8] R. E. Honig and D. A. Kramer, RCA Rev. **30**, 285 (1969).

[9] J. F. Sarver, Fred L. Katnack, and F. A. Hummel, J. Electrochem. Soc. **106**, 960 (1959).

[10] R. E. Leuchtner, Mat. Res. Soc. Symp. Proc. **397**, 157 (1996).

[11] M. Sano and M. Aoki, Jpn. J. Appl. Phys. **15**, 1943 (1976).

[12] For example, R. Zimmermann, J. Cryst. Growth **101**, 346 (1990).

[13] E. C. Heltemes and H. L. Swinney, J. Appl. Phys. **38**, 2387 (1967).

[14] A. K. Sharma, J. Narayan, J. F. Muth, C. W. Teng, C. Jin, A. Kvit, R. M. Kolbas, and O. W. Holland, Appl. Phys. Lett. **75**, 3327 (1999).

[15] R. Zimmermann, J. Cryst. Growth **101**, 346 (1990).

[16] K. Minegishi, Y. Koiwai, Y. Kikuchi, K. Yano, M. Kasuga, and A. Shimizu, Jpn. J. Appl. Phys. **36**, L1453 (1997).

[17] T. Yamamoto and H. Yoshida, Jpn. J. Appl. Phys. **68**, L166 (1999).

[18] A. Ohtomo, M. Kawasaki, T. Koida, K. Masubuchi, H. Koinuma, Y. Sakurai, Y. Yoshida, T. Yasuda, and Y. Segawa, Appl. Phys. Lett. **72**, 2466 (1998).

[19] Y. Matsumoto, M. Murakami, Z.W. Jin, A. Ohtomo, M. Lippmaa, M. Kawasaki, and H. Koinuma, Jpn. J. Appl. Phys. **38**, L603 (1999)

[20] M. Kawasaki, A. Ohtomo, R. Shiroki, I. Ohkubo, H. Kimura, G. Isoya, T. Yasuda, Y.Segawa, and H. Koinuma, *Extended Abstracts of International Conference on Solid State Devices and Materials, Hiroshima, Japan* (1998) p. 356.

[21] A. Ohtomo, M. Kawasaki, I. Ohkubo, H. Koinuma, T. Yasuda, and Y. Segawa, Appl. Phys. Lett. **75**, 980 (1999).

[22] E. R. Segnit and A. E. Holland, J. Am. Ceram. Soc. **78**, 409 (1965).

[23] W. Y. Liang and A. D. Yoffe, Phys. Rev. Lett. **20**, 59 (1968).

[24] G. Bacher, D. Tonnies, D. Eisert, A. Forchel, M. O. Moller, M. Korn, B. Jobst, D. Hommel, G. Landwehr, J. Sollner, and M. Heuken, J. Appl. Phys. **79**, 4368 (1996).

[25] R. C. Tu, Y. K. Su, Y. S. Huang, and S. T. Chou, J. Appl. Phys. **84**, 6017 (1998).

[26] M. A. Hasse, J. Qiu, J. M. DePuydt, and h. Cheng, Appl. Phys. Lett. **59**, 1272 (1991).

[27] S. Nakamura, M. Senoh, N. Iwasa, S. Nagahara, T. Yamada, and T. Mukai, Jpn. J. Appl. Phys. **34**, L1332 (1995).

[28] S. Chichibu, K. Wada, and S. Nakamura, Appl. Phys. Lett. **71**, 2346 (1999).

[29] Y. Narukawa, S. Saijou, Y. Kawakami, and Sg. Fujita, T. Mukai, and S. Nakamura, Appl. Phys Lett. **74**, 558 (1999).

[30] J. J. Brown and F. A. Hummel, J. Electron. Soc. **111**, 1056 (1964).

[31] See for example, T. Fukumura, Z.W. Zin, A. Ohtomo, Y. Matsumoto, H. Koinuma, and M. Kawasaki, Appl. Phys. Lett. **75**, 3366 (1999), and Zhengwu Jin, M. Murakami, T. Fukumura, A. Ohtomo, M. Kawasaki, and H. Koinuma, J. Cryst. Growth, in press.

[32] H. Schulz and K. H. Thiemann, Solid State Commun. **32**, 783 (1979).

[33] Y. Oumi, H. Takaba, S. S. C. Ammal, M. Kubo, K. Teraishi, A. Miyamoto, M. Kawasaki, M. Yoshimoto, H. Koinuma, Jpn. J. Appl. Phys. **38**, 2603 (1999).

[34] T. Takeuchi, S. Sota, M. Katsuragawa, M. Komori, H. Takeuchi, H. Amano and I. Akasaki, Jpn. J. Appl. Phys. **36**, L382 (1997).

Chapter 5. Structure and Optical Properties of ZnO/$Mg_xZn_{1-x}O$ Superlattices Grown on Sapphire (0001) Substrates

Abstract

ZnO/$Mg_{0.2}Zn_{0.8}O$ superlattices having a band gap offset of about 0.5 eV were epitaxially grown by laser molecular-beam epitaxy on sapphire(0001) substrate using ZnO buffer layer. The use of buffer layer was very essential to obtain smooth surface $Mg_xZn_{1-x}O$ surface and sharp heterointerface between ZnO and $Mg_xZn_{1-x}O$ layers. The superlattice structure with period ranging from 8 to 18 nm was clearly verified by cross-sectional transmission electron microscopy, Auger depth profile, and x-ray diffraction. As the well layer thickness decreased below 5 nm, the photoluminescence peak and absorption edge in photoluminescence excitation spectra showed a blue shift, indicating quantum size effect. Energy discontinuity of conduction band minimum at ZnO/$Mg_{0.2}Zn_{0.8}O$ heterointerface was evaluated to be about 0.4 eV as the best fitting parameter of well width dependence of quantum sub-band energy.

5.1. Introduction

Recently, considerable attention is being paid to ZnO as a widegap oxide semiconductor. ZnO has a bandgap of 3.37 eV at room temperature, thus a potential candidate for ultraviolet light emission. We have demonstrated the room temperature laser action with a low threshold (24 kW/cm^2) from optically pumped ZnO thin films composed of hexagonally shaped nanocrystals closely assembled in a honeycomb fashion.[1] There are three interesting findings of this phenomenon. First, the stimulated emission process was caused by exciton-exciton collision even at room temperature because of the very large exciton binding energy (60 meV)[2]. Second, the threshold of this excitonic process was very low when the nanocrystalline size was tuned at about 50 nm.[3] Third, the longitudinal cavity was automatically formed by making use of the grain boundaries between hexagonal nanocrystals acting as mirrors.[4, 5] Recently we have reported that $Mg_xZn_{1-x}O$ alloy films can be prepared by pulsed laser deposition which show higher bandgap up to 4 eV and have similar lattice constants to pure ZnO.[6] Emission process with exciton recombination further can be enhanced if such low dimensional structures as quantum wells, wires, and dots are constructed.

In this chapter, we will discuss the structural characterization and optical properties of $ZnO/Mg_{0.2}Zn_{0.8}O$ superlattices. Quantum confinement effect was observed in photoluminescence (PL) and photoluminescence excitation (PLE) spectroscopies.

5.2. Fabrication of $ZnO/Mg_xZn_{1-x}O$ Superlattices

5.2.1. Effects of ZnO buffer layer

We used a ZnO buffer layer prior superlattice deposition on sapphire substrates. Here we will discuss with focusing the effects of ZnO buffer layer. When the $Mg_xZn_{1-x}O$ films were deposited directly on sapphire, the surface showed relatively rough compared with pure ZnO films, as shown in Fig. 5-1 (a). The root mean square (rms) roughness of 400 nm-thick film with x=0.20 was as large as 10 nm. The surface flatness can be improved by inserting a 200 nm-thick ZnO buffer layer, resulting in the rms roughness of 1 nm (Fig. 5-1 (b)). The film morphology was greatly improved by inserting a ZnO buffer layer as thin as 1 nm.[6]

In order to examine an effect of buffer layer in successive deposition of ZnO layer on the $Mg_xZn_{1-x}O$ films, x-ray photoelectron spectroscopy (XPS) study was performed. Thin ZnO layers were deposited on the same samples shown in the AFM images, with controlling layer thickness from 1.7 to 5.7 nm. The

$Mg_xZn_{1-x}O$ samples were cut to yield 4~5 pieces and used for the each deposition. The samples were explored to air, and then transferred into a XPS chamber after photochemical surface cleaning in an atmospheric ozone with UV light irradiation using a low-pressure mercury lamp.[7] In XPS measurements, a x-ray beam generated from a Mg filament was used to yield photoelectron signal. Mg2*p* signal from bottom $Mg_xZn_{1-x}O$ layer was detected with number of accumulations. Figure 5-2 (a) shows Mg2*p* spectra taken from the samples deposited on the buffered $Mg_xZn_{1-x}O$ films. As ZnO layer thickness (*d*) decreases, signal intensity increases. Integrated intensity of Mg2*p* peaks for the both samples is plotted as a function of *d* in natural logarithmic scale in Fig. 5-2 (b). Obviously, damping rate for the case of buffered films is larger than that for the case of non-buffered films, indicating much smoother surface of the ZnO layer deposited on buffered $Mg_xZn_{1-x}O$ films. The dotted line in the figure is a simulation curve assuming ideal two-dimensional growth, calculated using Lambert's Low, $I(d)=I_0\exp(-d/\lambda)$, where $I(d)$ is photoelectron intensity, I_0 is the intensity at $d=0$, and λ is mean free path of photoelectron. It can be seen slight deviation between experimental curve for the buffered films and simulation curve. We suppose that this may be caused by consistent inhomogeneous growth of ZnO, or by thermal diffusion of Mg ions into top ZnO layer. When the superlattice was directly fabricated on sapphire, surface morphology was not smooth and satellite peaks in x-ray diffraction (XRD) pattern due to superlattice periodicity could not be observed. As is described later, superlattice peaks could be clearly visible, when ZnO buffer layer (100 nm) was employed before superlattice growth. Thus, it can be concluded that the use of buffer layer is effective to keep $Mg_xZn_{1-x}O$ film surface smooth and to improve thickness homogeneity of the second ZnO layer.

5.2.2. *In-situ* RHEED monitoring of ZnO/$Mg_xZn_{1-x}O$ heteroepitaxial growth

ZnO/$Mg_xZn_{1-x}O$ superlattices were fabricated by laser molecular-beam epitaxy (MBE), *i.e.* pulsed laser deposition from ceramic targets along with reflection high energy electron diffraction (RHEED) observation in an ultra-high vacuum chamber.[8] Mg content of the barrier layer was chosen at $x=0.20$, corresponding to a band-offset of about 0.5 eV at the heterointerface with pure ZnO. Oxygen pressure was kept constant at 1×10^{-6} Torr during the deposition. Before the deposition of superlattice, a 100 nm-thick ZnO buffer layer was grown on sapphire(0001) substrate at 550° C. The surface characteristics of the superlattices are summarized in Fig. 5-3 with the design of superlattices structure. RHEED patterns with the ZnO [11-20] azimuth for a buffer layer and superlattice (L_W=5.7 nm) are shown in Fig. 5-3 (c and b), respectively. Throughout the deposition, such RHEED pattern with fine streaks was maintained, indicating all the layers were epitaxially grown. Weak three-fold streaks associated with superstructure

can be also seen in the picture taken from the [10-11] direction of ZnO Pure ZnO films grown under the similar conditions also showed such streaks. Although the origin of this structure has not yet understood, excess zinc atoms or oxygen vacancies at the surface might be presented to form surface reconstruction. Fig. 5-3 (e and d) show AFM images of the ZnO buffer layer and the superlattice, respectively. Hexagonally shaped grains and steps with a height of 0.52 nm are clearly seen in the both images, indicating that epitaxial growth took place in a spiral growth mode. The root mean square (rms) roughness of ZnO and the superlattices are as small as 0.5 and 0.8 nm, respectively.

5.2.3. Control of structural parameters

The superlattice with 10 periods was fabricated on the ZnO buffer layer at 650° C. The deposition temperatures for ZnO buffer layer and for superlattice were independently optimized to obtain smooth surface. ZnO layer thickness (L_W) was varied from 1.7 nm to 12 nm maintaining $Mg_{0.2}Zn_{0.8}O$ layer thickness (L_B) constant at 6.2 nm. A schematic of superlattice structure is given in Fig. 5-6 (a). The layer thickness was controlled by deposition time by taking into account the deposition rate predetermined by single layer deposition experiments. In order to determine Mg content of the barrier layer, $Mg_xZn_{1-x}O$ single layer films were grown on sapphire under the same condition using $Mg_{0.1}Zn_{0.9}O$ target and the composition was analyzed by inductively coupled plasma (ICP) optical emission spectroscopy by dissolving the films in HNO_3 (0.1 mol/l) solution. Note that we have chosen x=0.1 of the target because of Mg condensation during growth due to larger vapor pressure of ZnO than that of MgO.[6]

Figure 5-4 shows small-angle ω-2θ XRD patterns. The solid line is obtained from experiment and the dotted curve is a simulation, calculated by using a theoretical model[9] assuming the interface rms roughness of ~1 nm as evaluated by AFM image. Peaks corresponding to the superlattice reflection were consistently observed for all superlattices. The period deduced from superlattice peaks is plotted in Fig. 5-5 as a function of the deposition time for the well layers. As can be seen, the superlattice periodicity has excellent agreement with the designed one. Precise control of layer thickness as well as Mg content in the barrier layers can enable us to determine various material parameters from the optical properties, as be discussed later. This technique has been further employed for combinatorial laser molecular-beam growth, with very high-throughput experiments (See Chapter 7).

5.3. Structural and Optical Characteristics of ZnO/$Mg_{0.20}Zn_{0.80}O$ Superlattices

5.3.1. Structural properties

The superlattice structure was characterized by cross-sectional transmission electron microscope (TEM), depth profiling using Auger electron spectroscopy (AES), and XRD reciprocal space mapping (See Chapter 3 in detail) using high-resolution x-ray diffractometer (Philips, X'-pert MRD). Figure 5-6 (b) shows TEM image of a superlattice with L_W=5.7 nm. The designed layer structure is clearly seen as a modulation of the contrast. The depth profile of Mg content in a superlattice was measured by AES and plotted in Fig. 5-6 (c). As can be clearly seen, the regular oscillation was observed till the end of the superlattice, indicating that the interface diffusion at the bottom interfaces during the successive film deposition is negligible.

In superlattices composed of alloy semiconductors, in-plane lattice mismatch is an important parameter in the case of strained superlattices. With increasing Mg content (x in $Mg_xZn_{1-x}O$) a-axis length expands as $3.250+0.036x$.[6] Therefore, in-plane lattice mismatch of 0.22 % is applied for superlattice prepared in the study. This lattice constant change is much smaller than those for $3.189-0.077x$ in $Al_xGa_{1-x}N$[10] and $3.189+0.36x$ in $Ga_{1-x}In_xN$.[11] When superlattice is under strain, piezoelectric field proportional to the product of strain and piezoelectric constant is induced. If well layers are strained, electrons and holes confined in well layers will be spatially separated due to internal electric field. In case of ZnO/$Mg_xZn_{1-x}O$ superlattices, the in-plane lattice mismatch is small enough to neglect the internal electric field. Even if there is internal field, the choice of ZnO buffer layer will produce unstrained well ZnO layer and strained $Mg_xZn_{1-x}O$ barrier layer.

Figure 5-7 shows a reciprocal space contour mapping for a superlattice with L_W=12 nm around an asymmetric (10-15) plane of ZnO. Two peaks corresponding to the buffer layer and superlattice were observed. As can be seen, the superlattice and buffer ZnO have an identical q[10-10] value within experimental accuracy. The peak position measured for a thick $Mg_{0.2}Zn_{0.8}O$ layer is marked by a cross as well to show 0.22 % mismatch in the plane. Therefore, in these superlattices, only barrier layers are strained to form pseudomorphic epitaxial structure.

5.3.2. Optical properties

Figure 5-8 shows PL and PLE spectra taken at 4.2 K for the superlattices with L_W=1.7 and 3.1 nm. The PL peak shifts towards higher energy side as L_W decreases. When L_W=5.2 nm, no detectable shift was

observed. The two peaks in the PLE spectra indicated by open and filled triangles are assigned to n=1 quantum sub-band level and barrier layer absorption level, respectively. The positions of the latter peaks shown by filled triangles agree with the absorption edge for a 200 nm-thick $Mg_{0.2}Zn_{0.8}O$ film, indicating that carrier excited at the barrier layers are relaxed into well layers to emit light upon recombination. In order to evaluate the relationship between well layer thickness and observed PLE peak positions for n=1 sub-band level, we have made a preliminary simulation by using reported effective masses of electron (m_e*=0.28) and hole (m_h*=1.8) and considering finite potential barrier. Since the discontinuities at the conduction and valence bands (ΔE_c and ΔE_v) have never been measured, we used the ratio of $\Delta E_c/\Delta E_v$ as a fitting parameter and obtained the best fit when $\Delta E_c/\Delta E_v$=9, that is, ΔE_c=414 meV and ΔE_v=46 meV. The estimated n=1 quantum sub-band level for various well layer thickness is given as a ruler in the figure.

The PL peaks show considerable broadening and Stokes shift by about 50 meV. The former is presumably due to the fluctuation of well layer thickness. As reported earlier,[8] ZnO film surface has spirally shaped steps with a unit cell height (0.52 nm), therefore these superlattices should have well layer thickness fluctuation of $\pm$0.52 nm at minimum. Thickness fluctuations deduced from full width at half maximum of PL peaks, however, are larger than the minimum case. The possible explanations for the peak broadening and Stokes shift could be (1) Mg content fluctuation in the barrier layers, (2) bound state related with unintentionally doped impurities or crystallographic defects, and (3) strain-induced band gap modification of barrier layers. The Mg content of x=0.2 is far above the solubility limit (x=0.04)[12] of bulk solid solution and close to the solubility limit of metastable thin films (x=0.33).[6] Therefore, we suspect reason (1) as most probable. The results for superlattices using x=0.15 barrier layers showed higher crystalline quality, better interface sharpness, and sharper PL peaks with negligibly small Stokes shift.[13] This was much clearly demonstrated by systematic studies using combinatorial laser MBE system as be discussed in chapter 7. Therefore, uniformity of Mg content in the barrier layers significantly affects the optical properties of the $ZnO/Mg_xZn_{1-x}O$ superlattice.

5.4. Conclusions

In summary, we have shown that superlattices composed of oxide widegap semiconductors, ZnO and $Mg_{0.2}Zn_{0.8}O$, were successfully grown by employing ZnO buffer layer. PL and PLE spectra clearly showed quantum size effect. The Mg concentration of x=0.2 is close to the limit to obtain clear electronic structures at the heterointerfaces, probably due to the spatial fluctuation of Mg content in the barrier layer.

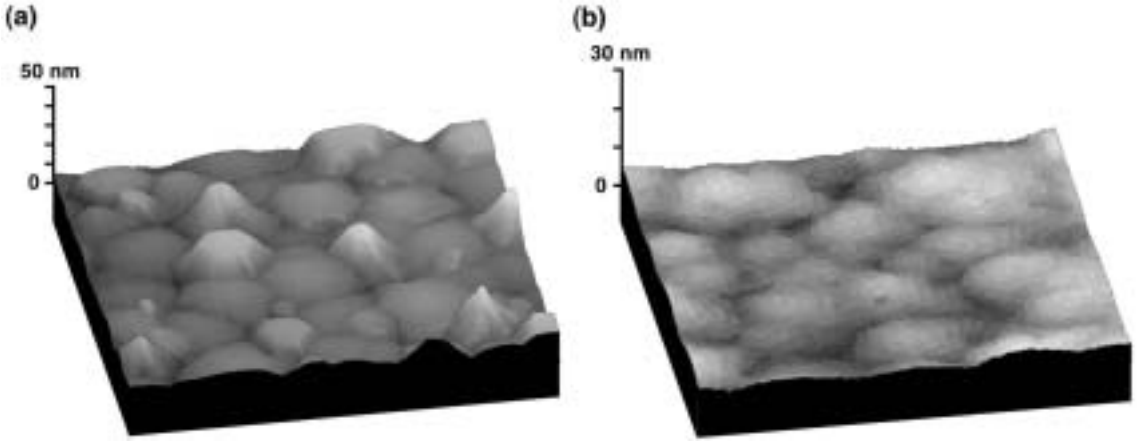

Figure 5-1. Atomic force microscopy images for $Mg_{0.20}Zn_{0.80}O$ films (400 nm-thick) deposited on (a) sapphire substrate and (b) ZnO buffer layer (200 nm-thick).

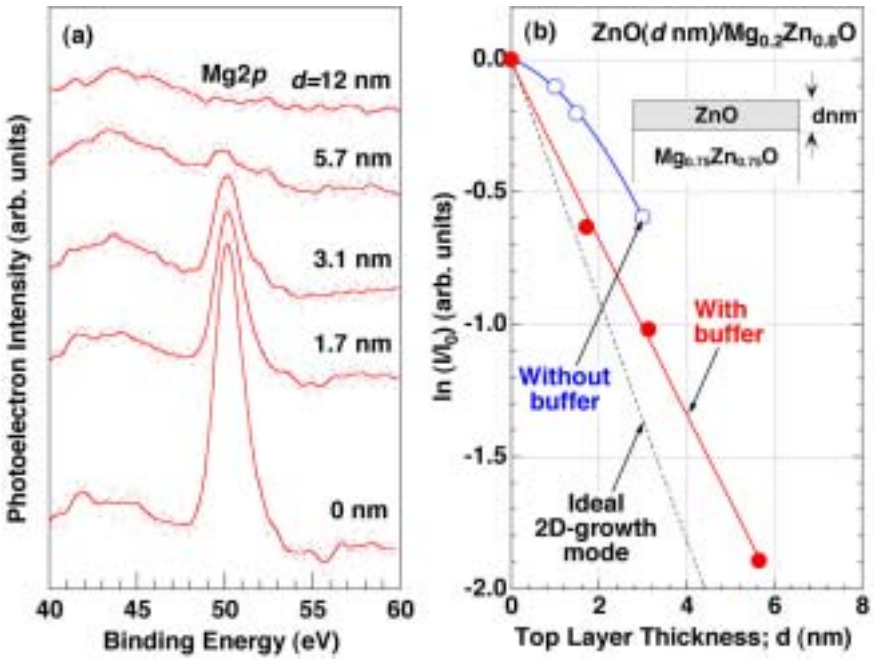

Figure 5-2. (a) X-ray photoelectron spectra of Mg2*p* for ZnO(*d* nm)/$Mg_xZn_{1-x}O$ films grown on sapphire substrate with 100 nm-thick ZnO buffer layer. (b) Integrated intensity of Mg2*p* photoelectron signal as a function of *d* in a natural logarithmic scale. Closed circle is for ZnO/$Mg_xZn_{1-x}O$ with ZnO buffer layer, and open circle is for ZnO/$Mg_xZn_{1-x}O$ without buffer layer grown on sapphire substrates. The dotted line is a simulation curve assuming the ideal two-dimensional growth mode.

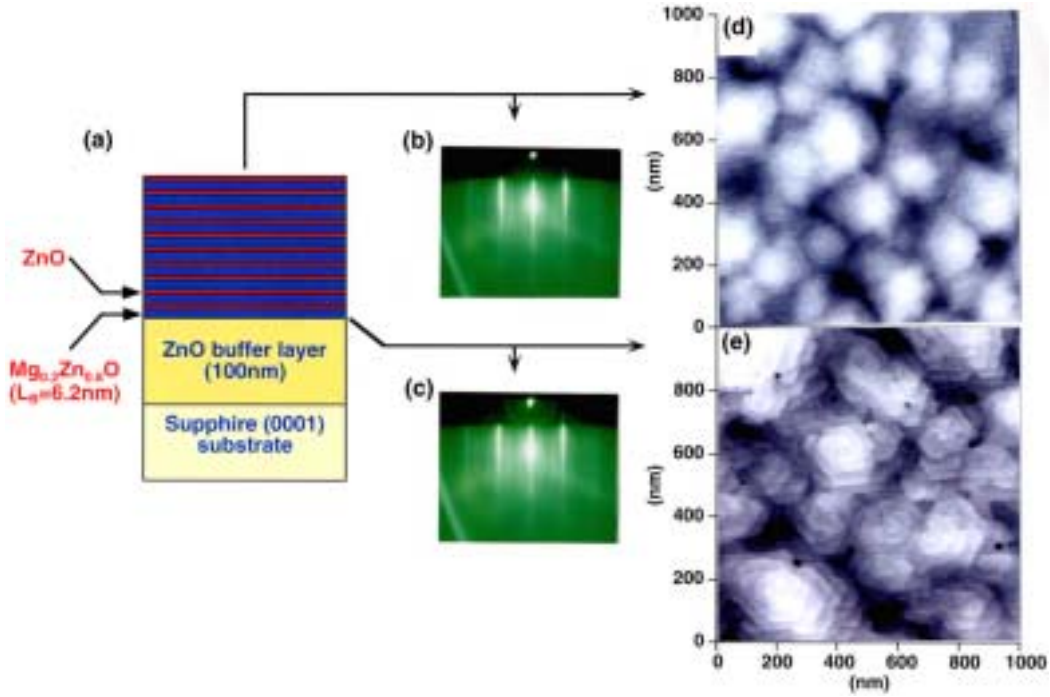

Figure 5-3. (a) Schematic diagram of the ZnO/$Mg_{0.20}Zn_{0.80}O$ superlattice. RHEED pattern of $Mg_{0.20}Zn_{0.80}O$ film grown on a ZnO buffer layer (c) and superlattice grown on it (b) are shown. The incident electron beam is parallel to the [11-20] direction of ZnO. AFM images are also shown for a ZnO buffer layer (e) and a superlattice (d). Steps with a height of 0.52 nm, corresponding to the ZnO *c*-axis length, are clearly seen.

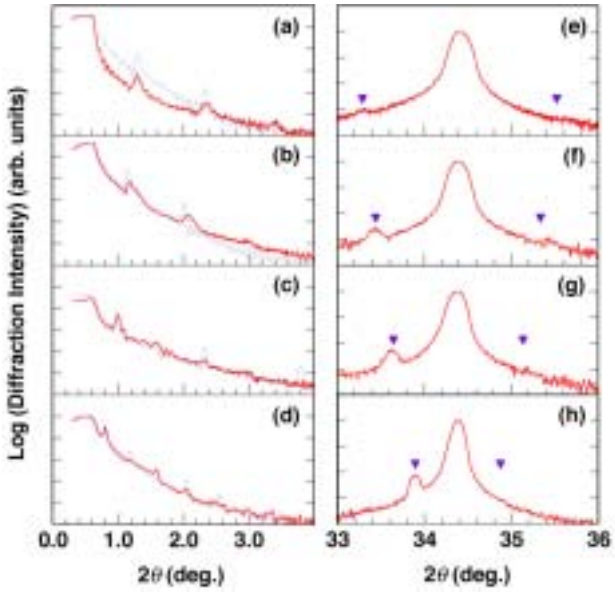

Figure 5-4. ω-2θ XRD pattern of the superlattice samples with ZnO well layer thickness of (a and e) 1.7 nm, (b and f) 3.1 nm, (c and g) 5.7 nm, and (d and h) 12 nm. The solid lines show experimental results. The dotted lines show simulated curves deduced from the designed structure.

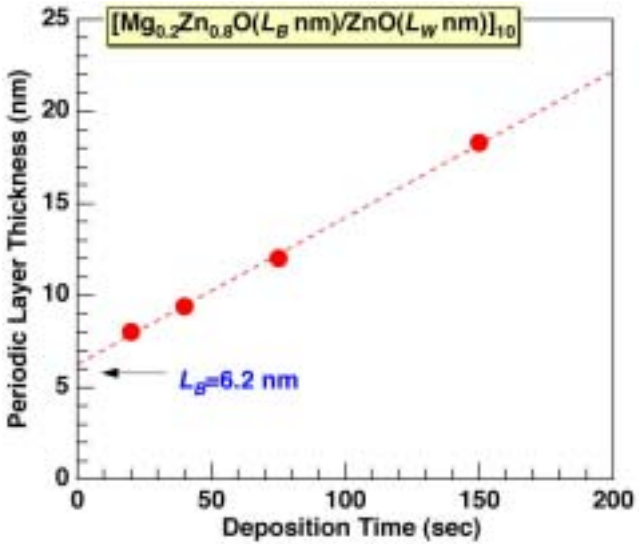

Figure 5-5. The period of superlattices estimated from XRD patterns is plotted as a function of deposition time for the well layer thickness. Barrier thickness was constant at 6.2 nm, while well layer thickness was varied from 1.7 nm to 12 nm.

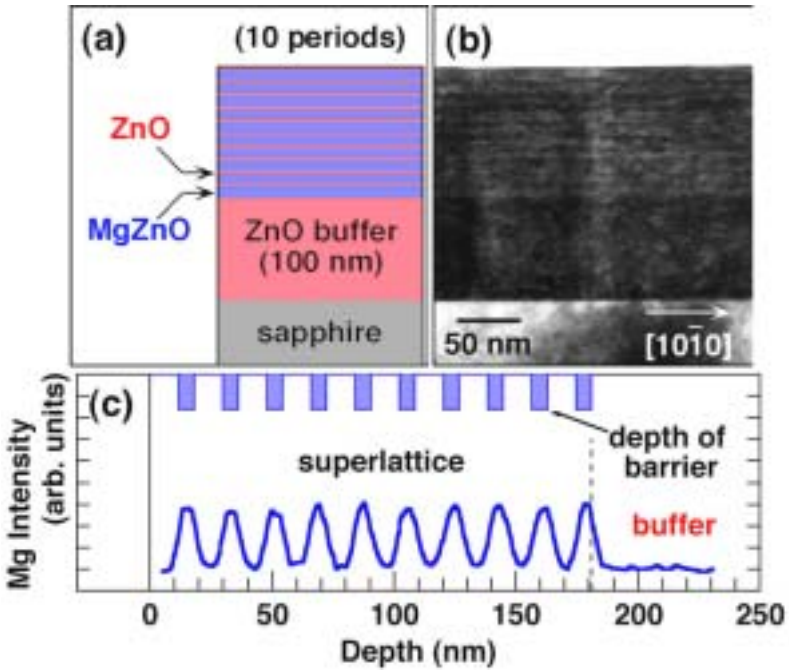

Figure 5-6. Cross-sectional (a) schematic and (b) TEM image of a $ZnO/Mg_{0.2}Zn_{0.8}O$ superlattice with L_W=5.7 nm and L_B=6.2 nm. (c) The depth profile of Mg signal intensity in AES was measured for a superlattice with L_W=12 nm and L_B=6.2 nm.

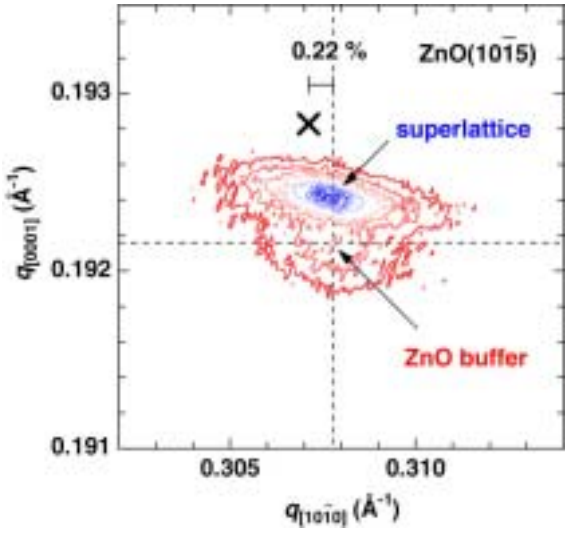

Figure 5-7. X-ray diffraction reciprocal space contour map around (10-15) diffraction for a superlattice sample with L_W =12 nm. The buffer ZnO layer and superlattice have identical q[10-10] value, indicating the barrier $Mg_{0.2}Zn_{0.8}O$ layer is strained to form pseudomorphic epitaxial structure. A cross in the figure is the peak position for a thick $Mg_{0.2}Zn_{0.8}O$ film. The lattice mismatch is as small as 0.22 %.

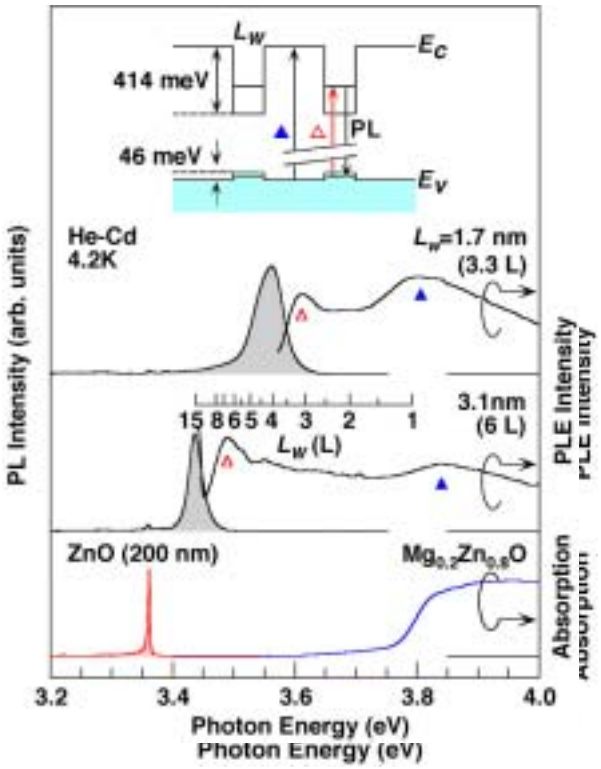

Figure 5-8. PL and PLE spectra measured at 4.2 K for two of the superlattices (L_W =1.7 and 3.2 nm). For comparison, PL and absorption spectra of a 50 nm-thick ZnO film and absorption spectrum of a 200 nm-thick Mg0.2Zn0.8O film are also shown. The ruler in the figure shows calculated quantum sub-band energy as a function of well layer thickness (multiples of unit cell height; LW /0.52 (L)).

References

[1] Y. Segawa, A. Ohtomo, M. Kawasaki, H. Koinuma, Z.K. Tang, P. Yu, and G.K.L. Wong, Phys. Stat. Sol. **B202**, 669 (1997).

[2] Z. K. Tang, P. Yu, G.K.L. Wong, M. Kawasaki, A. Ohtomo, H. Koinuma and Y. Segawa, Solid State Commun. **103**, 459 (1997).

[3] A. Ohtomo, M. Kawasaki, Y. Sakurai, I. Ohkubo, R. Shiroki, Y. Yoshida, T. Yasuda, Y. Segawa, and H. Koinuma, Mat. Sci. Eng. **B54**, 24 (1998).

[4] Z. K. Tang, G.K.L. Wong, P. Yu, M. Kawasaki, A. Ohtomo, H. Koinuma, Y. Segawa, Appl. Phys. Lett. **72**, 3270 (1998).

[5] P. Yu, Z.K. Tang, G.K.L. Wong, M. Kawasaki, A. Ohtomo, H. Koinuma and Y. Segawa, J. Cryst. Growth **184/185**, 601 (1998).

[6] A. Ohtomo, M. Kawasaki, T. Koida, K. Masubuchi, H. Koinuma, Y. Sakurai, Y. Yoshida, T. Yasuda, and Y. Segawa, Appl. Phys. Lett. **72**, 2466 (1998).

[7] T. Honda, A. Inoue, M. Mori, T. Shirasawa, N. Mochida, K. Saotome, T. Sakaguchi, A. Ohtomo, M. Kawasaki, H. Koinuma, F. Koyama, K. Iga, J. Cryst. Growth, **195**, 319 (1998).

[8] A. Ohtomo, M. Kawasaki, T. Koida, K. Masubuchi, H. Koinuma, Y. Sakurai, Y. Yoshida, T. Yasuda, and Y. Segawa, Appl. Phys. Lett. **72**, 2466 (1998).

[9] The simulations were carried out using a commercially available software (Win-Gixa, Philips) based on theoretical models in the literatures, for example, L. G. Parratt, Phys. Rev. **95**, 359 (1954), and D.K. G. de Boer, Phys. Rev. **B44**, 498 (1991).

[10] O. Ambacher, J. Smart, J. R. Shealy, N. G. Weimann, K. Chu, M. Murphy, W. J. Schaff, L. F. Eastman, R. Dimitrov, L. Wittmer, M. Stutzmann, W. Rieger, and J. Hilsenbech, J. Appl. Phys. **85**, 3222 (1999).

[11] L. T. Romano, B. S. Krusor, M. D. McCluskey, D. P. Bour, and K. Nauka, Appl. Phys. Lett. **73**, 1757 (1998).

[12] J. F. Sarver, Fred L. Katnack, and F. A. Hummel, J. Electrochem. Soc. **106**, 960 (1959).

Chapter 6. High-Quality ZnO Films Grown on Lattice-matched $ScAlMgO_4$(0001) Substrates

Abstract

Lattice-matched ($\Delta a/a$=0.09 %) $ScAlMgO_4$(0001) substrates were employed to grow single crystalline quality ZnO films by laser molecular-beam epitaxy. Extremely smooth surface represented by atomically flat terraces and half unit cell (0.26 nm) high steps and extremely small orientation fluctuations both in-plane (<0.02°) and out-of-plane (<0.01°) were achieved. Lattice constants hardly changed with increasing growth temperature, indicating that thermal expansion mismatch is negligibly small. The films have high mobility (~100 cm^2/Vs) together with low residual carrier concentration (~10^{15} cm^{-3}). Excellent optical properties, including a clear doublet of A and B exciton peaks in absorption spectra and sharp photoluminescence line were also observed. The films having thickness above 40 nm showed excitonic stimulated emission with very low threshold at temperatures ranging from 23 to 132° C. Threshold was as small as 19 kW/cm^2, which is the lowest value among the reported threshold of ZnO thin films. Characteristic temperature of excitonic stimulated emission was as high as 107° C. These features could not be simultaneously achieved for ZnO films grown on sapphire (0001) having a large lattice mismatch ($\Delta a/a$=18 %).

6.1. Introduction

As an oxide wide bandgap (E_g=3.37 eV) semiconductor, ZnO has attracted considerable attention for applications such as ultraviolet light emitting devices and laser diodes, due to the observation of very efficient ultraviolet excitonic laser action starting at very low threshold of optical pumping even at room temperature.[1] $Mg_xZn_{1-x}O$ alloys films were readily prepared to extend the bandgap up to about 4.0 eV.[2] $ZnO/Mg_xZn_{1-x}O$ superlattices[3] were demonstrated to confirm the quantum size effect.[4] However, synthesis of *p*-type ZnO still remains the most critical issue and a big challenge. The history of ZnSe and GaN tells us that high quality intrinsic films having high carrier mobility and low residual carrier concentration are the starting point. ZnO thin films grown on lattice mismatched (~18 %) sapphire (0001) substrates are epitaxial but stay multicrystalline in nature having incoherent grain boundaries as was discussed in Chapter 3. Actually, these grain boundaries in epitaxial ZnO thin films seem to be useful for observing excitonic laser action. When the nanocrystal size is tuned to be as small as 50 nm, excitonic lasing is most efficient, making use of these grain boundaries as mirrors of longitudinal cavity. The electronic properties of such films are rather poor as represented by typical electron concentration, n~10^{17} cm^{-3} and Hall mobility μ~10 cm^2/Vs at room temperature, compared to n~10^{15} cm^{-3} and μ~200 cm^2/Vs for bulk single crystals.[5]

One may overcome these problems by using lattice-matched substrates. We have selected hexagonal $ScAlMgO_4$(0001) with lattice constants of a=3.246 Å and c=25.195 Å (Ref. 6) having an in-plane lattice mismatch as small as 0.09 %. $ScAlMgO_4$ is considered to be a natural superlattice composed of alternating stacking layers of wurtzite (0001)-face (Mg, Al)O_x and rocksalt (111)-face ScO_y layers, and hence has a cleavage habit along the (0001) plane. High-quality single-crystals can be grown by the Czochralski method.[7] This substrate is also suitable for the growth of ZnO to characterize optical and electronic properties because of a large band gap of about 5 eV and insulating nature. The crystal structure of $ScAlMgO_4$ and a possible heterointerface with ZnO are schematically shown in Fig. 6-1.

In this chapter, growth of single crystalline ZnO films on lattice-matched $ScAlMgO_4$ (0001) substrates and demonstration of excellent structural, electric, and optical properties, which would serve as host crystal films for possible *p*-type doping, are discussed.

6.2. Experimental

ZnO thin films were grown on $ScAlMgO_4$ (0001) and sapphire (0001) substrates by laser molecular-beam epitaxy that has been widely applied to the growth of high quality oxide thin films under high vacuum conditions.[8] KrF excimer laser pulses were directed onto a ZnO ceramic target (99.999 %) located 5 cm away from the substrate surface. The films were grown at temperatures ranging from 350° C

to 1000° C in 1×10^{-5} Torr of pure oxygen (99.9999 %). The surface morphology of the substrates and films was imaged by contact-mode atomic force microscope (AFM). The crystallinity of the films was characterized by a high resolution x-ray diffraction (XRD) apparatus equipped with a four-crystal monochrometer and an analyzer crystal with resolutions of 0.005° and 0.008°, respectively. The electronic properties of the films were characterized at room temperature by Hall measurements (van der Pauw configuration) with indium ohmic electrodes. The optical properties were characterized by photoluminescence (PL) spectroscopy using a cw He-Cd laser (325 nm) at 4.2 K and by absorption spectroscopy at 6 K. Frequency tripled pulses (355 nm, 10 Hz, 15ps) from a mode-locked Q-switch Nd: YAG laser (Coherent) was used for lasing experiments at temperature ranging from 294 to 380 K. The laser beam was focused with a cylindrical lens into a stripe on the sample surface at normal incidence. Emission spectra were taken from side edge of the samples by a monochrometer equipped with a cooled CCD detector.

6.3. Results and Discussions

6.3.1. Surface morphologies

Figure 6-2 shows AFM images for three kinds of substrates used in this study, *i.e.*, as-polished sapphire (0001), as-polished, and cleaved $ScAlMgO_4$ (0001), and those of the ZnO films grown on the respective substrates at 1000° C. Here, we note that the as-polished $ScAlMgO_4$ surface has atomically flat terraces and 0.85 nm-high steps, parallel in one direction (Fig. 6-2 (c)). This step height corresponds to one third of the *c*-axis length of $ScAlMgO_4$, *i.e.*, a pair of wurtzite $(MgAl)O_x$ and rocksalt ScO_y layers as schematically shown in Fig. 6-1. We presume that the appearance of such a well-defined surface structure is due to selective etching of one of the constituting layers during polishing in a solution, as in the case of $SrTiO_3$ (100) etched in a weak acid.[9] The miscut angle of this particular substrate was deduced as 0.14° by taking into account the ratio of the step height to the average terrace width of 340 nm. When the substrate is cleaved along the (0001) plane, the surface shows a step-free and atomically flat area of about 100 μm in size. Apparently, bunched steps seen by an optical microscope could be located in an AFM image as shown in Fig. 6-2 (e).

As can be clearly seen in Fig. 6-2 (d) and (f), ZnO thin films grown on $ScAlMgO_4$ have very flat surfaces as represented by atomically flat terraces and an 0.26 nm-high step (a charge neutral unit of ZnO). On the other hand, the film grown on sapphire (Fig. 6-2 (b)) shows a much rougher surface than those on $ScAlMgO_4$, by two orders of magnitude. On the film grown on an as-polished substrate (d), many steps are aligned in one direction, suggesting step-flow growth mode. The tilting angle of the film surface from the (0001) basal plane was calculated to be 0.17°, which agrees with the miscut angle of the

substrate within statistical error. On the cleaved substrates, the film grows in a two dimensional growth mode with a random nucleation, resulting in coaxially aligned and round shaped steps (f).

6.3.2. Growth temperature dependence of crystallinity

The crystallinity is also drastically improved by using $ScAlMgO_4$ substrates. All the films grown on $ScAlMgO_4$ substrates showed an epitaxial relationship of ZnO(0001)//$ScAlMgO_4$ (0001) and ZnO [11-20]//$ScAlMgO_4$ [11-20] without any trace of the other in-plane orientation domains which were observed for ZnO/sapphire(0001)[10] (twisting by 30°) and GaN/$ScAlMgO_4$[7] (twisting by 0.4°). Figure 6-3 (a) shows reciprocal space mapping of ZnO (11-24) peaks for a commercial bulk single crystal (Litton Airtron Co., Ltd.) and the films grown on $ScAlMgO_4$ and sapphire substrates at 1000° C. Obviously, the diffraction peak of ZnO/$ScAlMgO_4$ is much sharper than that of ZnO/sapphire and has almost the same quality as that of the single crystal. The peak position shift of the films can be interpreted as due to the strain induced by the thermal expansion mismatch as be described later. The fluctuation of crystal orientation, *i.e.*, in-plane *twisting* ($\Delta\phi$) and out-of-plane *tilting* ($\Delta\omega$) as represented by the full width at half maximum (FWHM) of the (10-11) and (0002) rocking curves, are plotted as a function of growth temperature (T_g) in Fig. 6-3 (b) and (c). The values of $\Delta\phi$ and $\Delta\omega$ for ZnO/$ScAlMgO_4$ grown above 450° C are temperature-independent and less than 0.02° and 0.01°, respectively, while a slight increase in the out-of-plane $\Delta\omega$ was detected only for the sample grown at 350° C. When ZnO films were grown on sapphire, much larger $\Delta\phi$ and $\Delta\omega$ values were observed in the full temperature range. As T_g was increased, $\Delta\phi$ and $\Delta\omega$ decreased, but still remained larger than 0.09° and 0.04°, respectively. Therefore, we conclude that ZnO thin films having comparable crystallinity to that of the bulk crystal can be grown even at a temperature as low as 400° C.

In the growth direction of wurtzite (0001), biaxial strain due to thermal expansion mismatch as well as lattice mismatch induces built-in piezoelectric field along the growth direction. *a*- and *c*-axis length of ZnO films grown on sapphire and $ScAlMgO_4$ is plotted as a function of growth temperature (T_g) in Fig. 6-4. In case of ZnO/sapphire, *c*-axis length increases while, *a*-axis length decreases with increasing T_g, indicating compressive strain. This agrees with the fact that there is a negative mismatch between linear thermal expansion coefficients parallel to the *a*-axis direction of 5.5×10^{-6} K^{-1} for ZnO and 7.3×10^{-6} K^{-1} for sapphire.[11] As for ZnO/$ScAlMgO_4$, the lattice constants are very close to the values for the bulk crystal at entire temperature range. This means thermal expansion mismatch is negligibly small in this system. Slight residual compressive strain would be caused by lattice mismatch because the measured *a*-axis length is rather close to that of $ScAlMgO_4$.

6.3.3. Electronic properties

The electronic properties of undoped films grown on various substrates were investigated by Hall measurements and summarized in Fig. 6-5. ZnO films grown on $ScAlMgO_4$ clearly showed both high μ (60~100 cm^2/Vs) and low n ($0.4\sim2.7 \times 10^{16}$ cm^{-3}) when compared to the films grown on sapphire. We did not observe any considerable dependence of n and μ on T_g. In the case of ZnO/sapphire, the residual carrier concentration was as large as 10^{18} cm^{-3}. After these films were annealed at 1000° C in 1 atm of oxygen to decrease grain boundary density, the values of μ increased, while the values of n showed no considerable change.[11] Therefore, it is concluded that the use of $ScAlMgO_4$ substrate is essential not only for improving the electron mobility, *i.e.*, reducing crystalline defects, but also for reducing the residual carrier concentration. We have examined the doping capability of these high crystalline thin films by preparing n^{++}-type ZnO doped with Al by using 0.5 % Al_2O_3 mixed ceramic target. These films showed high conductivity (>10^3 Scm^{-1}) and high crystallinity ($\Delta\phi$ and $\Delta\omega$ less than 0.05°). The doped films grown on sapphire substrates can not achieve both requirements simultaneously because a higher growth temperature is needed to obtain a higher crystallinity whereas lower temperature is needed to prevent segregation of Al_2O_3 and related compounds at grain boundaries.

6.3.4. Optical properties: fine excitonic structure and stimulated emissions

We have also examined the optical properties of some of the films. Here, we have selected the films grown at 600° C, which is the typical deposition condition for observing the most efficient lasing.[12] Absorption spectra taken at 6 K for 50 nm-thick films on $ScAlMgO_4$ showed a clear doublet in the exciton absorption peak, which can be assigned to A and B excitons separated by 7.0 meV, as shown in Fig. 6-6 (a). This splitting has not been observed so far for the films grown on sapphire (b) because of the large nonradiative damping-constant of excitons due to poor crystallinity, and also not for high quality bulk single crystals because of the large thickness. Those excellent optical properties enable us to estimate each excitonic parameter directly from the absorption spectra.[13] The ZnO films grown on $ScAlMgO_4$ substrates give narrower PL line width of a donor-bound exciton emission (I_6)[14] than that of the film grown on sapphire. Emission peak is observed at 3.364 eV and 3.361 eV for the films grown on sapphire and $ScAlMgO_4$ substrates, respectively.

6.3.5. Room temperature stimulated emission at very low threshold

We also characterized optical properties under a strong excitation condition. In order to perform the systematic experiments, the films grown by combinatorial laser MBE system, whose details are described

in chapter 7, are tested. Briefly, the films having 3×3 mm^2 in size were deposited on 16×16 mm^2 $ScAlMgO_3$ wafers (as-cleaved) through physical masks, in which nine pixels are defined as 3×3 manner. 36 samples (4 chips) having various thickness ranging from 9.4 to 269 nm were grown at 600° C in an oxygen pressure of 1×10^5 Torr. Layer thickness was precisely determined from Laue-fringe spacing in the x-ray diffraction patterns. The surface was observed by a mean of AFM and was confirmed to be atomically flat, as represented similar morphologies to that shown in Fig. 6-2 (f).

Figure 6-7 (a) shows layer thickness dependence of the stimulated emission threshold for the films grown on $ScAlMgO_4$ substrates (closed circles) and lasing threshold for the films grown on sapphire substrates reported in Ref. 15. The growth conditions of the films grown on sapphire substrates is quite similar to that used in this study. The samples grown on $ScAlMgO_4$ substrates exhibit considerably lower threshold than that of films grown on sapphire, even though two times larger excitation intensity should be needed for lasing compared to stimulated emission.[16] The lowest threshold (19 kW/cm^2) was observed for the 186 nm-thick film, and this value is still lower than the lowest one observed in ZnO/sapphire. This result would be attributed to much higher crystallinity of ZnO/$ScAlMgO_4$, as represented by about 0.05 times smaller FWHM values of ZnO (0002) rocking curves for the ZnO/$ScAlMgO_4$ with comparing ZnO/sapphire. The dependence for the ZnO/$ScAlMgO_4$ is reproduced in Fig. 6-7 (b) with larger magnification for the horizontal axis. Rapid increasing of the threshold below 50 nm and a minimum threshold at thickness ranging 50-150 nm can be seen from both cases. This dependence has been explained by taking a theory based on waveguide effect into account.[15] Since epitaxial layer can be considered as a thin dielectric waveguide, any mode can not be allowed to exist in the guide when thickness is below a cutoff value (L_{cutoff}). In case of ZnO/sapphire, L_{cutoff} is estimated to be 29 nm, which is denoted by dashed lines in the figures. Refractive index of $ScAlMgO_4$ is reported to be similar to that of sapphire[7], so that similar cutoff value can be expected for ZnO/$ScAlMgO_4$. When layer thickness is larger than L_{cutoff} but sufficiently thinner, only the lowest-order *TE* guided mode exists, resulting that a large fraction of the total spontaneous emission goes into the TE_0 mode. This leads to an increase in the stimulated emission and hence gain. Further investigation would be interesting to understand lasing mechanism due excitonic recombination process.

Emission energy position also depends on the layer thickness as shown in Fig. 6-7 (c). As layer thickness increases, emission energy increases. Although this behavior has not been understood yet, there are interesting finding. Some of the samples having thickness below 100 nm start to show stimulated emission at higher energy position than that of *P*-line, which is stimulated emission mode due to *ex-ex* collision process. For instance, the first stimulated emission line starts to increase at 3.25 eV for 81 nm-thick film (denoted by an arrow) as shown in the inset of Fig. 6-7 (c). For a comparison, energy

positions of various emission modes such as free exciton spontaneous emission (E_{ex}), spontaneous and stimulated emissions (P_2 and P) due to exciton-exciton collision process, and electron-hole plasma (EHP), which have been observed in ZnO nanocrystalline films grown on sapphire,[17] is given in the figures. One of the possible reasons for *ultraviole*t-shift of the stimulated emission peak might be a quantum confinement effect of excitons in a two-dimensional system.[18]

In order to examine applicability to real device, we tested to high-temperature operation at a temperature ranging from 23 to 132° C. Figure 6-8 shows temperature dependence of emission intensity as a function of excitation intensity (I_{ex}) of a 61 nm-thick ZnO/$ScAlMgO_4$ with thickness of 61 nm. The threshold for the stimulated emission increased gradually with increasing temperature. The inset shows temperature dependence of ln(I_{th}). The characteristic temperature, which was used to express the temperature dependence of the threshold in the formula $I_{th}(T)=I_0\exp(T/T_0)$, was estimated to be 107 K for ZnO/$ScAlMgO_4$. Here, I_o is a constant, T is the absolute temperature, $I_{th}(T)$ is the threshold. For a comparison, that for 55 nm-thick ZnO/sapphire showing excitonic lasing with the lowest threshold (40 kW/cm^2)[19] is also plotted in the figure. T_0 for this sample is calculated to be 67 K. We attribute larger T_0 for ZnO/$ScAlMgO_4$ to high crystalline quality.

6.4. Conclusions

In conclusion, the application of $ScAlMgO_4$(0001) substrates has substantially improved the crystalline quality of epitaxial ZnO thin films. We note a high surface smoothness, high crystallinity, excellent electronic properties such as low residual carrier concentration (~10^{15} cm^{-3}) and high electron mobility (~100 cm^2/Vs), a small damping constant of excitons observed in absorption spectra, and efficient *n*-type doping. Very low threshold (19 kW/cm^2) and high characteristic temperature (107 K) for excitonic stimulated emission was demonstrated under strong excitation condition using Nd: YAG laser pulses. These excellent properties were achieved by small lattice mismatch (0.09 %) and by small thermal expansion mismatch.

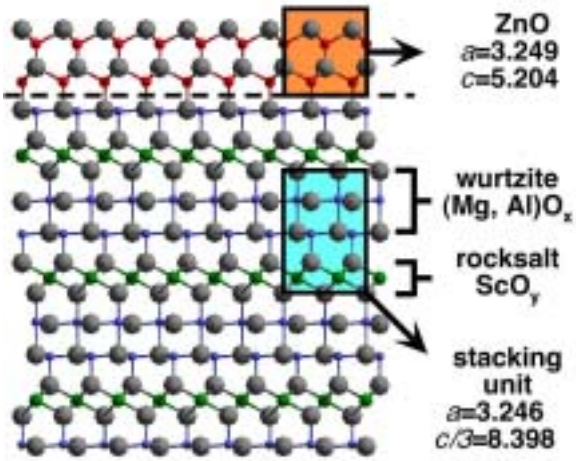

Figure 6-1. Schematic illustration of $ScAlMgO_4$ crystal structure composed of an alternating stack of wurtzite (Mg, Al)O_x (0001) and rocksalt ScO_y (111) layers. Epitaxially grown ZnO is attached by assuming that the wurtzite layer of $ScAlMgO_4$ coherently continues with that of ZnO.

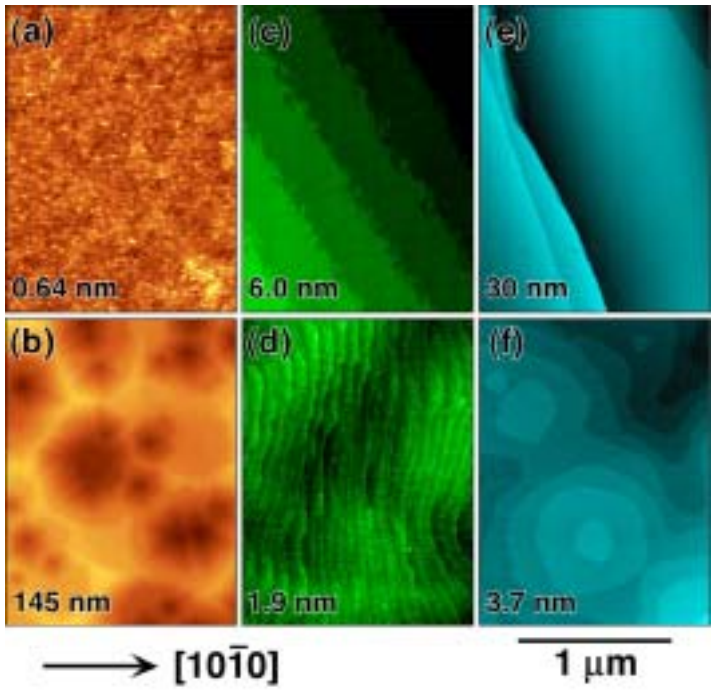

Figure 6-2. Atomic force microscope images of various substrates and the films deposited on them. (a) and (b): as-polished sapphire (0001). (c) and (d): as-polished $ScAlMgO_4$ (0001). (e) and (f): cleaved $ScAlMgO_4$ (0001). Films were 1.5 μm thick grown at 1000° C. The step height in (c) is 0.85 nm, and that in both (d) and (f) is 0.26 nm, corresponding to charge neutral units of $ScAlMgO_4$ and ZnO, respectively. The span of gray scale in the topographic image is given in the respective left-bottom corner.

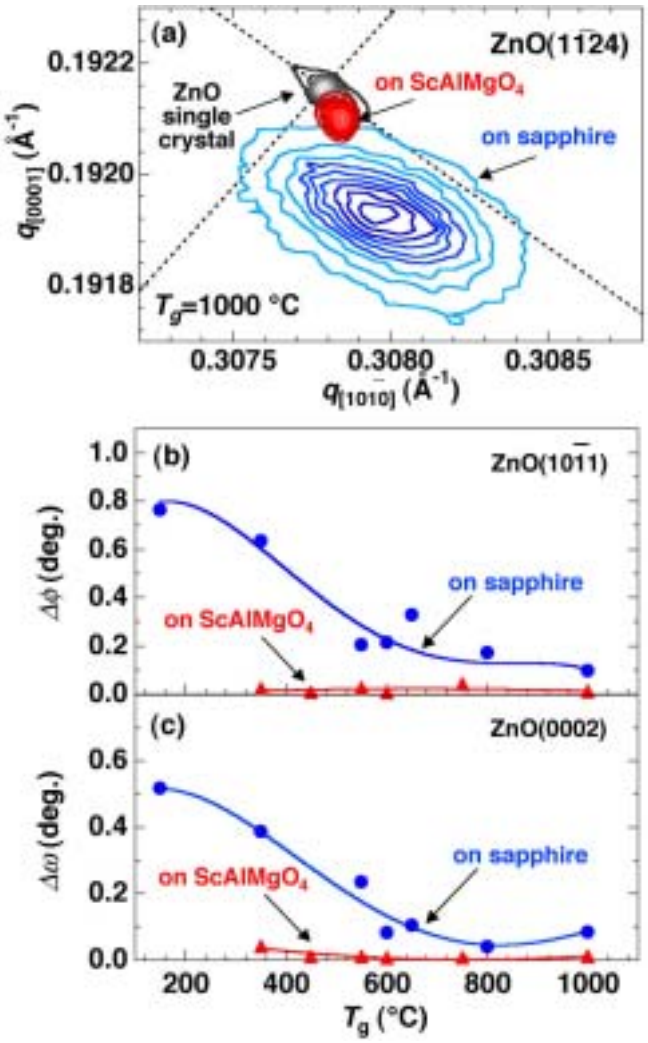

Figure 6-3. (a) Reciprocal space contour mapping of ZnO (11-24) peaks for a bulk ZnO single crystal and the films grown on sapphire and $ScAlMgO_4$ at 1000° C. Broken lines are eye guides for the directions of the Bragg and *tilting* diffraction. (b) and (c) Growth temperature dependence of the full width at half maximum ($\Delta\phi$ and $\Delta\omega$), for in-plane and out-of-plane rocking curves measured for ZnO films grown on sapphire (○) and $ScAlMgO_4$ substrates (▲).

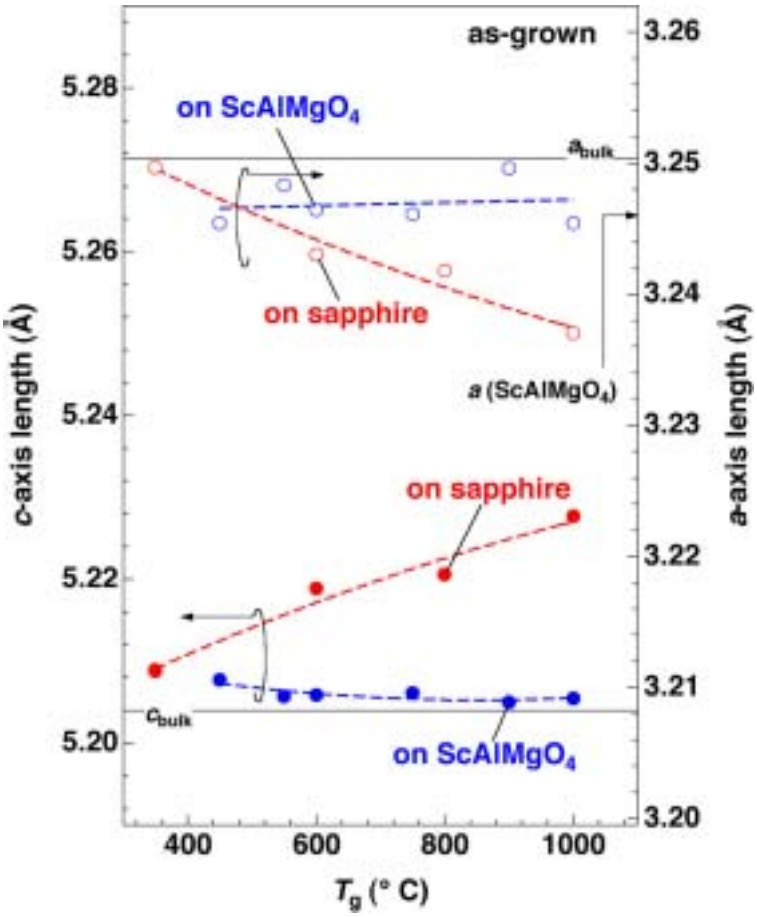

Figure 6-4. Growth temperature dependence of the *a*- and *c*-axis length of 1 μm-thick ZnO films grown on sapphire and $ScAlMgO_4$ (0001) substrates. *a*-axis length of the films grown on $ScAlMgO_4$(0001) substrates was precisely determined from reciprocal space mapping including ZnO (10-14) and $ScAlMgO_4$ (10-11$\underline{9}$). The lattice parameters of the bulk crystal are indicated by the solid lines, and the *a*-axis lattice parameter of $ScAlMgO_4$ is given by the arrow.

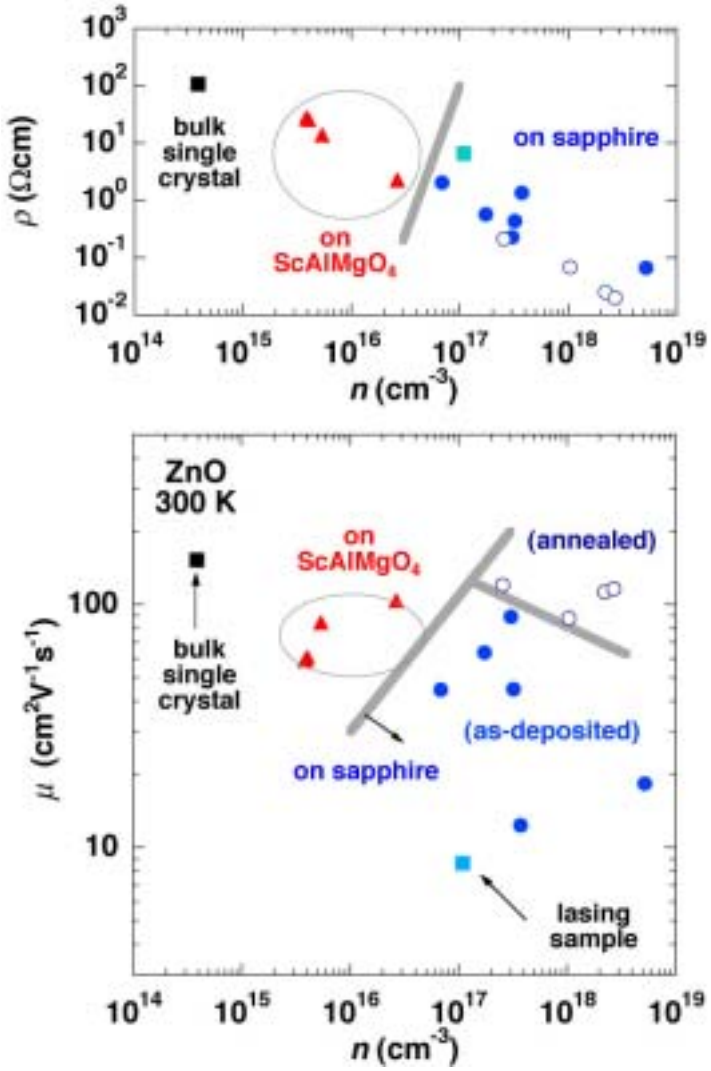

Figure 6-5. Electronic properties of various undoped ZnO films and a bulk single crystal are mapped out in a plane of (a) carrier concentration (n) and resistivity, and (b) n and electron mobility (μ). Gray lines and circles show the boundaries classifying as-deposited ZnO/sapphire (●), ZnO/sapphire annealed at 1000° C in 1 atm of O_2 (○), and as-deposited ZnO/$ScAlMgO_4$ (▲).

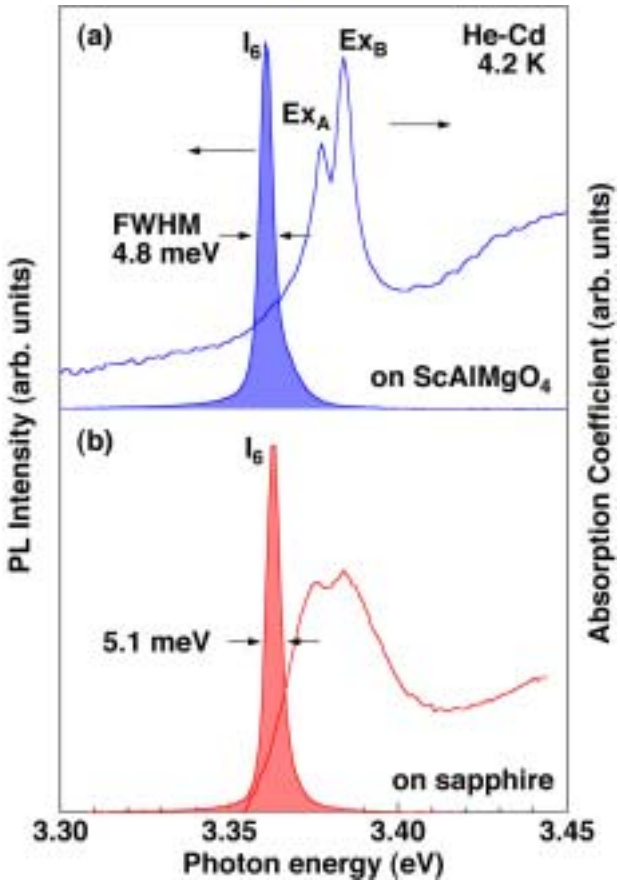

Figure 6-6. Photoluminescence spectra measured at 4.2 K and absorption spectra taken at 6 K (a) ZnO/$ScAlMgO_4$ and (b) ZnO/sapphire. Growth temperature and film thickness is 600° C and about 50 nm for both films, respectively.

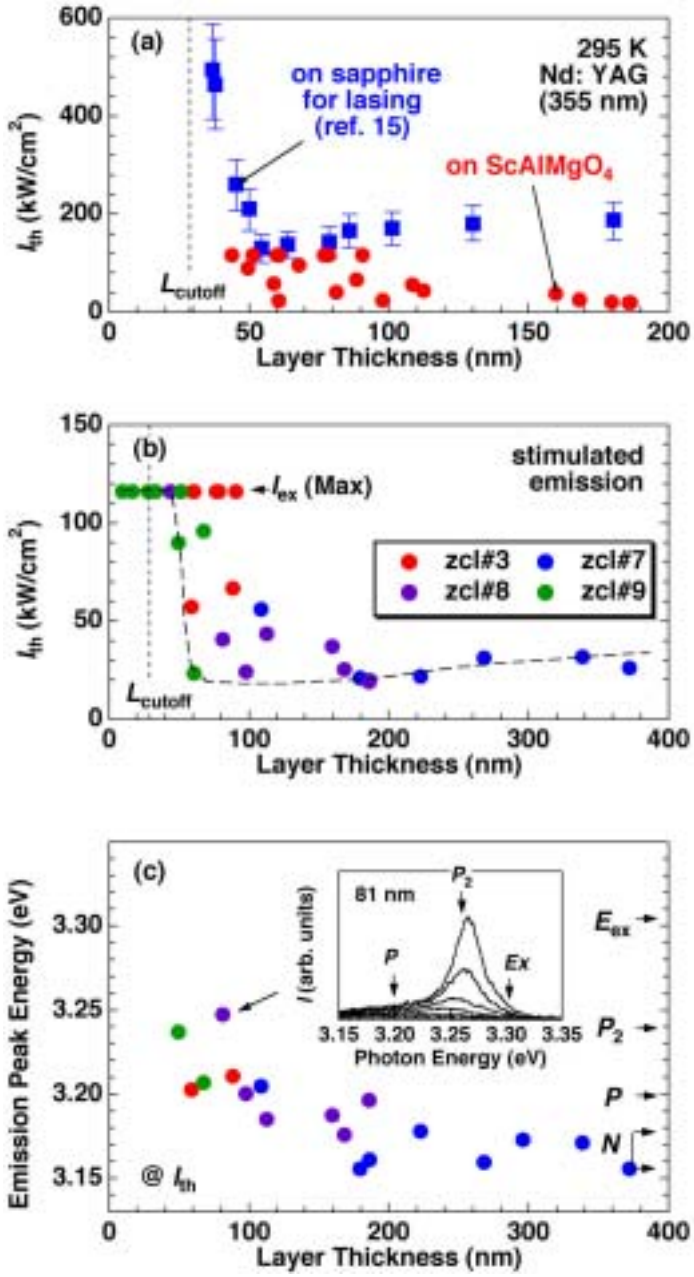

Figure 6-7. (a) Threshold of the stimulated emissions for the ZnO films, grown on $ScAlMgO_4$ at 600° C using combinatorial laser MBE (See section 7.2.1.), as a function of layer thickness compared with that for the ZnO films grown on sapphire. L_{cutoff} indicates a cutoff value calculated by a theoretical model with considering waveguide effect. (b) Similar to (a), but different magnification. (c) The emission peak energy at the threshold as a function of layer thickness of ZnO grown on $ScAlMgO_4$ at 600° C using combinatorial laser MBE.

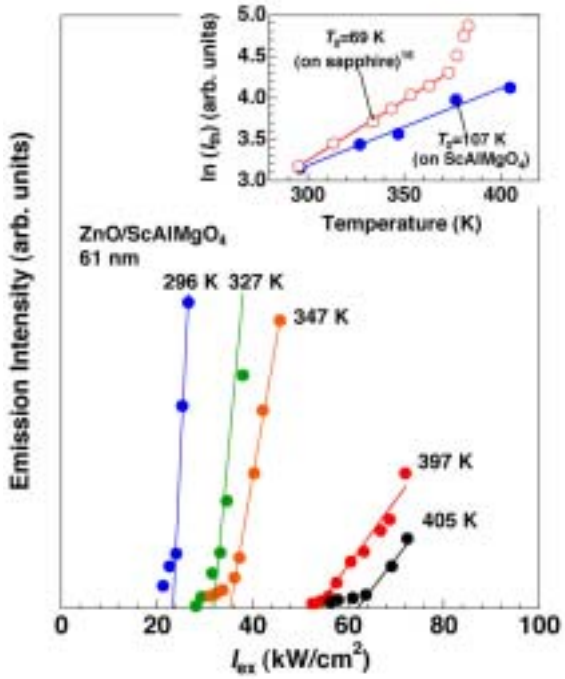

Figure 6-8. Temperature dependence of the emission intensity as a function of excitation intensity (I_{ex}) of 61 nm-thick ZnO film grown on the $ScAlMgO_4$ substrate. Inset depicts threshold intensity (I_{th}) of the same sample as a function of temperature. Characteristic temperature (T_0) is as high as 107 K. For a comparison, that of 55 nm-thick ZnO film are also shown in the inset figure.

References

[1] See for example, a review, M. Kawasaki, A. Ohtomo, I. Ohkubo, H. Koinuma, Z. K. Tang, P. Yu, G.K.L. Wong, B.P. Zhang, and Y. Segawa, Mat. Sci. Eng. **B56**, 239 (1998).

[2] A. Ohtomo, M. Kawasaki, T. Koida, K. Masubuchi, H. Koinuma, Y. Sakurai, Y. Yoshida, T. Yasuda, and Y. Segawa, Appl. Phys. Lett. **72**, 2466 (1998).

[3] A. Ohtomo, M. Kawasaki, Y. Sakurai, I. Ohkubo, R. Shiroki, Y. Yoshida, T. Yasuda, Y. Segawa, and H. Koinuma, Mat. Sci. Eng. **B56**, 263 (1998).

[4] A. Ohtomo, M. Kawasaki, I. Ohkubo, H. Koinuma, T. Yasuda, and Y. Segawa, Appl. Phys. Lett. **75**, 980 (1999).

[5] K. J. Hagemark, and L. C. Chacka, J. Solid State Chem. **15**, 261 (1975).

[6] Accurate lattice constants of $ScAlMgO_4$ measured in this study were a=3.249 Å and c=25.195 Å. Other values of a=3.2405 Å and c=25.106 Å, and a=3.236 Å and c=25.150 Å are reported in Ref. 7 and N. Kimuzuka and T. Mohri, J. Solid State Chem. **78**, 98 (1989), respectively.

[7] E. S. Hellman, C. D. Brandle, L. F. Schneemeyer, D. Wiesmann, I. Brener, T. Siegrist, G. W. Berkstresser, D. N. E. Buchanan, E. H. Hartford, Jr., Mat. Res. Soc. Symp. Proc. **395**, 51 (1996).

[8] H. Koinuma, M. Kawasaki, and M. Yoshimoto, Mat. Res. Soc. Symp. Proc. **474**, 303 (1997).

[9] M. Kawasaki, K. Takahashi, T. Maeda, R. Ryuta, M. Shinohara, O. Ishiyama, T. Yonezawa, M. Yoshimoto, and H. Koinuma, Science **266**, 1540 (1994).

[10] R. D. Vispute, V. Talyansky, Z. Trajanovic, S. Choopun, M. Downes, R. P. Sharma, T. Venkatesan, M. C. Woods, R. T. Lareau, K. A. Jones, and A. A. Iliadis, Appl. Phys. Lett. **70**, 2735 (1997).

[11] D. N. Nikogosyan, in *Properties of Optical and Laser-Related Materials*, edited by D. N. Nikogosyan (John Wiley & Sons Ltd., England, 1997).

[12] A. Ohtomo, M. Kawasaki, Y. Sakurai, I. Ohkubo, R. Shiroki, Y. Yoshida, T. Yasuda, Y. Segawa, and H. Koinuma, Mat. Sci. Eng. **B54**, 24 (1998).

[13] T. Makino, N. T. Tuan, Y. Segawa, C.H. Chia, M. Kawasaki, A. Ohtomo, K. Tamura, and H. Koinuma, submitted to Appl. Phys. Lett.

[14] D. C. Reynolds, D. C. Look, B. Jogai, C. W. Litton, T. C. Collins, W. Harsch, and G. Cantwell, Phys Rev. **B57**, 12151 (1998).

[15] P. Yu, Z.K. Tang, G.K.L. Wong, M. Kawasaki, A. Ohtomo, H. Koinuma and Y. Segawa, J. Cryst. Growth **184/185**, 601 (1998).

[16] Z.K. Tang, P. Yu, G.K.L. Wong, M. Kawasaki, A. Ohtomo, H. Koinuma, and Y. Segawa, Nonlinear Optics **18**, 355 (1997).

[17] Z. K. Tang, P. Yu, G.K.L. Wong, M. Kawasaki, A. Ohtomo, H. Koinuma and Y. Segawa, Solid State Commun. **103**, 459 (1997).

[18] Z.K. Tang, Y. Yanase, T. Yasui, Y. Segawa and K. Cho, Phys Rev. Lett., **71** (1993) 1431.

[19] Z. K. Tang, G.K.L. Wong, P. Yu, M. Kawasaki, A. Ohtomo, H. Koinuma, Y. Segawa, Appl. Phys. Lett. **72**, 3270 (1998).

Chapter 7. High Throughput Optimizations of Alloy and Doped Films Based on ZnO and Parallel Synthesis of ZnO/$Mg_xZn_{1-x}O$ Quantum Wells Using Combinatorial Laser MBE

Abstract

We report high-throughput optimizations for various material parameters of $Mg_xZn_{1-x}O$ and $Zn_{1-x}Cd_xO$ alloy films, Al-doped ZnO films, $Mg_xZn_{1-x}O$/ZnO single quantum wells and superlattice structures with using combinatorial laser MBE (CL-MBE). Combinatorial chips including nine thin film pixels were grown on lattice-matched $ScAlMgO_4$ (0001) substrates by switching the mask patterns and targets during pulsed laser deposition. For alloy experiments, two chips (two runs) provided us with complete and systematic understanding of the band gap in a range from 3.0 to 3.6 eV. An Al-doped chip revealed systematic variation of the conductivity from 3 to 2×10^3 Scm^{-1}. A single quantum well chip showed clear systematic variation of photoluminescence peak energy as a function of well layer thickness. Two superlattice chips showed clear systematics on the quantum sub-band levels in absorption spectra even at room temperature, giving all desired information being useful for designing an efficient active layer in possible ultraviolet light emitting devices. The excitonic stimulated emissions could be observed even at very low optical pumping at room temperature. The threshold excitation intensity changed in a range of 11~40 kW/cm^2 and the emission energy can be tuned between 3.2 and 3.4 eV, depending on the well layer thickness and/or the Mg content in the barrier layers. The excitonic stimulated emission could be observed up to 100° C and a characteristic temperature was as high as 87 K for the best sample optimized by the combinatorial approach using only 8 deposition runs carried out in a week.

7.1. Introduction

As an oxide wide bandgap (E_g=3.37 eV) semiconductor, ZnO has attracted considerable attention for the applications such as ultraviolet light emitting devices (LEDs) and laser diodes (LDs). We have demonstrated room temperature laser action upon optical pumping form ZnO thin films grown on sapphire substrate by laser molecular beam epitaxy[1] (L-MBE). ZnO thin films are composed of hexagonally shaped nanocrystals closely assembled in a honeycomb fashion.[2] The stimulated emission process was caused by exciton-exciton collision even at room temperature because of the very large exciton binding energy (60 meV).[3] The threshold of this excitonic process was very low (24 kW/cm^2: still the best up to now) when the nanocrystalline size was tuned at about 50 nm. The longitudinal cavity was automatically formed by making use of the grain boundaries between hexagonal nanocrystals acting as mirrors.[4,5] These observations triggered us to start intensive study for constructing current-injection devices.

We have focused our effort to achieve two important requirements for realizing actual devices; these are valence control of ZnO to produce *p*-type material and band gap engineering. If band gap engineering is possible to form quantum well structure, much higher emission efficiency can be expected.[6] We have succeeded to prepare $Mg_xZn_{1-x}O$[7] and $Zn_{1-x}Cd_xO$[8] alloy films having x far above the thermodynamic solubility limits by using pulsed laser deposition (PLD). ZnO/$Mg_xZn_{1-x}O$ superlattices were consequently fabricated[9] to demonstrate quantum size effects.[10] In order to improve the crystalline quality, we have employed lattice-matched oxide $ScAlMgO_4$(0001) substrates instead of sapphire (0001) to improve the crystalline quality.[11] Excellent semiconductor properties of the films in terms of surface flatness, crystallinity, electronic and optical properties could be achieved with comparison to those of the films grown on sapphire. The most important achievement is that high crystalline films can now be grown even at a temperature as low as 400 ° C, providing us the opportunity to form *p*-type ZnO.[12]

For designing the semiconductor device architecture based on ZnO, systematic studies of electric and optical properties are necessary to optimize various material parameters in terms of alloying and doping, and heterostructures with well-defined epitaxial heterointerfaces. These are generally time-consuming experiments without utilizing combinatorial approach. In this paper, we discuss high-throughput optimization of $Mg_xZn_{1-x}O$ and $Zn_{1-x}Cd_xO$ alloy films, Al-doped ZnO films, ZnO/$Mg_xZn_{1-x}O$ single quantum wells (SQWs) and superlattices structures by using combinatorial laser molecular-beam epitaxy (CL-MBE) method.

7.2. Experimental

7.2.1. CL-MBE growth of ZnO based alloy and doped films

We used originally designed CL-MBE system, whose details are described elsewhere[13,14] Briefly, various films having 3×3 mm^2 in size were deposited on 16×16 mm^2 substrates through combinatorial masks in which nine pixels are defined as 3×3 manner with a spacing of 1 mm between each pixel. By switching the mask patterns and targets during pulsed laser deposition (PLD), nine different films having various thickness, composition, and layered structure were grown.

Various combinatorial chips fabricated in this study are listed in Table 8-1 as functions of the materials and structural parameters and growth temperatures. All the films were grown in 1×10^{-5} Torr of pure oxygen (6N) on $ScAlMgO_4$ (0001) substrates polished on both sides. This substrate is lattice-matching ZnO with a lattice mismatch as small as 0.08 %.[11] High purity polycrystalline ZnO target (6.5 N) was used through all the experiments. $Mg_{0.5}Zn_{0.5}O$, $Zn_{0.85}Cd_{0.15}O$, and $Al_{0.01}Zn_{0.99}O$ mixed ceramic targets were also used. The targets were placed at a distance of 5 cm from the substrate and ablated by KrF excimer laser pulses (248 nm, 10 Hz, 30 ns) with a fluence of 0.5 J/cm^2. The pure ZnO films having thickness ranging 17 to 81 nm were deposited at 600° C. After evaluation of deposition rates for each target, the alloy and doped films having various compositions were deposited with repeating alternating ablation of ZnO and mixed targets and switching mask patterns. In order to suppress inhomogeneous distribution of the doped ions, numbers of switching repetition were regulated so that the deposition amount in one cycle is less than the half unit cell of ZnO (0.26 nm).

7.2.2. CL-MBE growth of ZnO/$Mg_xZn_{1-x}O$ SQW and superlattices

ZnO/$Mg_xZn_{1-x}O$ SQW structures and superlattices were fabricated with varying x and ZnO well layer thickness (L_W). The Mg content of x was chosen at x=0.11 for the SQWs, and 0.12 and 0.26 for the superlattices. In order to fabricate SQW structures, 100 nm-thick $Mg_{0.11}Zn_{0.89}O$ bottom barrier was deposited on entire region with using ZnO and $Mg_{0.5}Zn_{0.5}O$ targets, and then ZnO well layer was grown with varying L_W from 1 to 9 nm. The top barrier layer with thickness of 50 nm was successively deposited to cover the ZnO well layers. In the case of the superlattice samples, $Mg_{0.06}Zn_{0.94}O$ and $Mg_{0.10}Zn_{0.90}O$ mixed targets were used to form $Mg_{0.12}Zn_{0.88}O$ and $Mg_{0.26}Zn_{0.74}O$ barrier layers, respectively. 10 period superlattices were fabricated with varying L_W between 0.7 and 4.6 nm maintaining $Mg_xZn_{1-x}O$ layer thickness (L_B) constant at 5 nm.

7.2.3. Characterization methods

The characterizations of the whole films are a time consuming part of the experiments. Structural characterization of the film pixels was investigated by a commercial x-ray diffraction (XRD) apparatus (Philips, X'-pert MRD) equipped with an originally designed masking system. Since the size of incident x-ray beam cannot be kept as small as the pixel size for different incidence (ω), we used physical mask attached on the chip surface. X-ray beam from one pixel area can be detected selectively through an open window (3.5×3.5 mm^2 in size) on a 0.5 mm-thick Cu plate covering the entire chip area. An effective ω range is limited from 10° to 80° due to the mask shadowing. Each pixel was measured in a consecutive manner by controlling alternately the stage position, sample angles, ω and ω-2θ scan measurements. It took about one hour for each pixel to measure ω rocking curve of the ZnO (0002) and ω-2θ scan for 30° $\leq 2\theta \leq$ 37° for the ZnO (0002) and the $ScAlMgO_4$ (0009) peaks (see Fig. 7-1).

The surface morphology of the films was observed by a mean of contact-mode atomic force microscopy (AFM, Seiko, SPI-3700) in air. In order to evaluate room temperature conductivity, I-V characteristic was measured with conventional four probe contacts, and then plotted by a X-Y recorder.

Optical properties were characterized by using photoluminescence (PL) spectroscopy with an excitation by 325 nm line of a cw He-Cd laser beam and standard absorption spectroscopies at temperatures ranging from 4.2 to 294 K. Frequency tripled pulses (355 nm, 10 Hz, 15ps) from a mode-locked Nd: YAG laser (Coherent) was used for strong excitation experiments at temperature ranging from 294 to 380 K. The laser beam was focused by a cylindrical lens into a stripe on the sample surface at normal incidence. Emission spectra were taken from the side edge of the samples by a monochrometer equipped with a cooled CCD detector.

7.3. Results and Discussions

7.3.1. Crystallinity and compositional homogeneity

First, let us discuss on the film quality in the terms of crystallinity and compositional homogeneity in order to confirm applicability of combinatorial synthesis. Figure 7-1 shows x-ray diffraction (XRD) patterns of nine ZnO single-layer films (3×3 mm^2 in size) having various thickness ranging from 17 to 81 nm grown on $ScAlMgO_4$ (0001) substrates. Two peaks labeled $(0009)_s$ and $(0002)_L$ are Bragg diffraction peaks of the substrate $ScAlMgO_4$ the ZnO, respectively. All the films have *c*-axis orientation, and showed full width at half maximum (FWHM) values of rocking curve at ZnO (0002) less than 100 arcsec. Clear intensity oscillations due to Laue pattern deduced from the layer thickness are observed in all samples, indicating high crystallinity, and high thickness homogeneity.

In case of CL-MBE deposition, the composition of the alloy and doped films was tuned by mixing of precursor species provided from $M_xZn_{1-x}O$ (M=Al, Mg, Cd) and pure ZnO target. As reported in the previous paper,[13] two targets were switched and certain numbers of pulses were given on both target in a cycle. We regulated the thickness of the film was less than the unit cell of ZnO (0.26 nm) so that homogeneous mixing of the elements could be expected. However, if mixing of M ions into ZnO during the one cycle of the growth is not sufficient, the films contain local compositional fluctuation. In order to the examine homogeneity of the films, $Mg_xZn_{1-x}O$ ($0<x<0.13$) films were characterized by absorption spectroscopy at room temperature. Figure. 7-2 shows squared absorption coefficients as a function of photon energy for $Mg_xZn_{1-x}O$ ($0<x<0.13$) films grown by CL-MBE and $Mg_xZn_{1-x}O$ films ($0\leq x\leq 0.17$) deposited by PLD on sapphire substrates using mixed ceramic targets having various Mg contents. Systematic shift of band gap energy (E_g) according to Mg contents can be seen in both cases. Since $Mg_xZn_{1-x}O$ alloy has a direct band gap, E_g value is defined by a relationship, $\alpha^2(h\nu)=a(h\nu-E_g)$, where α is absorption coefficient, a is a linear coefficient, and $h\nu$ is photon energy above E_g value. Linear fitting lines are plotted by dotted lines in Fig. 7-2 (a) and (b). The values of a for each spectrum are plotted as a function of E_g value in Fig. 7-2 (c). Top label of Mg content (x) is given by assuming a relationship, $E_g(x)=3.29+1.57x+2.16x^2$, deduced from the previous works.[15] Since $\alpha(h\nu)$ is directly related with density of state at the edge, the values of a should represent compositional fluctuation. In case of conventional PLD grown films, clear E_g dependence of a is seen, while the CL-MBE grown films show weak dependence and relatively smaller a than those for the PLD-grown films. Smaller a for the CL-MBE grown films is presumably due to the compositional inhomogeneity, which would give rise to the α^2 spectrum composed of the overlap of those from various compositions. In fact, we have observed much smaller a value for a $Mg_xZn_{1-x}O$ combinatorial chip when deposition amount during one cycle was as large as 1 nm. Therefore, we conclude here that reasonably homogeneous films can be grown by mixing successively supplied precursors from two targets if the deposition amount in a cycle is minimized to less than unit cell of crystal.

7.3.2. High-throughput optimization of $Mg_xZn_{1-x}O$ alloy films

Here we present systematics of band gap energy for $Mg_xZn_{1-x}O$ thin films against deposition parameters. We reported that Mg content in the films was higher than that of starting target due to rather high vapor pressure of ZnO compared with that of MgO. Thus, the growth temperature is an important parameter to determine actual Mg content. We grew a combinatorial chip consisted of $Mg_xZn_{1-x}O/Mg_{x'}Zn_{1-x'}O$ double-layer films varying the pulse ratio, which is defined as $n_{MgZnO}/(n_{ZnO}+n_{MgZnO})$, where n_{MgZnO} and n_{ZnO} are the pulse numbers during one cycle for $Mg_{0.5}Zn_{0.5}O$ and

ZnO target, respectively. Bottom layers with thickness of about 70 nm were deposited at T_g=550° C and then about 50 nm-thick layers were successively deposited at 600° C using the same deposition scheme.

Two absorption edges could be clearly observed in the absorption spectra shown in Fig. 7-3 (a) for the samples grown at P>0.2. Since the vapor pressure of Zn-related species is high, higher absorption edge comes from the top layers. E_g values for each layer deduced from $\alpha^2(h\nu) \propto (h\nu - E_g)$ relationship are plotted as a function of P in Fig. 7-3 (b). Systematic dependence is clearly seen for both cases. It should be noted here that only one deposition experiment is enough to find a suitable growth condition for pinpointing the desired band gap to make single quantum well structures discussed later.

7.3.3. Conductivity control of Al-doped ZnO films

It is well-known that *n*-type conducting ZnO can be readily obtained by III-element doping. III element-doped ZnO has been attracting considerable attention to form transparent conducting layers in modern solar cells for realizing low cost and high reproducibility. Moreover, recent theoretical prediction[16] and a claims of success[17] in *p*-type doping employ so-called *co-doping*, where III-element and nitrogen are doped in ZnO. Among number of reports of III-element doped ZnO films, however, only polycrystalline films grown on sapphire or glass substrates have been discussed. In the most cases, films contain unintentionally doped donor and acceptor due to crystalline defects such as oxygen vacancy, Zn interstitial, grain boundaries, and other defect associated with extrinsic impurity. To our best knowledge, there is no report on the electrical properties for single-crystalline films doped with III-element.

We reported that the use of lattice-matched $ScAlMgO_4$ substrates is useful not only for improving the electron mobility, by eliminating misfit dislocations, but also for reducing the residual carrier concentration. In order to examine the doping capability of single-crystalline thin films, we have grown ZnO: Al films on $ScAlMgO_4$ (0001) substrates at 400° C with varying designed Al concentrations from 1 × 10^{18} to 1 × 10^{20} cm^{-3} by using CL-MBE. Room temperature conductivity was evaluated by I-V measurements. Schematic illustration of the I-V measurement is depicted in the inset of Fig. 7-4.

Room temperature conductivity (σ) is plotted as a function of nominal Al concentration in Fig. 7-4. The σ value systematically increases up to 1.3 × 10^3 Scm^{-1} with increasing Al concentration. For comparison, the values of the films grown on sapphire substrates by PLD using ZnO: Al ceramic targets are also presented in the figure. Obviously, doping efficiencies for the films grown on $ScAlMgO_4$ substrates are much higher than those for the films grown on sapphire substrates. The use of $ScAlMgO_4$ substrates also gives us an advantage for carrier doping with precise control. All the films showed very high crystallinity as represented by full width at half maximum (FWHM) values of rocking curve for ZnO (0002) less than 200 arcsec. Thus, high conductivity, precise control of dopant concentration, and high

crystallinity could be achieved simultaneously by using CL-MBE on $ScAlMgO_4$ substrates. Further investigations are in progress using Hall measurements, secondary ion mass spectrometry, and optical characterizations.

7.3.4. Surface morphologies

For fabricating heterostructures such as quantum well and superlattice structures, it is important to regulate the film surface and interface flatness. When we grow alloy and doped films on sapphire, surface was rough than that of pure ZnO film. Therefore, we employed ZnO buffer layer prior to alloy film deposition, to increase surface smoothness for the $Mg_xZn_{1-x}O$ alloy films.[7] Recently, we have substantially improved the surface morphology by employing lattice-matched $ScAlMgO_4$ substrates.[11] Here we discuss the surface morphology of the alloy and doped films deposited on $ScAlMgO_4$ substrates without using buffer layers and extended this technique to the superlattice research.

All the samples listed in Table 8-1 were observed by AFM and representative images are shown in Fig. 7-5. As reported earlier, pure ZnO films show well-defined atomically flat terraces and 0.26 nm-high-steps (charge neutral unit cell of ZnO) as shown in Fig. 7-5 (a). Here we note that the surface of this image is composed of only four levels of terraces, i.e., interface roughness in heterostructure can be minimized as small as $\pm$0.52 nm at most. This smooth surface has been observed even on 1 μm-thick films.[11] Similar surface structure is seen in a $Mg_xZn_{1-x}O$ alloy film with x=0.075 (Fig. 7-5 (b)). Comparing with the pure ZnO, however, rather irregular step edge structures can be observed. It is interesting to note the fact that the terrace area surrounded by irregular steps is about 20 % of coverage, and this value corresponds to the deposition pulse ratio (P). The similar phenomena are observed for other pixels. Therefore, if this fact is related with the supply to the Mg-related species, less surface diffusion length of Mg-related precursors could explain the AFM image and degraded optical characteristics shown in Fig 7-2 (b). This speculation agrees with the fact that when $Mg_xZn_{1-x}O$ alloy films are directly deposited on sapphire substrate, the surface becomes quite rough.[7] However, we conclude here that the ZnO and the $Mg_xZn_{1-x}O$ alloy film grows in a two-dimensional growth mode on $ScAlMgO_4$ substrates, resulting in a sharp heterointerface between them. For instance, in case of ZnO/$Mg_{0.26}Zn_{0.74}O$ superlattice samples, atomically flat terraces (Fig. 7-5 (f)) and clear satellite peals in XRD patterns could be observed.

$Zn_{1-x}Cd_xO$ and ZnO: Al films deposited at 400° C have relatively rough surface. The surface morphology of $Zn_{1-x}Cd_xO$ films did not show any change with x (representative AFM image is shown in Fig. 7-5 (c)). On the other hands, the surface feature of ZnO: Al films is strongly depends on Al concentration (N_{Al}). As N_{Al} increases, surface roughness increases (Fig. 7-5 (d) and (e)). When a ZnO

buffer layer was used for the growth of ZnO: Al films, the surface roughness could be kept less than 5 nm with N_{Al} up to 1×10^{20} cm^{-3}.

7.3.5. High-throughput optimization of $ZnO/Mg_xZn_{1-x}O$ quantum structures

In this section, we discuss the optical characteristics of $ZnO/Mg_xZn_{1-x}O$ SQW and superlattice structures to acquire systematic information for designing device structures. In the previous work, we found out that the thermodynamic solubility limit of MgO in $Mg_xZn_{1-x}O$ epitaxial film is about x=0.15.[18] The thermal diffusion of Mg across the $Mg_xZn_{1-x}O/ZnO$ interface was observed upon the annealing above 700° C. By conventional L-MBE methods, we have succeeded to fabricate $ZnO/Mg_xZn_{1-x}O$ superlattices on sapphire substrate and showed quantum size effect in the optical transitions.[10] In general, radiative recombination process can be enhanced if low dimensional structures such as quantum wells, wires, and dots are constructed. This is because the quantum size effect modified the profile of density of states, so that the transfer integral at the band-edge becomes much larger than that of bulk semiconductor, resulting in more efficient stimulated emission. Therefore, $ZnO/Mg_xZn_{1-x}O$ heterostructures are considered as a suitable design to be used for an active layer of ultraviolet light emitting devices and lasers. Several parameters such as Mg content (x) in the barrier layer and well layer thickness (L_W), however, remain to be optimized.

A. Spontaneous emission of $ZnO/Mg_xZn_{1-x}O$ SQW structures

PL spectra of $Mg_{0.11}Zn_{0.89}O/ZnO/ Mg_{0.11}Zn_{0.89}O$ SQW films grown on a chip by single run of CL-MBE process are shown in Fig. 7-6 (a). Here alloy films for barrier layers were grown by employing two targets switched back and forth to adjust Mg content as explained in section 8.3.2. Two peaks are clearly seen in all the spectra and are assigned to be excitonic emission at n=1 quantum sub-band level (lower energy side) and the $Mg_{0.11}Zn_{0.89}O$ barrier layers, respectively. The sub-band emission line gradually shifts to higher energy side with decreasing L_W, while, the barrier emission stays at a constant energy of about 3.53 eV. This indicates photo-excited carriers in barrier layers are transferred into the quantum level in the well layers. The peak position, PL intensity, and FWHM values (Δ) for the sub-band emission are plotted as a function of L_W in Fig. 7-6 (b) and (c). For a comparison, values deduced from $ZnO/Mg_{0.15}Zn_{0.85}O$ multiple quantum well films grown on sapphire substrates[19] are also plotted. Although peak position is similar to the previous results, slight difference of Δ values is clearly seen as shown in Fig. 7-6 (c) (bottom trace). Therefore, we conclude that the SQW structures have reasonably good qualities, but there can be considerable spatial fluctuation of Mg content in the barrier layers. From

the device application viewpoint, we estimate an optimum L_w ranging from 3 to 6 nm, judging from the magnitudes of the integrated emission intensity and the peak width, as denoted by a gray mesh in Fig. 7-6 (c).

For minimizing the Mg inhomogeneity problem, we used $Mg_xZn_{1-x}O$ targets having optimal (x=0.06 and 0.1) to grow barrier layers in ZnO/$Mg_xZn_{1-x}O$ superlattices with x=0.12 and 0.26, respectively. Thus, the compositional fluctuation problem caused by target switching could be eliminated for those superlattices. A schematic band diagram of a superlattice is presented in Fig. 7-7 (a). In general, band gap discontinuity (ΔE_C and ΔE_V) is an important parameter to design various devises based on semiconductor heterostructure such as quantum cascade lasers.[20] As for ZnO/$Mg_xZn_{1-x}O$ system, band gap discontinuities still remains to be elucidated, although a ratio of $\Delta E_C/\Delta E_V$=0.9 has been proposed.[10] This value was obtained as a fitting parameter in a theoretical calculation, which was performed to explain the relationship between L_W and observed PLE peak energies of ZnO/$Mg_{0.2}Zn_{0.8}O$ superlattice grown on sapphire substrates. The sample quality of those superlattices was not as high as brand new results shown below.

B. Spontaneous and stimulated emissions of ZnO/$Mg_xZn_{1-x}O$ superlattices

Figure 7-7 (b) and (c) shows room temperature PL and absorption spectra of two kinds of superlattices with x=0.12 and 0.26, respectively, grown on the lattice-matched and transparent $ScAlMgO_4$ substrates. PL peaks and absorption edges corresponding to the sub-band level transitions can be clearly observed. These clear absorption spectra have never been obtained from the sample grown on sapphire substrate because of the lack of transparency due to thick ZnO buffer layer.[10] The barrier emission peaks was absent because of well developed sub-band in these superlattices.

All the superlattice films were also characterized under strong excitation conditions using frequency tripled Nd: YAG laser pulses. Figure 7-8 shows stimulated emission spectra of a superlattice film having x=0.12 and L_W=1.8 nm measured at room temperature. Strong and sharp emission peak are observed above a very low threshold (I_{th}=17 kW/cm^2), and the intensity rapidly increases as excitation intensity (I_{ex}) increases, as can be clearly seen in the inset figure. For the comparison, spontaneous PL and absorption spectra are also given. The spontaneous PL peak is located at the same energy of absorption peak, indicating excitonic spontaneous emission due to transition between sub-band levels. Whereas, the stimulated emission peaks show Stokes shift, that is, whose peak energies are located lower than that the absorption peak energy by about 100 meV. This energy shift is frequently observed in II-VI quantum well

structures, as was discussed with various mechanisms such as localized-exciton[21], exciton-exciton scattering[22], and bi-exciton[23]. Considering some results in these reports, it can be expected that population inversion is readily achieved by the photo-excitation because of smaller density of state at localized states, resulting in very low threshold. However, further work is needed to elucidate the emission mechanism.

Peak energies for various emissions and absorptions of the superlattices are summarized in Fig. 7-9 (a) and (b). The L_W dependence of peak positions can be clearly seen not only for the spontaneous PL (●) but also for the stimulated emission (■). Excellent agreement, seen between the absorption peak (Δ) and the spontaneous PL peak, indicates well-regulated heterointerfaces as well as small compositional fluctuations in the barrier layers. Stokes shifts between ● and Δ is observed only for the samples with x=0.26 and L_W<2.3. This is presumably due to the possible spatial fluctuations of Mg content in the barrier layers because x is much larger than the thermodynamic solubility limit (x=0.15). This also causes relatively large peak widths of the spontaneous PL lines for x=0.26 superlattices as indicated by error bars for ● symbols. In order to estimate ΔE_C and ΔE_V, we have performed simulations to the observed relationships between L_W and the absorption peak energy by using reported effective masses of electron (m_e*=0.28) and hole (m_h*=1.8) and considering finite potential barrier. The best fit was obtained with $\Delta E_C/\Delta E_V$=0.15 for x=0.12 films and 0.25 for x=0.26 films, respectively.

Almost all the superlattices showed stimulated emission below maximum excitation intensity used in this study (58 kW/cm^2). The threshold values are plotted against L_W by symbols ●(x=0.12) and ○ (x=0.26) in Fig. 7-9 (c). Since pumping laser energy is constant at 3.49 eV, when the absorption state locates higher than that energy, stimulated emission did not take place as seen in the case of x=0.26 films with L_W below 1 nm. As for x=0.12 superlattices, threshold is below 22 kW/cm^2, and the lowest threshold is as small as 11 kW/cm^2. Very high efficiency of the stimulated emission could be demonstrated even at room temperature. Besides, there is a big advantage of tuning the emission energy from 3.2 to 3.4 eV.

From the device application viewpoint, we tested high temperature operation of the stimulated emission. Figure 7-10 shows temperature dependence of the I-I_{ex} curves of a superlattice with x=0.26 and L_W=4.2 nm measured under strong excitation with Nd: YAG laser pulses at a temperature range between 21° C and 104° C. The threshold of the stimulated emission increases gradually with increasing temperature. The inset shows temperature dependence of ln(I_{th}) for obtaining characteristic temperature (T_0) defined by the formula $I_{th}(T)=I_0\exp(T/T_0)$, where, I_o is a constant, T is the absolute temperature, $I_{th}(T)$ is the threshold. The T_0 of 87 K is considerably larger than that of 55 nm-thick ZnO/sapphire (67 K) showing excitonic lasing with the lowest threshold (24 kW/cm^2).[1] We would tentatively attributed this improvement to the excitonic emission process enhanced by quantum size effect. The wavelength drift caused by the temperature change was estimated to be about 0.09 nm/K. This value is very close to the

theoretical value (0.085 nm/K) for the stimulated emission with exciton-exciton scattering process (*ex-ex*).[24] If the emission process is dominated by exciton-electron scattering, which is the most likely the case except for *ex-ex* and electron-hole-plasma (EHP) processes, two times larger value should be expected.[25] Therefore, we conclude that the stimulated emission due to *ex-ex* process occurs in the well layers of the superlattice samples.

7.4. Conclusions

We have performed parallel syntheses of various films and heterostructures based on ZnO with using a combinatorial laser MBE system. High-throughput optimization has been demonstrated by using conventional characterizations tools to show excellent thin film qualities, represented by high crystallinity, atomically flat surfaces and heterointerfaces, and high doping efficiency. These techniques have been also applied for constructing quantum well structures based on ZnO, resulting in very high-performance ultraviolet stimulated emission. Only 8 chips made in 8 separate runs provided 72 samples and crucial information enough for designing device structures.

Table 7-1. Film compositions, structures, and growth temperatures of various combinatorial chips fabricated in this study. The films were grown by varying *combinatorial parameter* and keeping *constant parameter*. *Note* briefly describes main topics investigated with each individual chip.

Chip	*Materials*	T_g (°C)	*Combinatorial parameter*	*Const. parameter*	*Note*
#1	ZnO	600	layer thickness (L)	composition	crystallinity
#2	$Mg_xZn_{1-x}O$	600	x	L~70 nm	widegap
#3	$Mg_xZn_{1-x}O$ bilayer	600/550	x, T_g	L~70/70 nm	optimizing x
#4	$Zn_{1-x}Cd_xO$	400	x	L~70 nm	narrow gap
#5	ZnO: Al	400	x	L~100 nm	conductivity
#6	single quantum wells	600	well layer thickness (L_W)	L_B, x=0.11	optimizing L_W
#7	superlattices #1	600	L_W	L_B, x=0.12	threshold
#8	superlattices #2	600	L_W	L_B, x=0.26	threshold , T_0

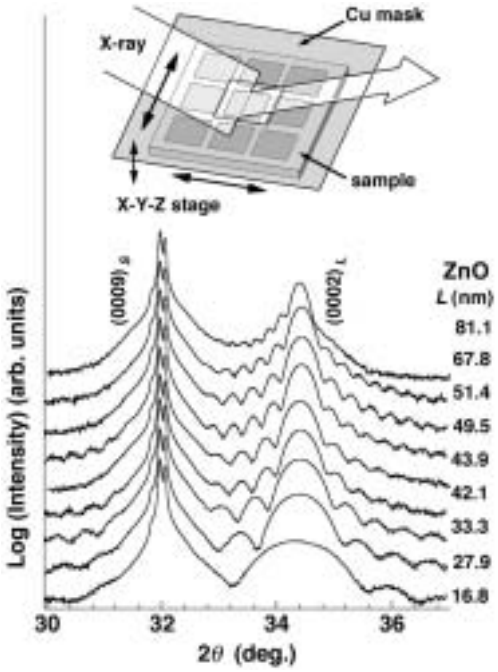

Figure 7-1. X-ray diffraction (XRD) patterns of pure ZnO thin films having various layer thickness grown on $ScAlMgO_4$ substrates (chip #1). $(0009)_s$ and $(0002)_L$ are Bragg diffraction peaks of the substrates and the ZnO films, respectively. Clear intensity oscillations are observed in all the patterns, indicating high crystallinity and high thickness homogeneity. Inset depicts schematic illustration of XRD set up with a Cu mask used in this study.

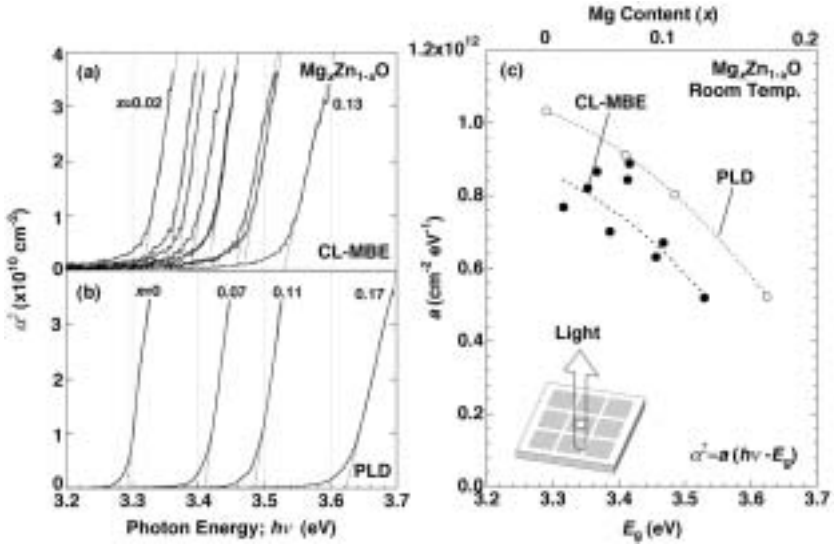

Figure 7-2. Squared absorption coefficients (α^2) as a function of photon energy ($h\nu$) of $Mg_xZn_{1-x}O$ films grown (a) on $ScAlMgO_4$ (0001) by combinatorial laser MBE (CL-MBE) (chip #2) and (b) on sapphire by conventional pulsed laser deposition (PLD). The dotted lines are linear fit lines at the energies near the band gap (E_g). (c) The linear coefficient (a) of the fit lines ($\alpha^2 = a(h\nu-E_g)$) plotted against E_g for the samples grown by CL-MBE (●) and PLD (○). Inset depicts schematic illustration of the absorption spectroscopy measurement.

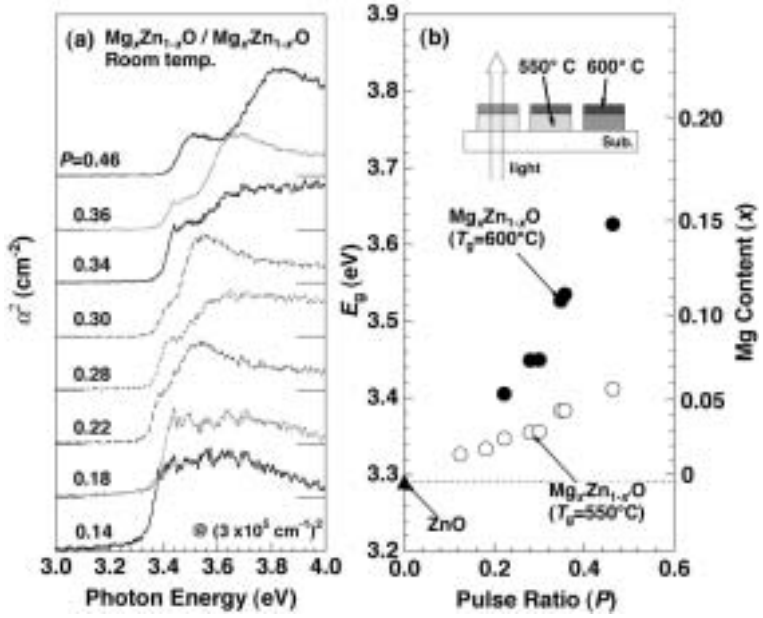

Figure 7-3. (a) Squared absorption coefficients (α^2) as a function of photon energy ($h\nu$) of $Mg_xZn_{1-x}O$ bilayer films grown on $ScAlMgO_4$ (0001) (chip #3). Top and bottom layers were grown at 550° C and 600° C respectively with the same condition of mask control and the combination of the targets. Each pixel has different pulse ration, P, which is defined as $n_{MgZnO}/(n_{ZnO}+n_{MgZnO})$, where n_{MgZnO} and n_{ZnO} is pulse numbers for $Mg_{0.5}Zn_{0.5}O$ and ZnO targets, respectively. Two absorption edges corresponding to those from the top and bottom layers are seen in each spectrum. (b) Band gap (E_g) deduced from $\alpha^2 = a(h\nu-E_g)$ relationship plotted against P. It is noteworthy that E_g values of 13 samples could be evaluated from only one deposition experiment. Inset depicts cross-sectional illustration of the doubled-layer films.

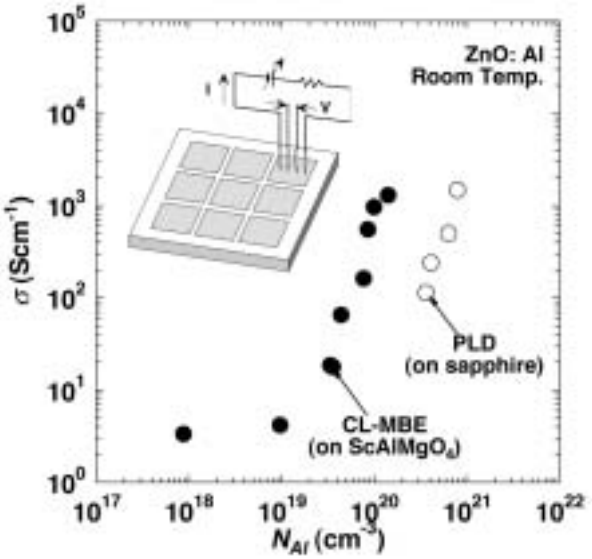

Figure 7-4. Room temperature conductivity (σ) as a function of nominal Al concentration (N_{Al}) of Al-doped ZnO films (ZnO: Al) (●: chip #5). For a comparison, conductivity values of ZnO: Al films grown on sapphire substrates by PLD using various ZnO: Al ceramic targets are also presented (○). Inset shows schematic illustration of four probe measurement.

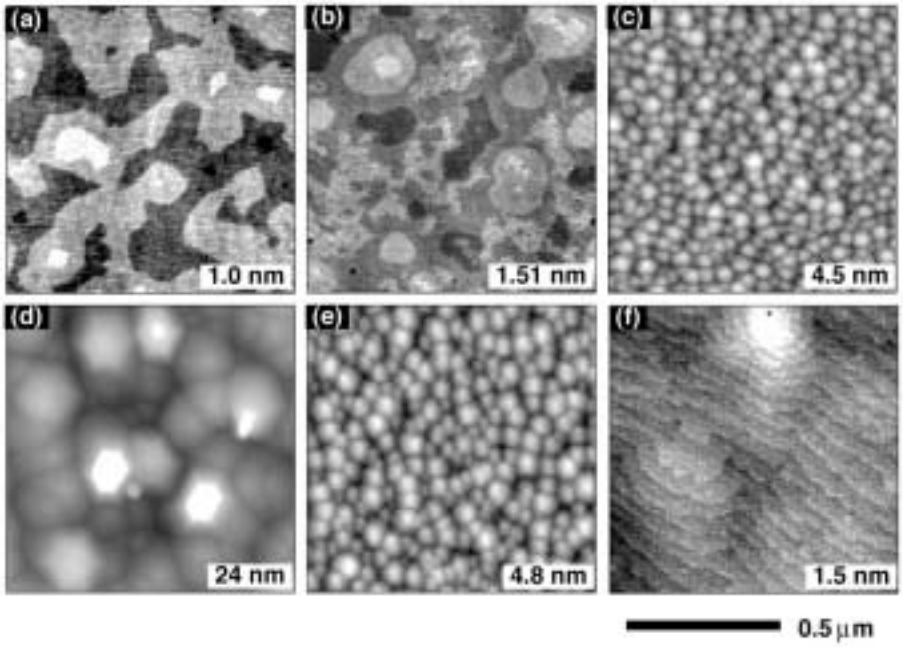

Figure 7-5. AFM images of (a) pure ZnO (L=68 nm), (b) $Mg_xZn_{1-x}O$ (x=0.075), (c) $Zn_{1-x}Cd_xO$ (x=0.009). (d) ZnO: Al ($N_{Al}=1 \times 10^{20}$ cm^{-3}), (e) ZnO: Al ($N_{Al}=1 \times 10^{18}$ cm^{-3}), and (f) $ZnO/Mg_{0.26}Zn_{0.74}O$ superlattice films chosen as a pixel in the combinatorial chips of #1, #2, #4, #5, and #8 respectively. Well-defined surface morphology ((a), (b), and (f)) indicates that two-dimensional growth mode took place in the growth of ZnO and $Mg_xZn_{1-x}O$ films, whereas three-dimensional grain growth mode dominated in cases of $Zn_{1-x}Cd_xO$ and ZnO: Al films ((b), (c), and (d)).

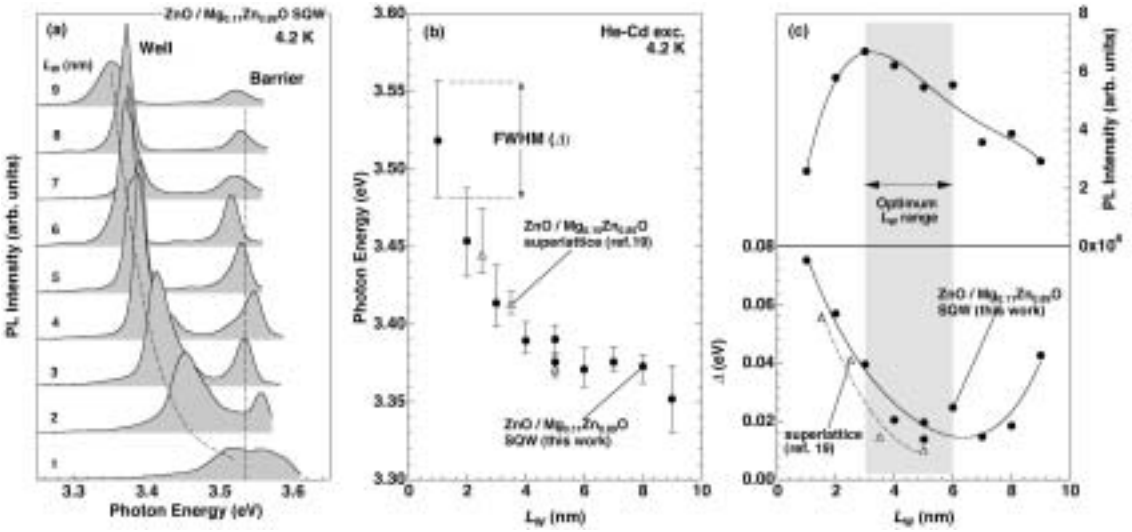

Figure 7-6. (a) PL spectra of the $ZnO/Mg_{0.11}Zn_{0.89}O$ single quantum well films (chip #6) with various well layer thickness ($1 \leq L_W$ (nm)≤ 9) measured at 4.2 K. Two PL peaks of ZnO well layers and $Mg_{0.11}Zn_{0.89}O$ barrier layers are clearly seen. (b) PL peak energy of the ZnO well layers plotted as a function of L_W. Error bars show full width at half maximum (FWHM) (Δ) (c) Integrated intensity and peak width (Δ) of PL peaks of the well layers (●) as a function of L_W. By judging from these results, an optimum L_W is found at $3 \leq L_W$ (nm)≤ 6, as indicated by the gray mask. For the comparison, some data points taken from $ZnO/Mg_{0.15}Zn_{0.85}O$ superlattice films (Ref. 19) are plotted by triangles in (b) and (c).

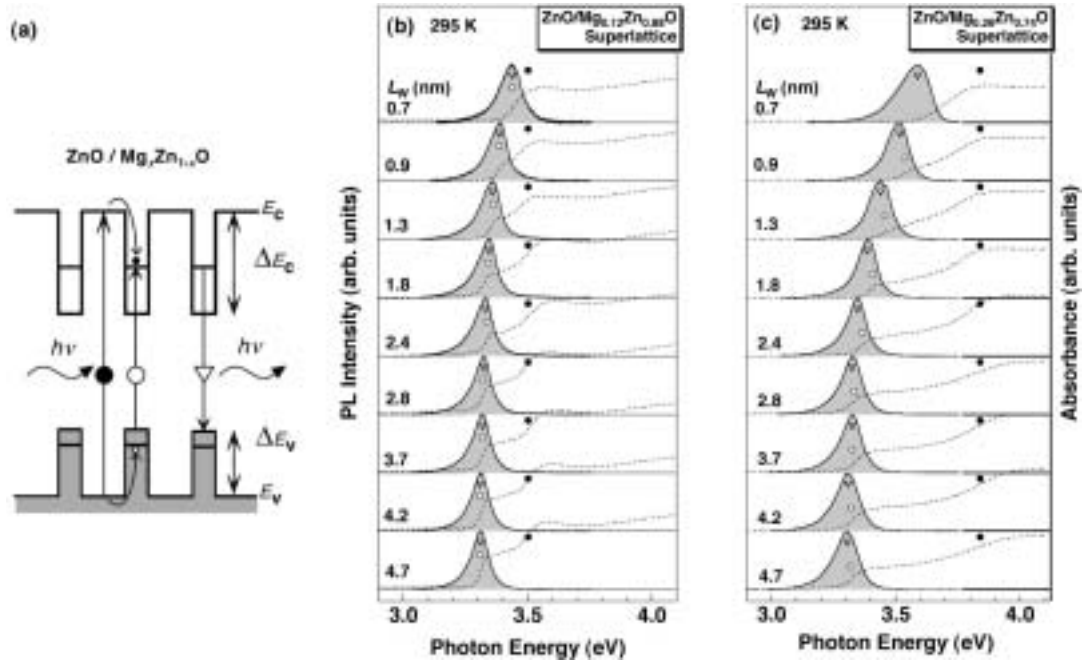

Figure 7-7. (a) Schematic energy diagrams of conduction band minimum (E_c) and valence band maximum (E_v) in the $ZnO/Mg_xZn_{1-x}O$ superlattices. (b) and (c) Room temperature PL and absorption spectra of $ZnO/Mg_xZn_{1-x}O$ superlattices with x=0.12 and 0.26 (chip #7 and #8), respectively.

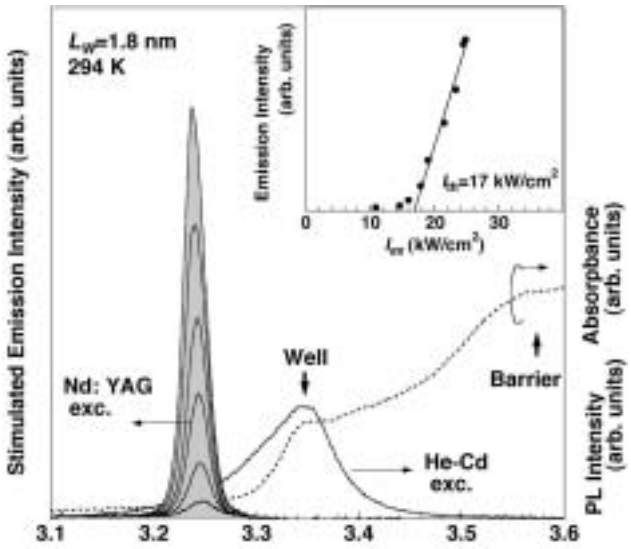

Figure 7-8. Stimulated emission spectra of a ZnO/$Mg_{0.12}Zn_{0.88}O$ superlattice film (L_W=1.8 nm) taken under various excitation intensities (I_{ex}) using frequency tripled Nd: YAG laser pulses. Weak excitation PL spectrum and absorption spectrum for the same film is also presented. Inset depicts integrated intensity of stimulated emission peak as a function of I_{ex}. Threshold intensity (I_{th}) is evaluated as 17 kW/cm^2.

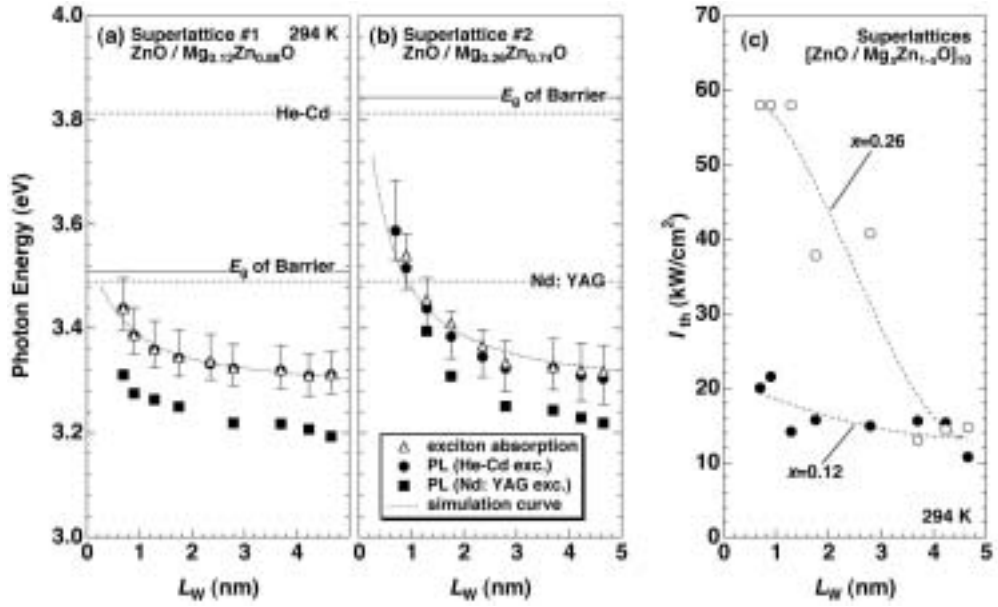

Figure 7-9. Room temperature optical transition energies of sub-band absorption (△), spontaneous PL (●), and stimulated emission (■) as a function of well layer thickness (L_W) for the ZnO/$Mg_xZn_{1-x}O$ superlattices with x=0.12 (a) and x=0.26 (b). Error bars show peak widths (FWHM) of spontaneous PL lines. Dotted lines are simulation curves calculated by assuming m_e*=0.28, m_h*=1.8, and $\Delta E_C/\Delta E_V$=0.2±0.05. E_g values of $Mg_{0.12}Zn_{0.88}O$ and $Mg_{0.26}Zn_{0.74}O$ (solid lines), and the energies of He-Cd and frequency tripled Nd: YAG lasers (dashed lines) are also shown. (c) L_W dependence of the stimulated emission threshold (I_{th}) of the ZnO/$Mg_xZn_{1-x}O$ superlattices with x=0.12 (●) and x=0.26 (○).

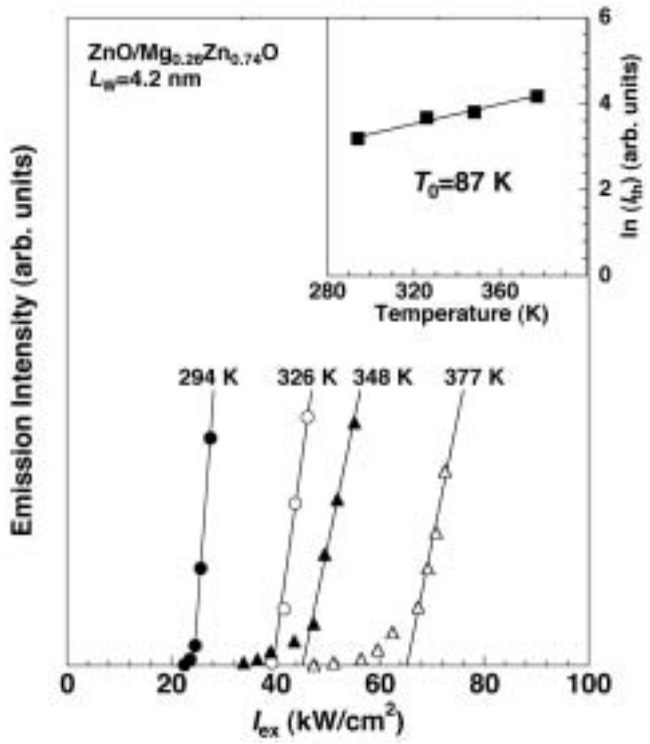

Figure 7-10. Temperature dependence of the emission intensity as a function of excitation intensity (I_{ex}) of a $ZnO/Mg_{0.26}Zn_{0.74}O$ superlattice film (L_W=4.2 nm). Inset depicts threshold intensity (I_{th}) of the same sample as a function of temperature. Characteristic temperature (T_0) is as high as 87 K.

References

[1] Z.K. Tang, G.K.L. Wong, P. Yu, M. Kawasaki, A. Ohtomo, H. Koinuma, and Y. Segawa, Appl. Phys. Lett. **72**, 3270 (1998).

[2]A. Ohtomo, M. Kawasaki, Y. Sakurai, Y. Yoshida, H. Koinuma, P. Yu, Z.K. Tang, G.K.L. Wong, and Y. Segawa, Mat. Sci. Eng. **B54**, 24 (1998).

[3] Z.K. Tang, P. Yu, G.K.L. Wong, M. Kawasaki, A. Ohtomo, H. Koinuma, and Y. Segawa, Solid State Comm. **103**, 459 (1997).

[4] Y. Segawa, A. Ohtomo, M. Kawasaki, H. Koinuma, Z.K. Tang, P. Yu, and G.K.L. Wong, Phys. Stat. Sol. **B202**, 669 (1997).

[5] M. Kawasaki, A. Ohtomo, I. Ohkubo, H. Koinuma, Z.K. Tang, P. Yu, G.K.L. Wong, B.P. Zhang, and Y. Segawa, Mat. Sci. Eng. **B56**, 239 (1998).

[6] Y. Kayanuma, Phys Rev. **B38**, 9797 (1988).

[7] A. Ohtomo, M. Kawasaki, T. Koida, K. Masubuchi, H. Koinuma, Y. Sakurai, Y. Yoshida, T. Yasuda, and Y. Segawa, Appl. Phys. Lett. **72**, 2466 (1998).

[8] M. Kawasaki, A. Ohtomo, R. Shiroki, I. Ohkubo, H. Kimura, G. Isoya, T. Yasuda, Y. Segawa, and H. Koinuma, *Ext. Abst. 1988 Int'l Conf. Solid State Mat. Devices*, 356-357 (1988).

[9] A. Ohtomo, K. Kawasaki, Y. Sakurai, I. Ohkubo, R. Shiroki, Y. Yoshida, T. Yasuda, Y. Segawa, and H. Koinuma, Mat. Sci. Eng. **B56**, 263 (1998).

[10] A. Ohtomo, M. Kawasaki, I. Ohkubo, H. Koinuma, T. Yasuda, and Y. Segawa, Appl. Phys. Lett. **75**, 980 (1999).

[11] A. Ohtomo, K. Tamura, K. Saikusa, K. Takahashi, T. Makino, Y. Segawa, H. Koinuma, and M. Kawasaki, Appl. Phys. Lett. **75**, 2635 (1999).

[12] K. Tamura, A. Ohtomo, K. Saikusa, Y. Osaka, T. Makino, Y. Segawa, H. Koinuma, and M. Kawasaki, J. Cryst. Growth, in press.

[13] Y. Matsumoto, M. Murakami, Z.W. Zin, A. Ohtomo, M. Lippmaa, M. Kawasaki, and H. Koinuma, Jpn. J. Appl. Phys. **38**, L603 (1999).

[14] Z.W. Jin, M. Murakami, T. Fukumura, A. Ohtomo, Y. Matsumoto, M. Kawasaki, and H. Koinuma, J. Cryst. Growth, in press.

[15] This equation was deduced from the observed $E_g(x)$ values reported independently in Ref. 7 ($0.19<x<0.33$) and in Ref. 13 ($0<x<0.19$).

[16] T. Yamamoto and H. Yoshida, Jpn. J. Appl. Phys. **68**, L166 (1999).

[17] K. Minegishi, Y. Koiwai, Y. Kikuchi, K. Yano, M. Kasuga, and A. Shimizu, Jpn. J. Appl. Phys. **36**, L1453 (1997)., and M. Joseph, H. Tabata and T. Kawai, Jpn. J. Appl. Phys. **38**, L1205 (1999).

[18] A. Ohtomo, R. Shiroki, I. Ohkubo, H. Koinuma, and M. Kawasaki, Appl. Phys. Lett. **75**, 4088 (1999).

[19] Y. Segawa, T. Yasuda, A. Ohtomo, and M. Kawasaki (unpublished).

[20] J. Faist, F. Capasso, D. L. Sivro, C. Sirtori, A. L. Hutchinson, and A. Y. Cho, Science **264**, 553 (1994).

[21] Y. Kuroda, I. Suemune, Y. Fujii, and M. Fujimoto, Appl. Phys. Lett. **61**, 1182 (1992), and C. J. Stevens, R. Cingolani, L. Calcagnile, M. Dabbicco, R. A. Taylor, J. F. Ryan, M. Lomascolo, and I. Suemune, Superlattices and Microstructures **16**, 371 (1994).

[22] M. Umlauff, H. Kalt, W. Langbein, O. Wind, K. P. Geyzers, and M. Heuken, Adv. Mater. Opt. Electron. **3**, 51 (1994).

[23] Y. Yamada, T. Mishina, Y. Masumoto, Y. Kawakami, J. Suda, Sz. Fujita, and Sg. Fujita, Phys. Rev. **B51**, R2289 (1995).

[24]J. M. Hvam, Phys. Stat. Sol. **B63**, 511 (1974)., and C. Klingshirn, Phys. Stat. Sol. **B71**, 547 (1975).

[25] G. H. Jensen and E. Mollwo, Phys. Stat. Sol. **B60**, 169 (1973)., and Ref. 21.

Chapter 8. General Conclusions

Extensive research of high-T_C superconducting films for more than 10 years has opened door to new class of electronics in which versatile properties of epitaxial metal oxide films and heterostructures play a major role. The present study stands on the status for expanding this trend towards photonic branch of "oxide electronics", so that we started to study ZnO thin films for realizing ultraviolet light emitting device. In this thesis, epitaxial growth techniques using laser ablation process, optical properties of nanocrystalline films and superlattices based on ZnO and possible *p*-type ZnO formation were discussed.

Laser molecular-beam epitaxy (L-MBE) technique has been developed and used to grow various films based on ZnO such as nanocrystalline films on lattice-mismatched substrates, single crystalline films on lattice-matched substrates, alloy films ($Mg_xZn_{1-x}O$ and $Zn_{1-x}Cd_xO$), *n*- and *p*-type doped films (ZnO: Al and ZnO: N), and their heterostructures (ZnO/$Mg_xZn_{1-x}O$ quantum well and superlattice structures). Five years of thesis research has revealed the followings.

Thin film growth

- L-MBE can provide precursor species as metal oxides particles, therefore oxygen deficiency is suppressed during growth even at high temperatures (~1000° C).
- High energetic process of laser ablation provides high driving force for thin film growth under non-equilibrium condition which enable us to grow solid solution films much above the thermodynamic solubility limit.
- Nitrogen can be doped into ZnO by use of RF-plasma cell during growth to obtain *p*-type material. Nitrogen concentration in the film is tuned from 10^{18} to 10^{20} cm^{-3} by changing growth temperature (K. Tamura *et. al*., J. Cryst. Growth, in press).

Materials

- *c*-axis oriented ZnO films epitaxially grow on sapphire substrate (18 % lattice-mismatch). If a higher order epitaxial relationship is taking into account, there can be translationally incoherent grain boundaries.
- Hexagonally shaped grains are closely packed and aligned as honeycomb fashion. The size of grains can be controlled by taking nucleation and growth process into account.
- Impurity as well as oxygen deficiency and crystallinity (stress, in-plane and out of plane mosaicness, lateral grain size) affect the emission properties.

- The films grown on lattice-matched (0.09 % lattice-mismatch) $ScAlMgO_4$ have high mobility (~100 cm^2/Vs) together with low residual carrier concentration (~10^{15} cm^{-3}).

Physics

- Spontaneous and stimulated emissions due to *ex-ex* collision process and electron-hole plasma are seen in ZnO nanocrystalline films as increasing pumping intensity.
- The incoherent grain boundaries serve as potential barriers for carrier confinements, and there is an optimum crystal size (50 nm) for excitonic lasing.
- The incoherent grain boundaries serve as mirrors to form longitudinal cavity.
- Band gap energy varies from 3.0 to 4.0 eV in $Mg_xZn_{1-x}O$ and $Zn_{1-x}Cd_xO$ ternary alloy systems.
- Quantum size effect in $ZnO/Mg_xZn_{1-x}O$ superlattices is confirmed by PL and PLE measurements.

Devices

- The excitonic recombination process dominates the stimulated emissions in $ZnO/Mg_xZn_{1-x}O$ superlattices. The threshold excitation intensity is as low as 11 kW/cm^2. (Low-threshold laser diodes would be expected).
- The emission energy was tuned between 3.2 and 3.4 eV, depending on the well layer thickness and/or the Mg content in the barrier layers. An optimum well layer thickness was found to be in a range of 3-6 nm.
- Excitonic stimulated emission at temperatures up to 100° C was demonstrated and a characteristic temperature was as high as 87 K for the best sample optimized by the combinatorial approach.
- Once *p*-type ZnO is available, high efficient light emitting devices based on ZnO would be expected.

These technological issues and phenomenon are important and on the traditional track of the progress in semiconductor technology. ZnO is one of the materials, which have the longest and most extensive history conducting film, and surface acoustic devices. It is surprising for us to find out a novel function in such an old material. One can say that L-MBE gave a new life to an old material. There should be other oxides, which may explore much exotic properties.

Publications

1. “Room temperature stimulated emission from ZnO/$Mg_xZn_{1-x}O$ multi quantum wells grown on $ScAlMgO_4$ (0001) substrates”, A. Ohtomo, T. Makino, K. Tamura, Y. Matsumoto, Y. Segawa, Z.K. Tang, G.K.L. Wong, H. Koinuma, and M. Kawasaki, submitted to *Appl. Phys. Lett.*

2. “Exciton spectra in ZnO thin films on lattice-matched substrates grown with laser MBE method”, T. Makino, N.T. Tuan, Y. Segawa, C.H. Chia, M. Kawasaki, A. Ohtomo, K. Tamura, and H. Koinuma, submitted to *Appl. Phys. Lett.*

3. “Room temperature exciton luminescence in ZnO/(Mg,Zn)O multi-quantum wells on lattice-matched substrates", T. Makino, N.T. Tuan, H.D. Sun, Y. Segawa, C.H. Chia, M. Kawasaki, A. Ohtomo, K. Tamura, and H. Koinuma, submitted to *Appl. Phys. Lett.*

4. “High-throughput optimizations of alloy and doped films based on ZnO and parallel synthesis of ZnO/$Mg_xZn_{1-x}O$ quantum wells using combinatorial laser MBE towards ultraviolet laser”, A. Ohtomo, T. Makino, K. Tamura, Y. Matsumoto, Y. Segawa, Z.K. Tang, G.K.L. Wong, H. Koinuma, and M. Kawasaki, submitted to *Proceedings of SPIE*, San Jose Convention center, San Jose, USA, January 22-28 (2000).

5. “Convergent-beam parallel detection x-ray diffraction system for characterizing combinatorial epitaxial thin films (Invited Paper)”, K. Omote, T. Kikuchi, J. Harada, M. Kawasaki, A. Ohtomo, T. Ohnishi, D. Komiyama, and H. Koinuma, submitted to *Proceedings of SPIE*, San Jose Convention center, San Jose, USA, January 22-28 (2000).

6. “Optical characterization for combinatorial systems based on semiconductor ZnO”, T. Makino, G. Isoya, Y. Segawa, C. H. Chia, T. Yasuda, M. Kawasaki, A. Ohtomo, K. Tamura, and H. Koinuma, submitted to *Proceedings of SPIE*, San Jose Convention center, San Jose, USA, January 22-28 (2000).

7. “Temperature dependence of four-wave-mixing spectra in ZnO thin films on sapphire substrates grown with laser-MBE”, T. Makino, N.T. Tuan, Y. Segawa, C.H. Chia, A. Ohtomo, M. Kawasaki, and H. Koinuma, *J. Lumin*. in press.

8. “Concept and Development of Combinatorial Laser MBE for Oxide Electronics”, H. Koinuma, M. Kawasaki, T. Itoh, A. Ohtomo, M. Murakami, Z.W. Jin, and Y. Matsumoto, *Physica C*, in press

9. “Investigation of ZnO/sapphire interface and formation of ZnO nanocrystalline by laser MBE”, I. Ohkubo, Y. Matsumoto, A. Ohtomo, T. Ohnishi, A. Tsukasaki, M. Lippmaa, H. Koinuma, M. Kawasaki, *Appl. Surf. Sci.* in press.

10. "Thermal stability of supersaturated $Mg_xZn_{1-x}O$ alloy films and $Mg_xZn_{1-x}O$/ZnO heterointerfaces", A. Ohtomo, R. Shiroki, I. Ohkubo, H. Koinuma, and M. Kawasaki, *Appl. Phys. Lett.* **75**, 4088 (1999).

11. "Lateral grain size and electron mobility in ZnO epitaxial films grown on sapphire substrates", A. Ohtomo, H. Kimura, K. Saito, T. Makino, Y. Segawa, H. Koinuma, and M. Kawasaki, *J. Cryst. Growth.* in press.

12. "ZnO/$Mg_xZn_{1-x}O$ Quantum Structures (Invited Paper)", A. Ohtomo and M. Kawasaki, *Proceedings of International Workshop on ZnO*, 17 (1999), Wright State University, Ohio, USA, October 7-8 (1999).

13. " Optical spectra of ZnO films on lattice-matched substrates grown with laser MBE (Invited Paper)", T. Makino, G. Isoya, Y. Segawa, C.H. Chia, T. Yasuda, M. Kawasaki, A. Ohtomo, K. Tamura, and H. Koinuma, *Proceedings of International Workshop on ZnO*, 18 (1999), Wright State University, Ohio, USA, October 7-8 (1999).

14. “Temperature dependence of absorption spectra in ZnO thin films on lattice-matched substrates grown with laser-MBE method”, C.H. Chia, T. Makino, Y. Segawa, M. Kawasaki, A. Ohtomo, K. Tamura, and H. Koinuma, *Proceedings of 10_{th} Meeting on Solid State Photophysics*, p. 45 (1999) (Sansho Co.Ltd, Osaka, Japan), Osaka, Japan, November (1999).

15. "Novel Semiconductor Technologies of ZnO films towards Ultraviolet LEDs and Invisible FETs (Invited Paper)", A. Ohtomo, and M. Kawasaki, *Proceedings of The 6_{th} International Display Workshop*, 881, (1999), Sendai International Center, Sendai, Japan, November 1-3 (1999).

16. "Epitaxial growth of ZnO films on lattice-matched $ScAlMgO_4$(0001) substrates", K. Tamura, A. Ohtomo, K. Saikusa, Y. Osaka, T. Makino, Y. Segawa, H. Koinuma, and M. Kawasaki, *J. Cryst. Growth*, in press.

17. "Combinatorial laser MBE synthesis of 3d ion doped epitaxial ZnO thin films", Zhengwu Jin, Y. Matsumoto, M. Murakami, T. Fukumura, A. Ohtomo, M. Kawasaki, and H. Koinuma, *J. Cryst. Growth.* in press.

18. "Optical spectra in ZnO thin films on lattice-matched substrates grown with laser MBE method", T. Makino, G. Isoya, Y. Segawa, C. H. Chia, T. Yasuda, M. Kawasaki, A. Ohtomo, K. Tamura, and H Koinuma, *J. Cryst. Growth,* in press.

19. "Parallel synthesis and x-ray diffraction for combinatrial lattice engineering", T. Ohnishi, A. Ohtomo, D. Komiyama, M. Lippmaa, S. Ohashi, N. Nakagawa, C. Stauter, T. Kikuchi, K. Omote, M. Kawasaki, and H. Koinuma, submitted to *Nature*.

20. "A Novel oxide diluted magnetic semiconductor: Mn doped ZnO", T. Fukumura, Z.W. Jin, A. Ohtomo, H. Koinuma, and M. Kawasaki, *Appl. Phys. Lett.* **75**, 3366 (1999).

21. "Optical and photoelectrical properties of oriented ZnO films", J. W. Tomm, B. Ullrich, X. G. Qiu, A. Ohtomo, M. Kawasaki, H. Koinuma, and Y. Segawa, submitted to *J. Appl. Phys.* **87**, 1844 (2000).

22. "In-plane and polar orientations of ZnO thin films grown on atomically flat sapphire", I. Ohkubo, A. Ohtomo, T. Ohnishi, Y. Matsumoto, H. Koinuma, and M. Kawasaki, *Surf. Sci. Lett.* **443**, L1043 (1999).

23. "Single-crystalline ZnO films grown on lattice matched $ScAlMgO_4$ (0001) substrates", A. Ohtomo, K. Tamura, K. Saikusa, K. Takahashi, T. Chikyo, T. Makino, Y. Segawa, Z.K. Tang, H. Koinuma, and M. Kawasaki, *Appl. Phys. Lett.* **75**, 2635 (1999).

24. "Structure and optical properties of $ZnO/Mg_{0.2}Zn_{0.8}O$ superlattice", A. Ohtomo, M. Kawasaki, I. Ohkubo, H. Koinuma, T. Yasuda, and Y. Segawa, *Appl. Phys. Lett.* **75**, 980 (1999).

25. " $Mg_xZn_{1-x}O$ as a II-VI semiconductor alloy", A. Ohtomo, M. Kawasaki, T. Koida, K. Masubuchi, H. Koinuma, Y. Sakurai, Y. Yoshida, T. Yasuda, and Y. Segawa, *Appl. Phys. Lett.* **72**, 2466 (1998).

26. "Epitaxial growth of single crystalline ZnO films towards novel transparent opt-electronics", A. Ohtomo, K. Tamura, K. Saikusa, Y. Osaka, H. Kimura, H. Koinuma, and M. Kawasaki, *Proceedings of the 3_{rd} Symposium on Atomic-Scale Surface and Interface Dynamic*, 147-150 (1999).

27. "ZnMnO as a novel diluted magnetic semiconductor system", T. Fukumura, Z.W. Jin, A. Ohtomo, H. Koinuma, and M. Kawasaki, *Proceedings of the 3_{rd} Symposium on Atomic-Scale Surface and Interface Dynamic*, 161-164 (1999).

28. "ZnO alloy system and quantum structures towards ultraviolet laser", A. Ohtomo, I. Ohkubo, M. Kawasaki H. Koinuma, G. Isoya, T. Yasuda and Y. Segawa, *Proceedings of the 2_{nd} International Symposium on Blue Laser and Light Emitting Diodes*, 711 (1998).

29. "Fabrication of alloys and superlattices based on ZnO towards ultraviolet laser", A. Ohtomo, M. Kawasaki, Y. Sakurai, I. Ohkubo, R. Shiroki, Y. Yoshida, T. Yasuda, Y. Segawa, and H. Koinuma, *Mat. Sci. Eng.* **B56**, 263 (1998).

30. "Room temperature ultraviolet laser emission from ZnO nanocrystalline thin films grown by laser MBE", A. Ohtomo, M. Kawasaki, Y. Sakurai, Y. Yoshida, H. Koinuma, P. Yu, Z.K. Tang, G.K.L. Wong, and Y. Segawa, *Mat. Sci. Eng.* **B54**, 24 (1998).

31. "Coaxial impact-collision ion scattering spectroscopy analysis of ZnO thin films and single crystals", T. Ohnishi, A. Ohtomo, I. Ohkubo, M. Kawasaki, M. Yoshimoto, and H. Koinuma, *Mat. Sci. Eng.* **B56**, 256 (1998).

32. "Determination of surface polarity of c-axis oriented ZnO films by coaxial impact collision ion scattering spectroscopy", T. Ohnishi, A. Ohtomo, M. Kawasaki, K. Takahashi, M. Yoshimoto, and H. Koinuma, *Appl. Phys. Lett.* **72**, 824 (1998).

33. "Excitonic ultraviolet laser emission at room temperature from naturally made cavity in ZnO nanocrystal thin films", M. Kawasaki, A. Ohtomo, I. Ohkubo, H. Koinuma, Z.K. Tang, P. Yu, G.K.L. Wong, B.P. Zhang, and Y. Segawa, *Mat. Sci. Eng.* **B56**, 239 (1998).

34. "Combinatorial laser molecular beam epitaxy (MBE) growth of Mg-Zn-O alloy for band-gap engineering", Y. Matsumoto, M. Murakami, Z.W. Jin, A. Ohtomo, M. Lippmaa, M. Kawasaki, and H. Koinuma, *Jpn. J. Appl. Phys.* **38**, L603 (1999).

35. "Room temperature ultraviolet laser emission from self-assembled ZnO microcrystalline thin films", Z.K. Tang, G.K.L. Wong, P. Yu, M. Kawasaki, A. Ohtomo, H. Koinuma, and Y. Segawa, *Appl. Phys. Lett.* **72**, 3270 (1998).

36. "Room-temperature gain and lasing in microcrystalline ZnO thin films", P. Yu, Z.K. Tang, G.K.L. Wong, M. Kawasaki, A. Ohtomo, H. Koinuma, and Y. Segawa, *J. Cryst. Growth* **184/185**, 601 (1998).

37. "Double heterostructure based on ZnO and $Mg_xZn_{1-x}O$", A. Ohtomo, M. Kawasaki, T. Koida, H. Koinuma, Y. Sakurai, Y. Yoshida, M. Sumiya, S. Fuke, T. Yasuda, and Y. Segawa, *Mats. Sci. Forum* (*Proceedings of International Conference on SiC, III-Nitride and Related Mats.*) **264-268**, 1463 (1998).

38. "Excitonic ultraviolet laser emission at room temperature from naturally made cavity in ZnO nanocrystalline thin films", A. Ohtomo, I. Ohkubo, H. Koinuma, Z. K. Tang, P. Yu, G.K.L Wong, B.P. Zhang, Y. Segawa, and M. Kawasaki, *Proceedings of the 2_{nd} Symposium on Atomic-scale Surface and Interface Dynamics*, 225-231, (1998).

39. "ZnO quantum structures towards UV diode lasers", M. Kawasaki, A. Ohtomo, R. Shiroki, I. Ohkubo, H. Kimura, G. Isoya, T. Yasuda, Y. Segawa, and H. Koinuma, *Extended Abstracts 1988 International Conference Solid State Mat. Devices*, 356-357 (1988).

40. "Ultraviolet excitonic laser action at room temperature in ZnO nanocrystalline epitaxial films", M. Kawasaki, A. Ohtomo, H. Koinuma, Y. Sakurai, Y. Yoshida, Z.K. Tang, P. Yu, G.K.L. Wong, and Y. Segawa, *Mats. Sci. Forum* (*Proceedings of International Conference on SiC, III-Nitride and Related Mats.*) **264-268**, 1459 (1998).

41. "GaN growth on ozonized sapphire(0001) substrates by MOVPE", T. Honda, A. Inoue, M. Mori, T. Shirasawa, N. Mochida, K. Saotome, T. Sakaguchi, A. Ohtomo, M. Kawasaki, H. Koinuma, F. Koyama, K. Iga, *J. Cryst. Growth* **195**, 319 (1998).

42. "Lasing of exciton at room temperature in ZnO quantum dots thin films", Y. Segawa, A. Ohtomo, M. Kawasaki, H. Koinuma, Z.K. Tang, P. Yu, and G.K.L. Wong, *RIKEN Review* **17**, 19 (1998).

43. "Observation of $SrTiO_3$ step edge dynamics by real-time high-temperature STM", M. Lippmaa, M. Kawasaki, A. Ohtomo, T. Sato, M. Iwatsuki, and H. Koinuma, *Appl. Surf. Sci.* **130-132**, 582 (1998).

44. "Atom technology for Josephson tunnel junctions: $SrTiO_3$ substrate surface", M. Lippmaa, K. Takahashi, A. Ohtomo, S. Ohashi, T. Ohnishi, N. Nakagawa, T. Sato, M. Iwatsuki, H. Koinuma, and M. Kawasaki, *Mat. Sci. Eng.* **B56**, 111 (1998).

45. "A study of $SrTiO_3$ surface dynamics during wet etching and high-temperature annealing", M. Lippmaa, K. Takahashi, T. Ohnishi, N. Nakagawa, A. Ohtomo, T. Sato, M. Iwasaki, H. Koinuma, and M. Kawasaki, *Proceedings of the 2_{nd} International Symposium on Blue Laser and Light Emitting Diodes* 205 (1998).

46. "Laser MBE of ceramic thin films for future electronics", H. Koinuma, N. Kanda, J. Nishino, A. Ohtomo, H. Kubota, M. Kawasaki, M. Yoshimoto, *Appl. Surf. Sci.* **109/110**, 514, (1998).

47. "Dimension controlled epitaxy of quantum functional oxide thin films by pulsed-laser processes", H. Koinuma, X.G. Qiu, R. Tsuchiya, N. Kanda, J. Nishino, A. Ohtomo, M. Kawasaki, and H. Koinuma, *Appl. Surf. Sci.* **127-129**, 403 (1998).

48. "Growth of ZnO thin films by laser MBE: Lasing of exciton at room temperature", Y. Segawa, A. Ohtomo, M. Kawasaki, H. Koinuma, Z.K. Tang, P. Yu, and G.K.L. Wong, *Phys. Stat. Sol.* (b) **202**, 669 (1997).

49. "Ultraviolet spontaneous and stimulated emission from ZnO microcrystallite thin films at room temperature", Z.K. Tang, P. Yu, G.K.L. Wong, M. Kawasaki, A. Ohtomo, H. Koinuma, and Y. Segawa, *Solid State Comm.* **103**, 459 (1997).

50. "Room temperature ultraviolet laser emission from microstructured ZnO thin films", Z.K. Tang, P. Yu, G.K.L. Wong, M. Kawasaki, A. Ohtomo, H. Koinuma, and Y. Segawa, *Nonlinear Optics* **18**, 355 (1997).

51. "Transmission electron microscopy study of room temperature lasing epitaxial ZnO films on sapphire", N. Wong, K.K. Fung, P. Yu, Z.K. Tang, G.K.L. Wong, M. Kawasaki, A. Ohtomo, and M. Koinuma, *Mat. Res. Soc. Symp. Proc.* **482**, 423 (1997).

52. "Oxide quantum structures for future electro-photonics", M. Kawasaki, A. Ohtomo, R. Tsuchiya, J. Nishino, and H. Koinuma, *Mat. Sci. Soc. Symp. Proc.* **474**, 303 (1997).

53. "Construction and superfunction of metal-oxide nanostructures and interfaces", M. Kawasaki, R. Tsuchiya, N. Kanda, A. Ohtomo, and H. Koinuma, *Sci. Rep. RITU* **A44**, 207 (1997).

54. "Atomic control of $SrTiO_3$ surface for perfect epitaxy of perovskite oxides", M. Kawasaki, A. Ohtomo, T. Arakane, K. Takahashi, M. Yoshimoto, and H. Koinuma, *Appl. Surf. Sci.* **107**, 102 (1996).

Invited Talks

1. "Material issues of ultraviolet laser diode based on ZnO", A. Ohtomo and M. Kawasaki, *International ZnO Workshop*, Dayton Ohio, USA , Octorber 7-8, 1999.

2. "Semiconductor Technologies of ZnO Films towards Ultraviolet LEDs and Invisible FETs", A. Ohtomo and M. Kawasaki, *International Display Workshop (IDW)'99*, Sendai, Japan, December 1-4, 1999.

3. "Nanocrystalline films and superlattices based on Zn towards UV light emitting device application", A. Ohtomo and M. Kawasaki, *Bell Laboratories Physics Seminar*, Marray Hill, USA, October 11, 1999.

Contributed Talks

1. "High-throughput optimizations of alloy and doped films based on ZnO and parallel synthesis of $ZnO/Mg_xZn_{1-x}O$ quantum wells using combinatorial laser MBE towards ultraviolet laser"
   A. Ohtomo, T. Makino, K. Tamura, Y. Matsumoto, Y. Segawa, Z.K. Tang, G.K.L. Wong, H. Koinuma, and, M. Kawasaki,
   SPIE's Optoelectronics 2000, International Symposium on Integrated Optoelectronic Devices, San Jose, USA, January 22-28, 2000.

2. "Epitaxial growth of alloys and superlattices based on ZnO"
   A. Ohtomo, I. Ohkubo, M. Kawasaki, H. Koinuma, G. Isoya, T. Yasuda, and Y. Segawa
   The 2_{nd} International Symposium on Blue Laser and Light Emitting Diodes, Chiba, Japan, October 2, 1998.

3. "Room temperature ultraviolet laser emission from laser MBE grown ZnO nanocrystals"
   A. Ohtomo, Y. Sakurai, Y. Yoshida, M. Kawasaki, H. Koinuma, P. Yu, Z.K. Tang, G.K.L. Wong, and Y. Segawa
   Symposia *The 1_{st} Yamazaki International Symposium and 3_{rd} TIT International Symposium on Oxide, Electronics*, Tokyo, Japan, December 18, 1996.

Poster Presentations

1. "Epitaxial growth of single crystalline ZnO films towards novel transparent optelectronics"
   A. Ohtomo, K. Tamura, K. Saikusa, R. Shiroki, H. Kimura, and M. Kawasaki
   The 3_{rd} Symposium Atomic-Scale Surface and Interface Dynamics, Fukuoka, March 4, 1999.

2. "Excitonic ultraviolet laser emission at room temperature from naturally made cavity in ZnO nanocrystalline thin films"
   A. Ohtomo, I. Ohkubo, H. Koinuma, Z.K. Tang, P. Yu, G.K.L. Wong, B.P. Zhang, Y. Segawa, and
   The 2_{nd} Symposium Atomic-Scale Surface and Interface Dynamics, Tokyo, March 5, 1998.

3. "Alloys and heterostructures based on ZnO"
   A. Ohtomo and M. Kawasaki
   Thin Film Workshop, Santa Barbara, California, December 11, 1997.

4. "ZnO nanocrystalline thin films as an ultraviolet laser emitting material"
   A. Ohtomo, M. Kawasaki, H. Koinuma, P. Yu, Z.K. Tang, G.K.L. Wong, and Y. Segawa
   Materials Research Society, 1997 Fall Meeting, Boston, USA, December 9, 1997.

5 "Fabrication of alloys and superlattices based on ZnO towards ultraviolet laser"
   A. Ohtomo, K. Kawasaki, Y. Sakurai, I. Ohkubo, R. Shiroki, Y. Yoshida, T. Yasuda, Y. Segawa, and H. Koinuma
   The 4_{th} International Workshop on Oxide Electronics, Maryland, USA, December 4, 1997.

6. "Ultraviolet excitonic laser action at room temperature in ZnO nanocrystalline epitaxial films"
   A. Ohtomo, M. Kawasaki, H. Koinuma, Y. Sakurai, Y. Yoshida, Z.K. Tang, P. Yu, G.K.L. Wong, and Y. Segawa
   International Conference on SiC, III-Nitride and Related Mats., Stockholm, SWEDEN, September 3, 1997.

7 "A novel widegap semiconductor: $Mg_xZn_{1-x}O$"
   A. Ohtomo, M. Kawasaki, T. Koida, H. Koinuma, Y. Sakurai, Y. Yoshida, M. Sumiya, S. Fuke, T. Yasuda, and Y. Segawa
   International Conference on SiC, III-Nitride and Related Mats., Stockholm, SWEDEN, September 1, 1997.

国内学会

(招待講演)

1. 「レーザアブレーション法による酸化亜鉛薄膜の作製と光物性」
   大友 明、鯉沼秀臣、川崎雅司
   第3回高機能レーザアブレーション加工の産業応用調査専門委員会、東京、1999/12/7.

2. "Material issues towards ultraviolet laser diodes based on ZnO"
   大友 明、川崎雅司
   Widegap Compound Semiconductor School、千葉、1999/4/1.

3. 「酸化亜鉛量子構造の作製と紫外発光素子への応用」
   大友 明、鯉沼秀臣、川崎雅司
   光未来技術研究会「最近の光材料と応用」セミナー、東京、1999/3/23.

4. 「レーザーアブレーション法による ZnO ナノ結晶薄膜の作製」
   大友 明、川崎雅司
   第 59 回応用物理学会学術講演会、広島、1998/9/17.

(寄稿講演)

「ZnO 単結晶薄膜の高分解能 XRD 解析」大友他、第 46 回応用物理学関係連合講演会、東京、1999/3/29 ほか「応用物理学会」「日本セラミックス協会年会」「日本 MRS 学術シンポジウム」において 1996～2000 年現在までに計 22 件の講演を行った.

著書･執筆等

1. 「酸化物で紫外線レーザーを創る」
   大友 明、川崎雅司、*パリティ* **13**, 49 (1998).

2. 「ZnO ナノ結晶からの室温励起子レーザー発振」
   川崎雅司、大友 明、固体物理、**33**, 59 (1998).

3. 「表面界面-ハイヤーオーダーエピタキシ-」
   大友 明、川崎雅司
   酸化物エレクトロニクス調査報告書 II-第 5 節 1 項-(日本電子工業振興協会編) p135 (1997).

4. 「新機能-光物性-」
   大友 明、川崎雅司
   酸化物エレクトロニクス調査報告書 II-第 6 節 2 項-(日本電子工業振興協会編) p161 (1997).

5. 「表面･界面-表面の電子構造-」
   川崎雅司、大友 明、大橋 智
   酸化物エレクトロニクス調査報告書 I-第 7 節 6 項-(日本電子工業振興協会編) p241 (1996).

6. 「酸化亜鉛紫外レーザー」
   田村謙太郎、大友 明、川崎雅司
   マテリアルインテグレーション **12**, 9 (1999).

特許

1. 川崎雅司、鯉沼秀臣、大友明、瀬川勇三郎
「光半導体素子及びその製造方」、 特開平 10-256673、1998 年 10 月公開.

2. 川崎雅司、鯉沼秀臣、大友明、瀬川勇三郎、安田隆
「Mg-Zn-O 固溶体薄膜」、特開平 10-270749、1998 年 10 月公開.

3. 川崎雅司、大野英男、大友 明:「半導体デバイス」: 整理番号 P0099JP、1999 年 3 月出願.

受賞等

1. 第 2 回応用物理学会講演奨励賞:「*Ex-situ* 紫外線オゾン処理による酸化物表面の清浄化」
第 44 回応用物理学関係連合講演会、東京、1997/05/30.

2. 日本 MES 学術シンポジウム奨励賞:「高温超伝導トンネル接合の作製」
日本 MRS 学術シンポジウム、東京、1994/12/8.

Acknowledgements

The present thesis is a compilation of my studies during 1995-2000 with support by JSPS Research Fellowships for Young Scientists (1997-2000). There are many people who have contributed to this study. First of all, I would like to express my deepest gratitude from bottom of my heart to Prof. Masashi Kawasaki for his variable advice and continuous encouragement throughout the work. He gave me a chance to work at laser MBE. He possesses a broad view of the society and the world situation as well as exceptional scientific talent. I learned from him a lot of things. Also, I would like to express my deepest gratitude to my supervisor Prof. Hideomi Koinuma for his helpful advises, discussions, and encouragement. He provided a lot of collaborative works with my research to broaden my scientific insights. I am much grateful to Dr. Yusaburo Segawa at RIKEN gave me a chance to study with optical stuff.

I am most indebted to my co-workers, Prof. Z.K. Tang at Hong Kong University of Science (HKUST) and Technology, Dr. T. Yasuda, Dr. T. Makino, Mr. G. Isoya at RIKEN, and Dr. M. Sumiya and Prof. S. Fuke at Shizuoka Univ., and Mr. M. Sasaki, Mr. Y. Sakurai, Mr. T. Koida, Mr. I. Ohkubo, Mr. H. Kimura, Miss. R. Shiroki, Mr. K. Tamura, Mr. K. Saikusa, Miss. Y. Osaka, Mr. A. Tsukazaki in Tokyo Institute of Technology for their continuous collaboration in the course of this work. I am indebted to Dr. Y. Matsumoto, Dr. T. Fukumura, Ms. Nakajima, Mr. M. Murakami, Mr. T. Aita and Mr. K. Hasegawa for their active collaboration.

I appropriated Dr. K. Takahashi and Mr. M. Nakamura in Shinkosha Corp. for their active collaboration and for kindly providing special oxide substrates. I also would like to express my gratitude to Dr. P. Yu of HKUST, Dr. T. Chikyo of NRIM, K. Saito of Philips Co., Ltd., and Dr. T. Yaguchi and Dr. T. Kamino of Hitachi Instruments Eng., Co., Ltd. for TEM observations, and Dr. H. Imai and Dr. J. Kikuma of Asahi Chemical Industry Co. for AES measurements, and Prof. H. Ohno of Tohoku Univ. for fruitful discussions and help for experiments.

I am much indebted to Dr. Naoki Kanda, Dr. R. Tsuchiya, Mr. K. Shimozono, for their collaboration in the experiments. I am also indebted to Dr. M. Lippmaa, Dr. R.S.M. Rao, Dr. Z.W. Jin, Mr. N. Matsuki, Miss. K. Miyazaki, Mr. K.S. Yun, Mr. Y.Z. Yoo, Mr. N. Nakagawa, Mr. M. Ohtani, and Mr. R. Takahashi, and many other members of Koinuma, Kawasaki, and Yoshimoto Laboratories offered me many helpful suggestions and kind assistance, for which I am deeply grateful.

I would like to appreciate secretaries, Ms. M. Nomura, Ms. K. Mukai, Ms. M. Tanabe, Ms. Y. Egawa, Ms. S. Kubara, Ms. J. Tsunakawa, Ms. M. Honda, Ms. Y. Inomata for their kindness.

Finally, I would like to express my sincere gratitude to my family and my wife, Tomoko, for their endless support, sympathy and tolerance in all means.

February, 2000

Akira Ohtomo